SAPIENZA
UNIVERSITÀ DI ROMA

Measurement and estimation of seismic attenuation for near-surface site characterization

DEPARTMENT OF CIVIL, CONSTRUCTIONAL AND ENVIRONMENTAL ENGINEERING (DICEA)

Ph.D. course in Environmental and Hydraulic Engineering

PhD Candidate:
Ing. Francesco Saverio Desideri

Tutor:
Prof. Michele Cercato

Coordinator
Prof. Francesco Gallerano

2018-2019

.

Summary

List of figures

List of tables

Chapter 1.
Introduction

1.1 Problem outline and motivation

Seismic attenuation is a fundamental parameter on the comprehension of the viscoelastic real behavior of the medium. Characterization of the ability of materials to transmit and dissipate seismic waves is even important for petrophysical descriptions of reservoir rocks.

From a physical point of view, seismic attenuation is due to three different phenomena:

- intrinsic attenuation, that exists as a results of the energy loss due to internal friction and associated to the dissipative behaviour of the medium;
- attenuation for scattering, that is the attenuation of the propagating waves in the inhomogeneous earth caused by diffraction, reflection and dissipation;
- geometrical spreading, that is the energy density decrease over the wavefront of increasing size.
-

Compared with seismic velocities and densities, absorption and scattering are often more sensitive to clay content, pore fluids, gas, or fracturing (*Klimentos, 1995*).

The most common measuring parameter of seismic wave attenuation is the dimensionless quality factor Q and its inverse (damping or dissipation factor) Q^{-1}. The quality factor as a function of depth is of fundamental interest in groundwater, engineering, and environmental studies, as well as in hydrocarbon exploration and earthquake seismology (*Morozov, 2015*). The desire to understand the attenuation properties of the earth is based on the observation that the seismic wave amplitude reduces as the wave propagates. The classical approach to attenuation estimation is henceto measure the absolute spatial decay rate of wave amplitude in the time domain. The interpretation of the results is usually difficult and it lacks a standard procedure for attenuation measurements because many not well-understood problems such as source mechanism, wave scattering, and geometrical spreading of the wavefront, are involved in the phenomenon (*Teng, 1968*),. These problems have kept Q away from testing in professional practice, despite being a fundamental parameter to take into account for seismic characterization.

The reduction of the amplitude due to attenuation is generally frequency-dependent and, more importantly, attenuation can provide information about lithology, physical state, and degree of rock saturation (*Toksoz and Johnston, 1981),* so it can be used, besides or along the seismic velocity, to characterize the material of a geological structure using seismogram analysis.

Conventionally, energy dissipation properties are described by Q-factor of the materials. However, Q can assume different meaning in different contexts. We need indeed to distinguish three different uses of Q-factor: (1) the Q^{-1}as a measure of "internal friction" used in petrophysical interpretation, (2) many measured ("apparent") Q_S arising from observations, and (3) the "axiomatic," mathematical Q used in viscoelastic theory and numerical modeling (*Morozov, 2018*).

The measured or effective Q is a combination of intrinsic attenuation, scattering and geometrical spreading, and it is generally referred to as apparent attenuation (*Barton, 2007*).

In practical seismic data processing and inversion, the exact value of the Q values are sometimes unimportant. The attenuation modeling is generally used to correct the data for attenuation effects; to this end, an absolute Q is not strictly necessary. By contrast, in seismic modelling, it is important to ensure that the algorithms adequately represent the physical mechanisms of wave attenuation, adopting an accurate Q profile for the soil model, related to petrophysical properties and internal friction.

To fully understand seismic wave propagation in the earth, the quality factors are parameters that must be known. For example, high frequency Rayleigh waves possesses information of the shear (S)-wave velocity (VS) and the quality factors of near-surface materials.

Seismic modeling for seismic prospecting generally employs elastic wave simulations and most local site response studies take a standard damping factor of 0.05% for the entire soil column. An accurate knowledge of the quality factor (i.e. damping) profile can improve the quality of the results, like in local seismic response studies.

Attenuation can be estimated both from surface or borehole data. Most of the borehole studies conducted for attenuation measures are calibrated for large depths, with large receiver spacing and array length. Some others are calibrated on earthquake measures. The idea of producing attenuation measures from downhole investigations started with the downhole measurements conducted for the 2016 Microzonation campaign. Downhole tests represent the most used borehole surveys to provide an accurate velocity profile and if the measurements are carried out with appropriate equipment and the required precautions, attenuation can be reliably estimated even in the near-surface range.

In spite of the broad variety of methods available for Q estimation, only a few techniques, such as the rise-time method or the spectral ratio method, are widely accepted for borehole studies.

1.2 **Objectives**

The knowledge of Q is very desirable for improving seismic resolution (*Wang, 2008*), facilitating AVO amplitude analysis, better understanding the lithology of subsurface and providing useful information about the porosity and fluid or gas saturation of reservoir. Anelastic attenuation can be regarded as a disturbance of seismic waves that must be eliminated by inverse Q-filters. Utilizing quality factors only as a disturbance to remove may be an underestimation error. Knowledge of large dissipation in the near surface layers is important for shallow seismic surveys and local observations of earthquakes because near-surface unconsolidated sedimentary layers or weathering materials may influence seismic records (*Jongmans, 1990*). The anelastic properties of earth materials have attracted the interest of many scientists in recent years, although great efforts have been made to determine it.

The purpose of this work is to investigate the reliability of the rise-time and the spectral ratio methods for Q estimation in a seismic downhole campaign, to obtain accurate Q profiles. The obtained parameters have been also compared through a study of surface waves dispersion and attenuation curves, adopting in-situ attenuation profiles for the forward modelling.

1.3 **Technical approach**

In this study, we applied two different methods to estimate attenuation. We used a standard spectral ratio technique to obtain the frequency independent$Q$ and then compared the results to Qobtained in the time domain from rise-time measurements. These methods are unaffected by far-field geometric spreading. A review of the methods using borehole and surface waves studies is given in **Chapter 3**.

Additionally, we estimate dispersion and attenuation curves using parameters model using results coming from borehole study. A comparison between experimental and theoretical curves can give us an idea about the reliability of the approach.

P, SH-wave velocity and Q measurements were conducted in this study using an 8-receivers (10 Hz) 3 Channels seismic string in two sites, one located in Rieti and the other in the headquarter of INGV in Rome. In the Rieti site, it has been operated a MASW surveys with 24 vertical geophones (4.5 Hz) in order to obtain surface wave dataset.

1.4 **Original aspects**

Most of the borehole attenuation studies presented in literature are carried out for hydrocarbon exploration. The main contribution of the present work is to apply the two most used attenuation estimation methods to near-surface data. They include two

techniques to determine the material damping ratio of the soil based on the downhole (DHT) test, and other two for attenuation and dispersion curves from MASW testing.

For the downhole test have been adopted the spectral ratio and the rise-time methods, the last one has never been used in near-surface studies. Our purpose is to provide reliable measures of attenuation even from this method, comparing with the spectral ratio one. The processing used for the test can be adopted as a standard procedure for future studies in this sector, since there is not a standard procedure for this purposes yet.

Another original aspect of this work is the implementation of a new modelling algorithm, based on the direct stiffness matrix method, improved by the insertion of a detailed attenuation profile.

1.5 **Organization of the thesis**

Chapter 1: introduces the problem outline and motivation, including the importance of the seismic attenuation. A synthetic list of existing methods is given and further needs and objectives are explained. The approach and original contributions from the thesis are described.

Chapter 2: outlines the seismic waves propagation relations on viscoelastic media. The theoretical background of body and surface waves is presented. Attenuation theory is introduced for both body and surface waves.

Chapter 3: the chapter focus on the body and surface waves methods used for seismic attenuation measurements in terms of experimental and theoretical measurements. The first two section are accompanied by reviews of the most used methods for both body and surface waves datasets. The second explain the improved direct stiffness matrix method that has used to obtain theoretical dispersion and attenuation curves in order to compare the two set of data.

Chapter 4: study in deep the DHT test to determine the material damping ratio of near-surface layered soil. The spectral ratio method as well as the rise-time method are elaborated based on the Rieti and INGV dataset examples. The methods are compared each another to check the material damping values obtained. Deals with the phase shift method and the spatial decay to determine the experimental dispersion and attenuation curves of shallow soil layers for the Rieti surface waves dataset.

Chapter 5: summarizes the conclusions from the present research and gives recommendations for future work.

Chapter 2.
Plane waves propagation in vertically inhomogeneous media

This chapter describes the theory of seismic wave propagation in linear elastic and in linear viscoelastic solids, several types of waves propagate within the earth and along its surface due to a mechanical disturbance. The waves that are generated can be divided into two main categories; body waves and surface waves (*Aki & Richards, 1980*). We will first give the basic notions on the theory of wave propagation and then focus on the characteristics and parameters that describe body and surface waves propagation.

2.1 Seismic waves

Many studies have been carried out in order to understand the characteristics of seismic attenuation through the **quality factor** Q. These studies are based on the use of P waves (Q_α), S waves (Q_β).

To describe seismic attenuation, it is therefore necessary to go through a brief explanation on the propagation and composition of the seismic wave field.

When an earthquake occurs, the energy released is partly dissipated in the form of heat, developed due to the friction deriving from the sliding of the rock masses along the fault surface. The remaining energy is partially spent as work, resulting in the displacement of the masses involved, and partly propagates in the ground in the form of seismic waves. These consist of elastic waves that propagate in the ground and on the free surface with velocity, frequency and amplitude dependent on the elastic properties of the medium and the source. The energy carried by the seismic waves translates into stresses and deformations of the ground and therefore in displacements (seismic shaking). In relation to the type of stress and deformation to which the soil is subjected as well as to the way in which the waves are propagated, body waves (P and S waves) and surface waves (Love and Rayleigh waves) are distinguished.

2.1.1 Wave equations for an elastic medium

In an infinite, homogeneous, isotropic, elastic medium, the equation of motion in the absence of body forces is given by Navier's equation, which may be expressed in terms of

the displacements and the cubic dilation and rotation vector. These two equations may be easily transformed into wave equations.

In the first place, we apply the divergence operation to the Navier's equation (*Aki and Richards, 1980*):

$$\alpha^2 \nabla\theta - \beta^2 \nabla \times \omega = \ddot{u} \qquad (2\text{-}1)$$

where α and β are parameters related to cubic dilation θ and the rotation vector ω, and, in consequence, related to changes in volume and in shape without changes in volume, respectively. $\ddot{u}$ represents the second partial derivative of the displacement u.

The divergence of the gradient of θ is its Laplacian, that of the curl of ω is null and the divergence of the displacement u is the cubic dilation θ, given by the summation of longitudinal stresses ($\theta = \varepsilon_{11} + \varepsilon_{22} + \varepsilon_{33}$). Thus, we obtain:

$$\nabla^2\theta = \frac{1}{\alpha^2}\frac{\partial^2\theta}{\partial t^2} \qquad (2\text{-}2)$$

To the same equation (2-1), we apply the curl operator. The curl of the gradient of the scalar function θ is null and that of the displacement $u(x,t)$ is the rotation vector ω. The curl of the curl of ω is equal to the gradient of the divergence, which is null minus the Laplacian. The results is:

$$\nabla^2\omega = \frac{1}{\beta^2}\frac{\partial^2\omega}{\partial t^2} \qquad (2\text{-}3)$$

Equation (2-2) and (2-3) have the form of wave equations for the scalar function θ and vector function ω. The solution of both equations represent waves that propagate in the elastic medium and the parameters α and β are their velocities. These velocities are functions of the elastic coefficients λ and μ and the density ρ.

Because θ represent changes in volume without changes in shape, solutions of equation (2-2) correspond to compressionala and dilational motion, or longitudinal waves, also called **P-waves**. Solutions of equation (2-3) represent shear waves that propagate with velocity β. The medium changes in shape, but not in volume, since the divergence of ω is null. These waves are called **S-waves**.

2.1.2 **Potential functions**

Displacement $u(x,t)$ in an elastic medium form a vector field. We can, therefore, apply Helmholtz's theorem that allows their rappresentation in terms of two potential functions, a scalar potential ϕ and a vector potential ψ:

$$u = \nabla\phi + \nabla \times \psi \qquad (2\text{-}4)$$

The vector potential ψ must satisfy the condition that its divergence is zero ($\nabla \cdot \psi = 0$).

By defining the rotation tensor as $\omega = \nabla \times u$ and the cubic dilation as $\theta = \nabla \cdot u$ it is easy to reduce the relations of the two potentials to the cubic dilation θ and the rotation ω:

$$\theta = \nabla^2 \phi \qquad (2\text{-}5)$$

$$\omega = -\nabla^2 \psi \qquad (2\text{-}6)$$

These relations indicates that ϕ is related to changes in volume and ψ to changes in form. We can even rewrite the differential equation of motion in term of the wave potentials, by a scalar and a vector equation in a much more simply form:

$$\alpha^2 \nabla^2 \phi + \frac{\phi}{\rho} = \ddot{\phi} \qquad (2\text{-}7)$$

$$\beta^2 \nabla^2 \psi + \frac{\psi}{\rho} = \ddot{\psi} \qquad (2\text{-}8)$$

2.1.3 **Types of body waves**

Body waves are transmitted through the interior of the earth, the medium of the wave, and consist of compressional waves (P-waves) and shear waves (S-waves). Body waves propagate inside the earth with spherical or hemispherical wave fronts (depending on the position of the source) increasing wider radius. The two main types are:

- **P-waves**: The particle motion of compressional waves is parallel to the motion of the wave itself, causing dilatation and compression of elementary volume particles (*Aki & Richards, 1980*). P-waves are the first to reach the surface and recorded by seismographs, propagating in depth at a speed between 1.5 and 8 km/s, depending on the material density; they can propagate either through the solid rock, or through a liquid material (magma or water). They are compression waves, which originate from the hypocenter and propagate within the volume of the rocks by successive compression and dilation of the rocks themselves, causing volume changes. They are also called longitudinal waves (or compression waves) because the oscillations of the infinite planes in which one can imagine dividing the rocky body occur in the same direction of wave propagation (as in figure 2.1);

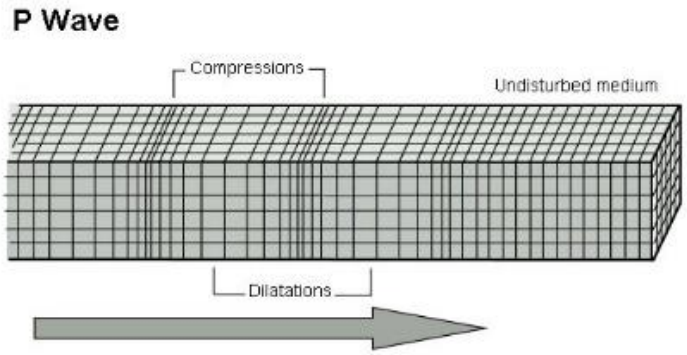

Figure 2-1: Particle motion associated with compressional waves

- **S-waves**: The particle motion associated with shear waves is perpendicular to the direction of wave propagation and has therefore both a vertical (**SV**) and a horizontal (**SH**) component. The transverse particle motion causes shear deformations (distortional) of volume elements within the medium (*Aki & Richards, 1980; Kramer, 1996*). They are also called secondary because they are slower than the P waves that represent the first arrivals. The wave can be polarized in two different directions, in the vertical direction SV and in the horizontal direction SH. These two components are identical in the case of an isotropic medium while they are separate and travel at different speeds considering a non-isotropic medium (as in **Figure 2.2**).

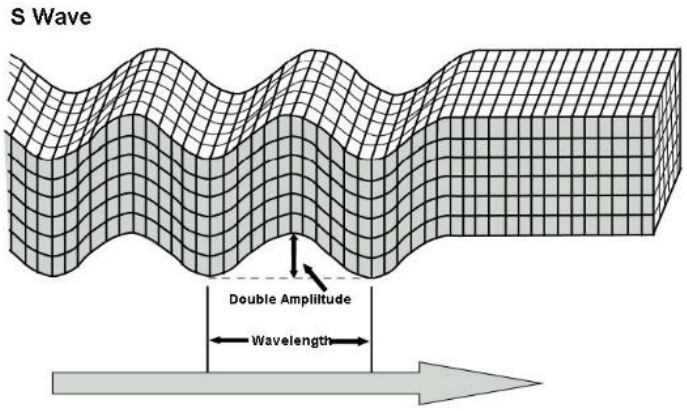

Figure 2-2: Particle motion associated with shear waves

As regards to body waves, although both are usually generated, depending on the source mechanism, those of one type tend to prevail over the other. For example, in the case in which the source is represented by a deep explosion, compressive stresses will prevail and the waves generated are mainly P-waves, when, instead, the source is due to a deep flow, as happens for the earthquakes, then the stresses induced in the ground are mainly cut off and the S-waves prevail.

The same result of equations (2-2) and (2-3) can be obtained for the potentials ϕ and ψ defined in (2-4). If in equations (2-7) and (2-8) we disregard the contribution of body forces ϕ and ψ, we obtain:

$$\nabla^2\phi = \frac{1}{\alpha^2}\frac{\partial^2\phi}{\partial t^2} \quad (2\text{-}9)$$

$$\nabla^2\psi = \frac{1}{\beta^2}\frac{\partial^2\psi}{\partial t^2} \quad (2\text{-}10)$$

In the absence of body forces, the potentials ϕ and ψ are also solutions of the wave equation. Since α and β are the velocities of P and S waves, ϕ is the potential of P waves and ψ that of S waves. The total elastic displacement u is the sum of the displacements of P and S waves and can be written as:

$$u = u^P + u^S \quad (2\text{-}11)$$

By defining velocities α and β of P and S waves as:

$$\alpha = \sqrt{\frac{(\lambda + 2\mu)}{\rho}} = \sqrt{\frac{M_V}{\rho}} \quad (2\text{-}12)$$

where M_V is the one-dimensional compression stiffness module, and ρ is the mass density.

$$\beta = \sqrt{\frac{\mu}{\rho}} \quad (2\text{-}13)$$

with μ stiffness shear modulus of the medium.

The wave equation for P-waves can be rewritten as:

$$\rho\frac{d^2\phi}{dt^2} = (\lambda + 2\mu)\nabla^2\phi \quad (2\text{-}14)$$

where ρ is the density, ϕ is the potential of P waves, while λ and μ are the Lamè constants. μ is the stiffness modulus, while λ is defined as $\lambda = K - 2/3\,\mu$, where K is the compressibility module.

The study of the dynamic equilibrium of the ideal elastic medium shows that the volume of seismic waves associated with states of compression or volumetric expansion, i.e. the P-waves, propagates in a direction parallel to the displacement of the volume element hit by the wave and with α velocity

Compressional waves are connected to distortional deformation phenomena, i.e. S-waves, are instead characterized by a perpendicular direction to the displacement of the volume element hit by the wave. S-waves are characterized by a wave equation equal to:

$$\rho\frac{d^2\psi}{dt^2} = (\mu)\nabla^2\psi \quad (2\text{-}15)$$

where the term $\nabla \times u$ represents the quantity being propagated.

Introducing $u^P = \nabla\phi$ and $u^S = \nabla \times \psi$ we can write wave equations in terms of displacement u:

$$\frac{\partial^2 u_2}{\partial x_1^2} = \frac{1}{\alpha^2}\frac{\partial^2 u_2}{\partial t^2} \qquad (2\text{-}16)$$

$$\frac{\partial^2 u_1}{\partial x_1^2} = \frac{1}{\beta^2}\frac{\partial^2 u_1}{\partial t^2} \qquad (2\text{-}17)$$

with u_1 and u_2 solutions of wave equations.

The ratio of α and β can be expressed solely as a function of the Poisson ratio ν:

$$\left(\frac{\alpha}{\beta}\right)^2 = \frac{\lambda + 2\mu}{\mu} = \frac{2(1-\nu)}{(1-2\nu)} > 1 \qquad (2\text{-}18)$$

which shows that it is always $V_S < V_P$.

For $\nu = 1/4$ (a typical value for several materials), $V_P = \sqrt{3} \cdot V_S$

Type of soil	V_P (m/s)	V_S (m/s)
Saturated clay	1500	100 – 150
Fine and medium sand	300 – 500	120 – 200
Dense sand	400 – 600	200 – 400
Gravel	500 – 750	300 – 600
Sandstone	1500 – 4500	700 – 1500
Marl	1500 – 4500	600 – 1500

Table 2-1: Typical values of V_P and V_S

A typical solution of the wave equations (2-9) and (2-10) are a harmonic function as:

$$f(x,t) = Ae^{i(kx-\omega t)} + Be^{i(kx-\omega t)} \qquad (2\text{-}19)$$

Where ω represents the angular frequency and k the wave number. The velocity of wave propagation is $c = \omega/k$. Another form of the solution can be represented by using sine and cosine functions:

$$f(x,t) = Acos(kx - \omega t) + Bsin(kx - \omega t) \qquad (2\text{-}20)$$

2.1.3.1 **Fourier Transform**

Waves with an arbitrary dependence in time can be represented by the sum or integral of harmonic waves of different frequencies using Fourier's trasform:

$$f(x_i,t) = \frac{1}{2\pi}\int_{-\infty}^{\infty} F(\omega) exp\left[i\left(\frac{\omega}{c(\omega)}S(x_i) - \omega t\right)\right] d\omega \quad (2\text{-}21)$$

where $F(\omega)$ is a complex function that is called the complex spectrum of $f(x_i,t)$ and can be representes as:

$$F(\omega) = R(\omega) + iI(\omega) = A(\omega)e^{i\Phi(\omega)} \quad (2\text{-}22)$$

where $A(\omega)$ is the amplitude spectrum and $\Phi(\omega)$ the phase spectrum.

2.1.4 **Phase and group velocities**

For wave trains containing more than one frequency, in a visco-elastic medium, the **phase velocity** is a function of the frequency $c(\omega)$ or wave number $c(k)$. This implies that the wave number is a function of frequency $k(\omega)$ and vice versa for $\omega(k)$. In this case, we have the phenomenon of wave dispersion and can define the **group velocity** as:

$$v = \frac{d\omega}{dk} \quad (2\text{-}23)$$

This velocity is referred to a packets or groups of waves. If we substitute $\omega = ck$, we obtain the relation between phase and group velocities:

$$v = c + k\frac{dc}{dk} \quad (2\text{-}24)$$

2.1.5 **Surface waves**

Surface waves are generated in the presence of a free boundary, such as the surface of the Earth, or along the interface between two different elastic media, and propagate parallel to this interface.

Several types of surface waves exist and can be classified with respect to the polarization of the ground motion associated with the propagation: **Rayleigh waves** involve elliptical motion in the vertical plane containing the wave propagation direction (Figure 2-3); **Love waves** involve transverse motion (Figure 2-4); Scholte waves propagate at the earth/water interface, and should thus be used for underwater surface wave analysis.

Rayleigh waves result from the interaction of P-waves and SV-waves with the surface of the earth (*Aki & Richards, 1980*). The particle motion of Rayleigh waves has both a vertical and a horizontal component and is reminiscent of rolling ocean waves (*Rayleigh, 1885; Aki & Richards, 1980; Kramer, 1996*). The wave motion is retrograde (anticlockwise) closest to the surface, but becomes prograde (clockwise) at greater depths.

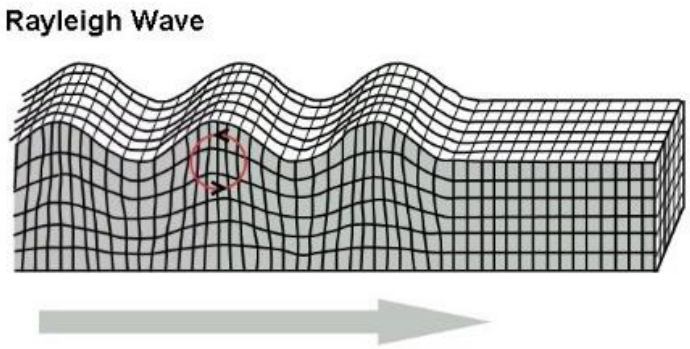

Figure 2-3: Particle motion associated with Rayleigh waves

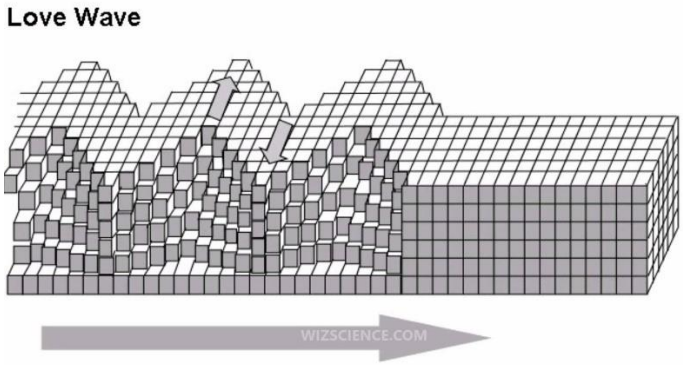

Figure 2-4: Particle motion associated with Love waves

In a homogeneous half-space, the Rayleigh wave velocity is independent of frequency, i.e. Rayleigh waves are non dispersive in a homogeneous medium, whereas for a point load, the rate of spatial decay is proportional to the inverse of the square root of the distance from the source. Conversely, for a point source, the geometric attenuation factor of body waves propagating along the boundary of an elastic half-space is proportional to the inverse of the square of the distance (*Ewing et al. 1957*). Thus, at distances on the order of one to two wavelengths from the source, the contribution of body waves becomes negligible, and the wave field is dominated by Rayleigh waves (**Figure 2-6**).

In the direction orthogonal to that of propagation, the displacement field generated by a surface wave decays exponentially because no energy is propagated in the interior of the half-space (**Figure 2-5**). It can be shown that most of the strain energy associated with surface wave motion is confined within a depth of about one wavelength λ from the free boundary (*Achenbach 1984*). Hence, Rayleigh waves with long wavelengths penetrate deep into the interior of a medium. Because wavelengths are proportional to the inverse of frequency in harmonic waves, this statement can be interpreted as follows: high-frequency waves are confined to shallow depths within the medium, whereas low-frequency components involve motion also at large depths.

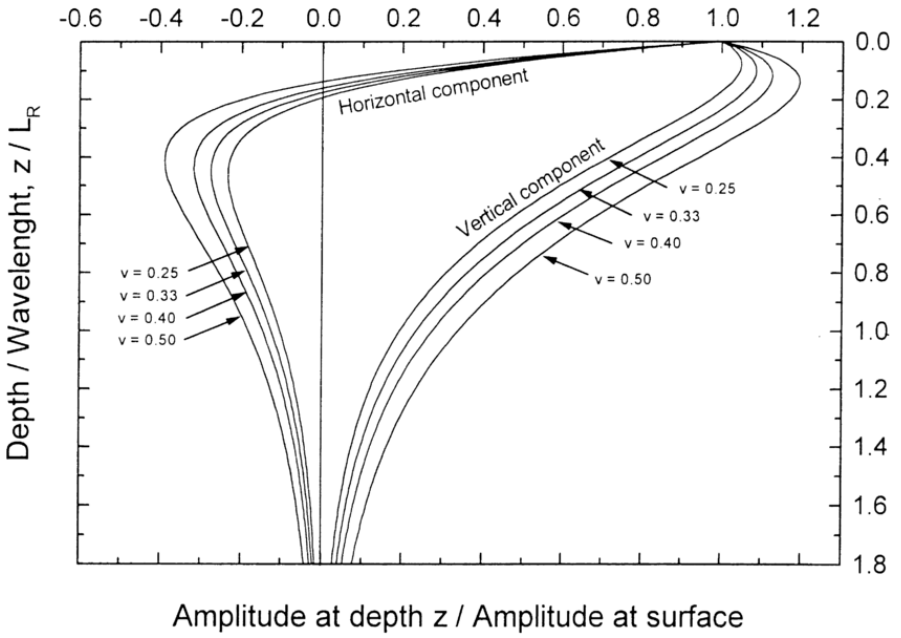

Figure 2-5: Displacement amplitude of Rayleigh waves versus dimensionless depth (Richart et al., 1970).

In vertically heterogeneous media, surface wave propagation is governed by geometric dispersion: harmonic waves of different wavelengths k propagate within different depth ranges and, hence, for each wavelength the phase velocity v depends on the elastic properties and density of the subsurface within the propagation depth range. Distribution of phase velocities as a function of frequency or wavelength is called a dispersion curve. In vertically heterogeneous media with increasing velocity (both V_S and V_P) with depth, the velocity of propagation of surface waves decreases for increasing frequency (normally dispersive profiles).

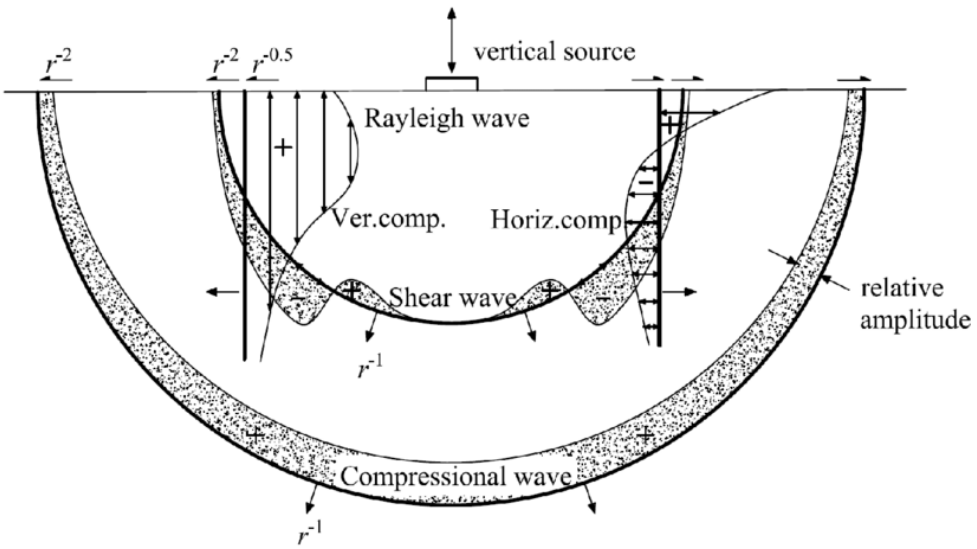

Figure 2-6: Distribution of compressional, shear and Rayleigh waves generated by a point load in a homogeneous, isotropic, elastic half-space (Woods, 1968).

Typically, multiple phase velocities exist for a given frequency, making the dispersion curve multimodal. The mode with the lowest phase velocity (at each frequency) is referred to as the fundamental mode. at each frequency, larger than a well-defined cut-off frequency, different modes of vibration exist (*Aki & Richards, 1970*). Each mode is characterized by its own propagation velocity, which always increases from the fundamental to the higher modes (overtones).

The propagation velocity of Rayleigh waves is proportional to the value assumed by the S-waves and approximately given by the following relation (*Viktorov, 1967*):

$$V_R \cong \frac{0{,}87 + 1{,}12v}{1 + v} V_S \qquad (2\text{-}25)$$

2.2 Attenuation theory

The main focus of this section, is a general overview of the attenuation theory and then the constitutive models adapted in literature.

Mainly, seismic attenuation is caused by three physical phenomena:

- **Intrinsic attenuation**: the energy dissipated in heat due to internal friction during the passage of the elastic wave;
- **Geometrical spreading**: it is the decrease of the energy density that occurs in the expansion of the elastic wave front, due to the fact that the energy irradiation takes place on a greater volume at increasing distances from the source, Theory and numerical model studies (*Haterly, 1986*) show that in most cases geometrical spreading is a complicated phenomenon, especially near the source; methods like amplitude decay appeared to be very sensitive to geometrical spreading (*Jongmans, 1990*); accurate studies on geometrical spreading effects can be found on Morozov (*2008, 2010*);
- **Scattering**: scattering phenomena are produced by reflection, refraction, and conversion of elastic energy due to the irregularities and discontinuities present in the medium.

2.2.1 The quality factor Q

Wave propagation, implies a variation of motion in space and time. Thus, attenuation of wave motion can be observed in time or in space. For a given location wave motion is attenuated with time and for a given time, it is attenuated with distance. For wave motion, we can define the **damping ratio** $D(\omega)$ as a function of frequency in the form:

$$D(\omega) = \left(\frac{1}{4\pi}\right)\frac{\Delta E}{E} \qquad (2\text{-}26)$$

In this definition, D represents the **material damping ratio** of the elastic energy ΔE dissipated during one cycle of harmonic motion of frequency ω due to imperfections in the elasticity of the material and the maximum or the mean energy E accumulated during the same cycle.

Another parameter related to the material damping, which is largely used by geophysicists and seismologists is the **quality factor** Q, that is related to the material damping D as follows:

$$Q(\omega) = \frac{1}{2D(\omega)} = (2\pi)\frac{E}{\Delta E} \qquad (2\text{-}27)$$

The Q factor may also be defined as the tangent of the phase lag between stress and strain, which are linked by the modulus (*Wang, 2006*).

The measured or effective Q is a combination of intrinsic Q of the rocks and apparent Q by elastic scattering as follow (*Lerche and Menke 1986; Spencer et al., 1986*):

$$\frac{1}{Q_{eff}} = \frac{1}{Q_{int}} + \frac{1}{Q_{sca}} \qquad (2\text{-}28)$$

The scattering attenuation Q_{sca}^{-1} (sometimes called extrinsic attenuation (*e.g., in Virieux and Operto, 2009*)) and intrinsic attenuation Q_{int}^{-1} are significant to interpret the geology and tectonics of an area (*Blair, 1990; White, 1992; Barton, 2007*).

If we consider an harmonic wave of amplitude A that is attenuated so that, after one period or one wave length, its amplitude is $Aexp(-\pi/Q)$, then, since the energy is proportional to the square of the amplitude, the energy dissipated in one cycle is (*Udías, 2017*):

$$\Delta E = A^2\left[1 - \exp\left(-\frac{2\pi}{Q}\right)\right] \qquad (2\text{-}29)$$

By using the ratio $\Delta E/E$, we obtain the equation (2-27). By using the amplitude ratio $\Delta A/A$, we define for wave propagation:

$$\frac{1}{Q} = \frac{1}{\pi}\frac{\Delta A}{A} \qquad (2\text{-}30)$$

Since wave phenomena can be considered as a variation in time or space, we can define **temporal** (Q_t) and **spatial** (Q_e) quality factors. Q_t represents the wave attenuation with time during one period for a fixed point in space and Q_e represents the attenuation at a given time along wavelength distance.

Wave attenuation is usually indicated by assigning complex values to the frequency and wavenumber. For a harmonic elastic wave we have:

$$u(x,t) = Aexp[i(k'x - \omega' t)] \qquad (2\text{-}31)$$

where the wavenumber and frequency are now complex quantities:

$$k' = k + ik^* \quad (2\text{-}32)$$

$$\omega' = \omega + i\omega^* \quad (2\text{-}33)$$

According to definitions of Q_t and Q_e we can easily deduce that:

$$\frac{1}{Q_t} = \frac{2\omega^*}{\omega} \quad (2\text{-}34)$$

$$\frac{1}{Q_e} = \frac{2k^*}{k} \quad (2\text{-}35)$$

2.2.1.1 **Frequency dependence**

Many studies on body, surface and coda waves describe attenuation depending on frequency adopting the visco-elastic model, this bond is commonly represented in an exponential type of quality factor Q:

$$Q(f) = Q_0 \left(\frac{f}{f_0}\right)^{\eta} \quad (2\text{-}36)$$

where η is a constant usually between $-1 < \eta < 1$ (*Li et al. 2016*), f_0 is a reference frequency of 1 Hz, while Q_0 is the corresponding value of the quality factor (*Aki and Chouet, 1975*). The values of Q (considering a $\eta > 0$, while very high values are not very common) tend to increase as the frequency increases. Another common hypothesis is that Q is independent of frequency at least in a limited frequency band (*Johnston et al., 1979*).

At the time of Knopoff's review (*1964*) it was customary to assume that Q was substantially independent of frequency. His assumptions of 'a homogeneous sample' and 'at low frequencies' are clearly important in view of what is now understood about potential dissipation mechanisms in microcracked rock samples or in rock masses with sets of bedding planes and/or joints. Laboratory experiments on many homogeneous solids had shown that up to moderately high frequencies, the dimensionless quantity Q was virtually independent of frequency. This preliminary conclusion indicated that the mechanism by which energy has removed from elastic waves in solids was not the same as the mechanism for attenuation in liquids, where attenuation is frequency dependent (*Barton, 2007*). Some physical phenomena such as viscous relaxation, irregular saturation, squirt flow, scattering, etc., are related to Q dependence on frequency.

Some typical values of Q for longitudinal excitation of various solids, selected from Knopoff, (*1964*) are reported below:

Material	Q

Steel	5000
Copper	2140
Silica	1250
Glass	490
Diorite	125
Limestone	110
Lead	36
Sandstone	21
Shale	10
Celluloid	7

Table 2-2: Some examples of Q for longitudinal or bending excitation of various solids (Knopoff,1964), sorted by magnitude.

2.2.1.2 10 Hz Transition problem

Measurements of Q_S carried out at seismogenethic depths and using coda waves show only a weak increase with the frequency between 10 and 100 Hz. Combining these results with those coming from near-surface studies at low frequency, a significant change in Q_S frequency dependence around 10 Hz in the active tectonic regions, passing from low values of Q_0 and high values of η (> 1) to large values of Q_0 and moderate values of η (η~$0.2 \div 0.3$), exceeded this value of frequency. This change is called by the authors the "10 Hz transition problem" (*Abercrombie, 1998*). It could be due to changes in the nature of the earth's crust in the most superficial layers (few hundred meters), or simply to a wrong hypothesis in the model used for the estimation of Q. In Morozov (*2008*) the problem of the 10 Hz transition and the absorption band is substantially attributed to some deviations from the geometric attenuation law.

Alternatively, the variation observed in the Q frequency dependence is able to provide important information about the nature of the earth's crust itself according to different scales.

In Abercrombie (*1998*) a weak increase in Q_S is observed with frequency (from about 500 to 10Hz up to 1200 to 100Hz). Various studies (*Abercrombie, 1997; Jongmans and Malin 1996*), considering a near-surface analysis, show low values of Q (about 10 in the first 100 meters of land), which grow rapidly with depth, and independent or weakly dependent from the frequency, in the range $f \sim 2 \div 100$. The attenuation in this case is rather independent even from the rock type (*Abercrombie, 1998*). These combined observations suggest that the main cause of surface attenuation is the opening of the microfractures with a consequent decrease in the lithostatic pressure.

2.2.1.3 Attenuation in rocks

As the wave propagates thorugh the material, the normal stress between the crack-faces increases, and thus the frictional shear stress also increases. As the wave passes, the direction of the frictional shear stress is reversed, and again work must be done against friction as the crack returns to its equilibrium position (*Barton, 2007*). Clearly, micro-scale deformations are implied here. Numerous mechanisms have been proposed to explain

attenuation of seismic waves in rock and in rock masses. Johnston et al., 1979 listed the following in their landmark paper:

- Matrix anelasticity;
- Frictional dissipation due to relative motions at grain boundaries and across crack surfaces (*Walsh, 1966*);
- Fluid flow causing relaxation due to shear motions at pore-fluid boundaries;
- Relative motion of the matrix frame with respect to the fluid inclusions in the case of fully saturated rock (*Biot, 1956a*);
- Squirt phenomena (*Mavko and Nur, 1975 and O'Connel and Budianski, 1977*);
- Gas pockets squeezing when only partial saturation;
- Geometrical effects due to small pores, larger irregularities, thin beds (this category obviously extends to major discontinuities, faults, rock boundaries, dykes etc.).

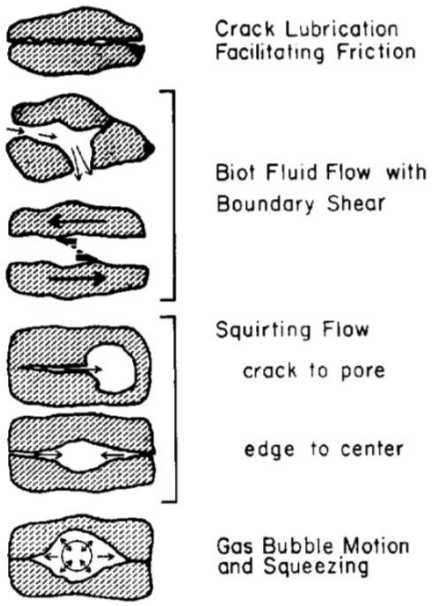

Figure 2.7: Schematic illustration of several proposed aitenuation mechanisms for saturated and partially saturated rocks (Johnston, 1979)

2.2.2 **Attenuation in body waves**

The attenuation in body waves can be expressed by taking complex values for velocities of P and S waves, namely $\alpha' = \alpha + i\alpha^*$ and $\beta' = \beta + i\beta^*$. Since the attenuation of body waves is measured from amplitude at various distances, the imaginary part of velocities are related to the spatial quality factor Q_e. For P and S waves we can define quality factors in a similar way:

$$\frac{1}{Q_\alpha} = \frac{2\alpha^*}{\alpha} \qquad (2\text{-}37)$$

$$\frac{1}{Q_\beta} = \frac{2\beta^*}{\beta} \qquad (2\text{-}38)$$

The complex velocities can now be expressed in terms of the corresponding Q factors:

$$\alpha' = \alpha\left(1 + \frac{i}{2Q_\alpha}\right) \qquad (2\text{-}39)$$

$$\beta' = \beta\left(1 + \frac{i}{2Q_\beta}\right) \qquad (2\text{-}40)$$

In most seismologic problems, it is assumed that the relation between P and S quality factors in similar to (*Udías, 2017*):

$$\frac{1}{Q_\alpha} = \frac{4}{3}\left(\frac{\beta}{\alpha}\right)^2 \frac{1}{Q_\beta} \qquad (2\text{-}41)$$

If $v = 0.25$ and $\alpha = \sqrt{3}\beta$ the relations gives $Q_\alpha = 9/4Q_\beta$.

Following the ray theory, the attenuation of the amplitude of a monochromatic P wave in the Earth's interior, become in a dispersive wave equation, given by:

$$A = A_0 \exp\left(-\frac{\omega s}{2\alpha Q_\alpha}\right) = A_0 e^{-\omega t^*} \qquad (2\text{-}42)$$

Where A and A_0 are the amplitudes at the observation point and the focus, and s is the distance traveled along the ray. For an homogeneous medium $t^* = t/(2Q_\alpha)$, where $t = s/\alpha$ is the traveling time of P waves. The path attenuation factor t^* in the exponent of equation (2-42) is often used in body-wave analysis (*Der and Lees, 1985*). This equation can be expressed for S waves in a similar way, substituting β and Q_β.

Existence of t^*or Q as attenuation properties is based on common observations that the negative exponent in the amplitude-decay expression increases with f and accumulates with t (*Morozov, 2015*).

Following Johnston, (*1979*) the attenuation is determined from the amplitude ratios of waves observed at a different distance. For body waves, we need observations along similar ray paths, so that the attenuation of amplitude is referred to a certain distance Δs along the ray inside the Earth. In an approximate form, the attenuation with epicentral distance between two stations may be found from:

$$\ln\left(\frac{A_2(\omega)}{A_1(\omega)}\right) = \ln C - \gamma(\omega)\Delta x \qquad (2\text{-}43)$$

Where $\gamma(\omega) = \omega\Delta x/(2\alpha Q) = \pi f/Q$ is the overall attenuation of amplitude with horizontal distance and C depends on the geometrical spreading. This equation illustates

the difference between the influences of Q geometrical spreading and anlelastic attenuation on the decrease in amplitude with distance.

The attenuation coefficient, γ, is a quantity which measures energy absorption, and can be expressed in terms of wavelength λ as:

$$\gamma = \frac{\pi}{\lambda Q}(nepers/unit\ length) = \frac{20\pi}{(ln10)Q}(db/\lambda) \qquad (2\text{-}44)$$

which leads to the approximation mentioned above; that is, $27.3Q\ db$ per wavelength (*Johnston and Toksöz, 1979*).

2.2.3 **Attenuation in surface waves**

Following equations (2-39) and (2-40), the frequency-dependent complex wavenumber k_n^* defines the propagation of dispersive surface wave modes in linear viscoelastic media. As introduce in the equation (2-32), the phase velocity and the attenuation constant for the nth mode are related to the complex wavenumber by:

$$k_n^* = Re(k_n^*) + Im(k_n^*) = k_n - i\gamma_n = \frac{\omega}{v_n} - i\gamma_n \qquad (2\text{-}45)$$

The real part of the wavenumber is the physical wavenumber k_n, a function of the real physical phase velocity v_n; the imaginary part of the complex wavenumber is the **attenuation constant**, associated with the nth mode of propagation (*Aki and Richards, 1980*. The asterisk indicates complex numbers.

. The frequency-dependent attenuation constant γ_n is the coefficient of the exponential function describing the spatial decay of the spectral amplitude for a single mode in the far-field (*Strobbia, 2014*). The real and imaginary parts of the complex wavenumber are linked by the Kramers-Kronig relation, and have to be Hilbert transform pairs tosatisfy the principle of causality (*Bracewell, 1965; Tschoegl, 1989*). This is used in the solution of the forward problem (*Lai and Rix, 2002*).

$$A_n(\omega, r) = A_{n,0}(\omega)\frac{1}{\sqrt{r}}e^{-\gamma_n(\omega)r} \qquad (2\text{-}46)$$

where r is the source to receiver distance.

The spatial decay of the wave amplitude, due to the geometrical spreading, is represented by the square root of the distance, for each mode.

In a medium with homogeneous velocity and intrinsic absorption, both wavenumber and attenuation coefficient are frequency dependent. A representation showing the relationship with the material properties can be obtained using two different parameters, derived from the real and imaginary part of the wavenumber.

The first one is the modal phase velocity, definite as:

$$v_n = \frac{\omega}{Re(k_n)} \qquad (2\text{-}47)$$

It has a more intuitive and direct relationship with the layer velocities. The attenuation coefficient is a wave propagation parameter; it describes the spatial amplitude decay of the surface wave as it propagates in an anelastic medium. The intrinsic material energy dissipation can be measured using different parameters.

The second parameter is the Rayleigh modal **phase damping ratio** (*Misbah and Strobbia, 2014*), typically used in soil dynamics, which is defined using an analogy with the body wave damping ratio in a viscoelastic medium, as:

$$D(\omega) = \frac{Im(k^{*2})}{2 \cdot Re(k^{*2})} \qquad (2\text{-}48)$$

The Rayleigh phase damping ratio is a modal property, related to the damping ratio of the subsurface layers, that is more directly related to the material absorption.

As an alternative to the phase damping ratio, it is possible to define a phase quality factor Q, related to the subsurface quality factor (*Carcione et al., 1988*), as:

$$Q(\omega) = \frac{Re(k^{*2})}{Im(k^{*2})} \qquad (2\text{-}49)$$

Chapter 3.
Experimental and theoretical attenuation measurements of body and surface waves

3.1 Body waves methods

3.1.1 Review of methods

Two different methods are presented to estimate seismic attenuation from borehole surveys, other existing method that have used borehole surveys are listed in the table below (Table 3-1). The first one is the **rise-time** method which operates in time domain and the second is the **spectral ratio** methods which is defined in the frequency domain. Many reviews of such methods exist in literature, consisting in a comparison between these two or even more methods (*Tonn, 1991; Janssen et al., 1985; Cheng and Margrave, 2012*). In this chapter I have first attached a synthetic review (table 3-1) of the various methods appearing in the literature on seismic attenuation estimation using body waves, that can be allied on borehole or surface seismic surveys, giving the complete theoretical basis of the two methods which are used in the experiments presented later on in this thesis. In spite of the broad variety of methods available for Q-computations, only a few techniques such as the rise-time method or the spectral ratio method are widely accepted for borehole studies. These methods are more robust and unaffected by far-field geometric spreading. My review does not cover the methods employing coda waves which are mainly based on seismological (earthquake) recordings (*Aki and Chouet, 1975*).

Method	Code	Domain	Reference
Amplitude decay	AD	x-t	-
Analytical signal	AS	x-t	Engelhard et al. (1986)
Wavelet modelling	WM	x-t	Jannsen et al. (1985)
Phase modelling	PM	x-t	-
Frequency modelling	FM	x-t	-
Rise-time	RT	x-t	Gladwin and Stacey (1974)
Pulse amplitude method	PA	x-t	Kjartansson (1979)

Beam Forming	BF	x-t	White (1988)
Matching technique	MT	x-ω	Raikes and White (1984)
Spectral modelling	SM	x-ω	Jannsen et al. (1985)
Spectral ratio method	SR	x-ω	Bath (1974), Teng (1968)
Centroid Frequency Shift	CFS	x-ω	Quan and Harris (1997)
Peak Frequency Shift	PFS	x-ω	Zhang ed Ulrych (2002)
Dominant and Central frequency shift	DCFS	x-ω	Li et al. (2015)

Table 3-1: Review methods to estimate seismic attenuation through borehole surveys

3.1.2 **Time domain methods**

3.1.2.1 **Rise-time method**

The rise-time method is a time-domain method based on the broadening of the pulse resulting from the attenuation of the high-frequency components. An empirical mathematical model for pulse broadening in an inhomogeneous medium has been suggested by Gladwin and Stacey (*1974*) and Stacey et al. (*1975*) and supported theoretically by Kjartansson (*1979*).

Gladwin and Stacey (*1974*) defined the rise-time (τ) as the "interval between the intersections of the steepest rise of a pulse onset with zero level and peak pulse amplitude". Or, alternatively, the ratio of the maximum peak amplitude to the maximum slope of the first quarter-cycle of the pulse.

Gladwin and Stacey (*1974*) proposed a rise-time principle indicated by the following equation:

$$\tau = \tau_0 + C \int_{ray} \frac{ds}{vQ} = \tau_0 + C \int_{ray} \frac{dT}{Q} \qquad (3\text{-}1)$$

where τ is the rise-time of the first arrival waveform, τ_0 is the origin pulse rise-time at the source (*Stacey et al.* used zero for this term), v is the velocity, dS is the segment along the ray path, dT is the travel time, Q is the quality factor and C is a constant. The velocity and quality factor vary with the position r of the receivers.

The rise-time, defined on displacement records, is approximately the pulse width used by Zucca et al. (*1994*) on recorded seismograms. The pulse width, or rise-time,τ, is the time difference from the onset of initial arrival to initial peak for displacement seismograms, or, equivalently, from on set to first zero crossing for velocity records or to second zero crossing for acceleration seismograms. In practice, the onset of a signal can be difficult to determine precisely in the presence of noise. Even for noise-free seismograms, bandwidth limitations can make picking the on-set difficult. For short pulse widths, the error introduced by mis-picking can be large and unacceptable (*Wu and Lees, 1996*).

As the seismic wave travels through the medium, dispersion causes pulse spreading, this process is well established for optical fiber studies, as in **Figure 3.1**.

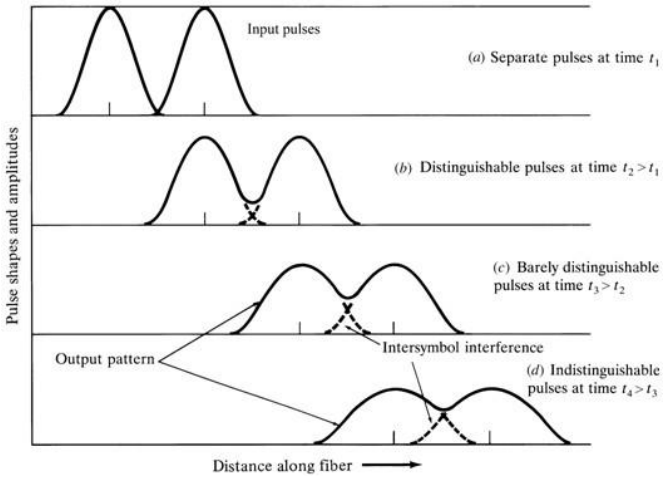

Figure 3.1: Broadening and attenuation of two adjacent pulses as they travel along a fiber.

The same phenomena occur on a seismic wave travelling through the earth.

Kjartansson (*1979*) indicated several ways to measure the pulse widths, as showed in **Figure 3.2**:

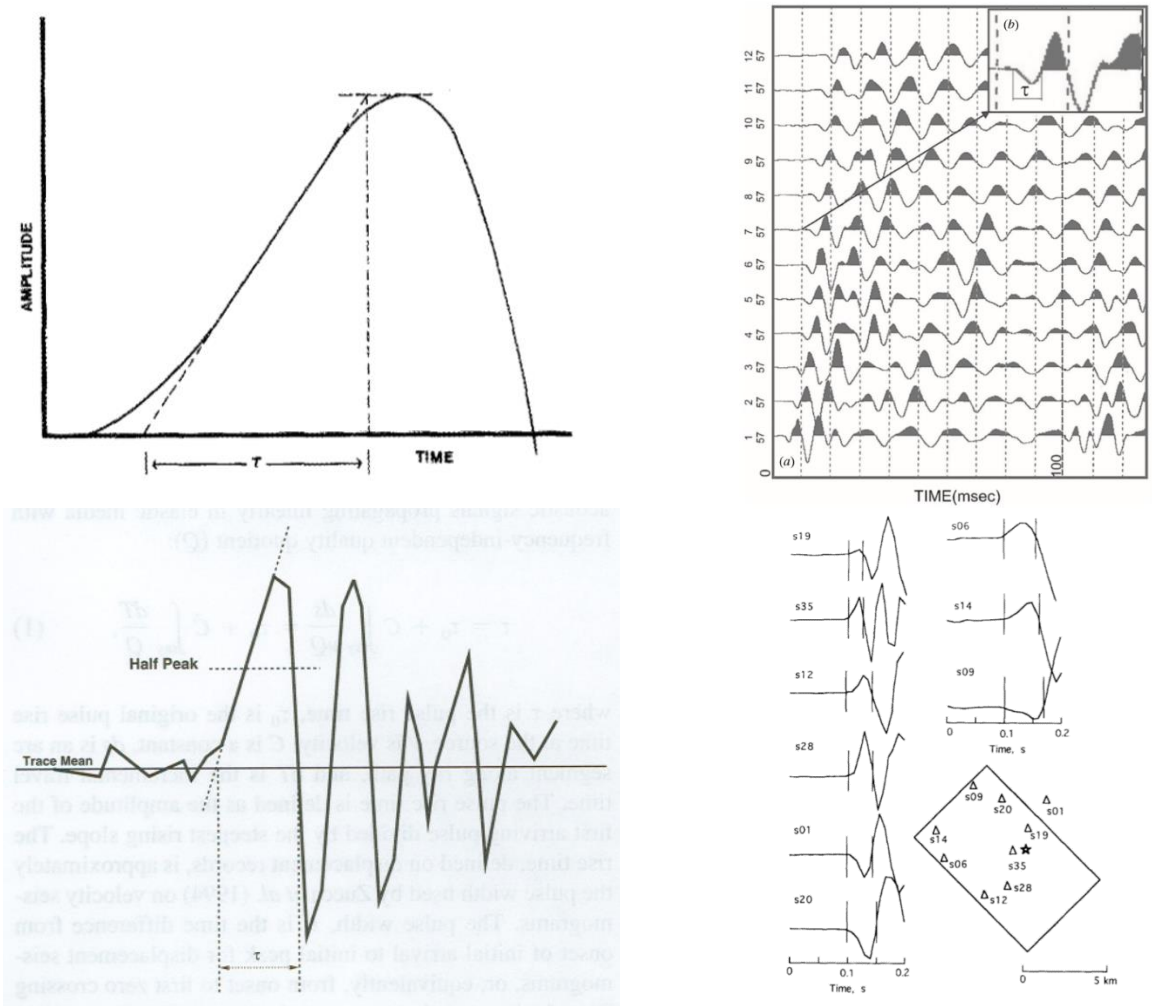

Figure 3.2: Rise-time τ of a pulse is in lectirature: a) from Gladwin and Stacey, 1974; b) from Kurtuluş and Sertçelik, 2010; c) Wu and Lees, 1996; d) Zucca et al., 1996.

In this study, we used a near-surface VSP (Vertical Seismic Profiling; *Balch et al., 1982*) data records; measurements based on the first quarter-cycle of the pulse should be used to avoid interference with the later cycles of the pulse. Suitable measures, therefore, are the pulse rise-time calculated as the maximum amplitude divided by maximum slope, as the separation between the first inflection point and the first peak. An example of one rise-time has showed in **figure 3.3**. The experimental procedure will be showed in detail in chapter 4.

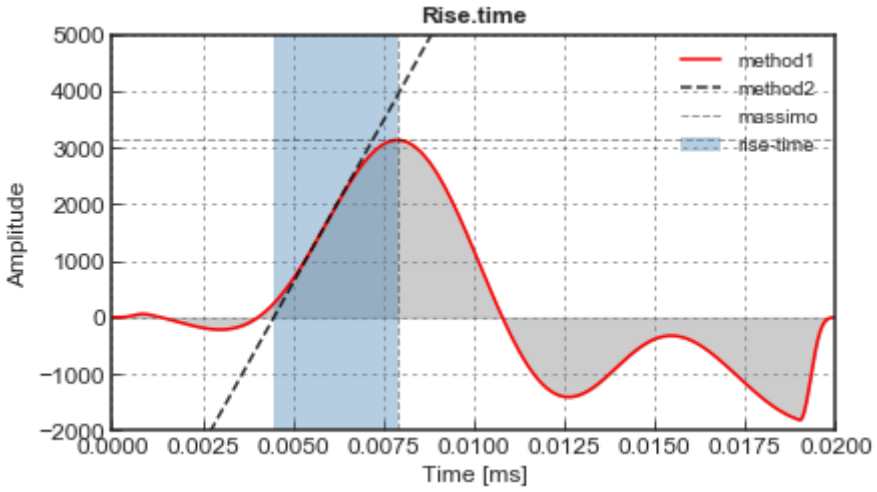

Figure 3.3: Example of a rise-time measurement of a single P-wave trace at 41 meter depths in Rieti site.

Assuming a homogeneous $Q = Q_0$, equation (3-1) becomes a linear relation:

$$\tau = \tau_0 + \frac{CT}{Q_0} \qquad (3\text{-}2)$$

The constant C in (3-2) was first determined experimentally (*Gladwin and Stacey, 1974*) for ultrasonic acoustic pulses in the kilohertz frequency band to be 0.5, and a rigorous theoretical justification was supplied later (*Kjartansson, 1979*). According to Kjartansson's (*1979*) theory of impulsive displacement sources, the rise-time of recorded displacement, velocity, and acceleration seismograms obey the relation (3-2), although with different constants C. For > 30 ,C will take on values of 0.485, 0.298, and 0.217 for displacement, velocity, and acceleration records, respectively (*Blair and Spathis,1982*). Blair and Spathis (*1982*) further suggested that C can take on different values for different sources.

The main advantage of the pulse-broadening or rise-time method is that only a very short time-length of the seismogram is required for processing, by the time we use only the first quarter cycle, (*Kurtuluş and Sertçelik, 2010*). Hatherly (*1986*) found that the measurement of the pulse width appears to be suitable even for use with shallow seismic refraction data.

3.1.3 **Frequency domain methods**

3.1.3.1 **Spectral ratio method**

The second method used in this study is the spectral ratio method. The method in the frequency domain has been used widely for estimating the seismic attenuation (*Teng, 1968; Jongmans, 1982, Badri and Mooney, 1987; Sarma and Ravikumar, 2000; Abercrombie 2000; etc..*). The method is based on the spectral amplitude ratio at two different distances.

Considering the wave propagation expression:

$$U(x,\omega) = U_0(\omega)\exp[-\alpha(\omega)x]\exp\left[i\omega\left(t - \frac{x}{v(\omega)}\right)\right] \quad (3\text{-}3)$$

And taking only amplitude attenuation we obtain:

$$A(\omega) = A_0(\omega)\exp[-\gamma(\omega)x] \quad (3\text{-}4)$$

where $A(\omega)$ is the amplitude spectrum of the trace at receiver depth , z and $A_0(\omega)$ at a shallower depth z_0. The amplitude $A(\omega)$ is decayed exponentially from a reference amplitude $A_0(\omega)$. $\gamma(\omega)$ is the attenuation coefficient that can be expressed in different ways as:

$$\gamma(\omega) = \frac{\pi f}{vQ} = \frac{\pi}{v\lambda} = \frac{\omega}{2vQ} = \frac{\omega(t-t_0)}{2Q} \quad (3\text{-}5)$$

where v is the velocity, λ is the wavelenght, f is the frequency in Hz, ω is the frequency in radiants and $\tau = (t - t_0)$ is the time delay between two first arrival at two different distance (depths) z and z_0.

In general case $A(\omega)$ can be expressed as a product of the source function $A_0(\omega)$ with a number of transfer functions, each for an appropriate portion of the transmitting medium. It includes: instrumental transfer function, crustal transfer function and geometrical transfer function. Considering only geometrical transfer function the equation (3-4) becomes:

$$A(\omega) = A_0(\omega)G_0(t)\exp[-\gamma(\omega)x] \quad (3\text{-}6)$$

where $G(t)$ is the geometrical factor that includes spreading, reflections, etc..

Considering the ratio of the Fourier spectral amplitudes we obtain:

$$\frac{A(\omega)}{A_0(\omega)}\frac{G(\omega)}{G_0(\omega)}\exp[-(\gamma_0(\omega) - \gamma(\omega))x] \quad (3\text{-}7)$$

and applying simple logarithmic properties we can obtain:

$$\ln\left[\frac{A(\omega)}{A_0(\omega)}\right] = \ln\left[\frac{G(\omega)}{G_0(\omega)}\right] + (\gamma(\omega) - \gamma_0(\omega))x \quad (3\text{-}8)$$

where the term on the left side of the equation is called **reduced spectral ratio**, the ratio $\ln[G(\omega)/G_0(\omega)]$ is frequency-independent. This simple result shows that the reduced spectral ratio is a linear function of frequency (*Teng, 1968*).

For typical rocks where $Q = 10 \div 100$, the term $\ln[G(\omega)/G_0(\omega)]$ is negligible (*Sarma and Ravikumar 2000*). Now, the decay of the amplitude at certain distance from source is measured using the simplified spectral ratio method:

$$\ln\left[\frac{A(\omega)}{A_0(\omega)}\right] = -\frac{\omega(t-t_0)}{2Q} = -\frac{\pi f(t-t_0)}{2Q} \qquad (3\text{-}9)$$

Measuring the slope of the spectral ratio:

$$m = \frac{1}{\omega}\ln\left[\frac{A(\omega)}{A_0(\omega)}\right] = \frac{2\pi}{f}\ln\left[\frac{A(\omega)}{A_0(\omega)}\right] \qquad (3\text{-}10)$$

The slope m, is called **differential attenuation**, and contains all the information concerning the difference of wave attenuation along two different rays; can be found from the slope of the line fitted to $\ln[A(\omega)/A_0(\omega)]$ versus frequency f, as shown in the **figure 3.4**.

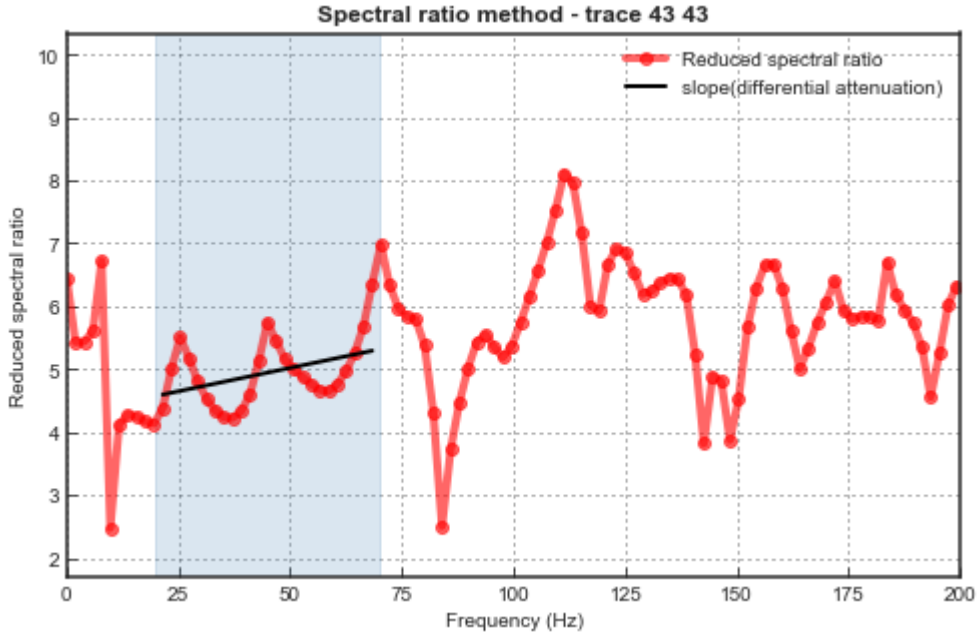

Figure 3.4: Slope estimation on reduced spectral ratio. The frequency band considered is 20-65 Hz for S-waves (Rieti site).

The Q value between z and z_0 is then estimated as:

$$Q^{-1}(z-z_0) = -\frac{2m}{\tau} \qquad (3\text{-}11)$$

For in-situ measured seismograms, the method consists in calculating the Fourier transform of two signals and then the logarithmic ratio for each frequency. Since m is independent of frequency, Q can be determined from the slope of the line fitted to A vs. f The geometrical spreading factor, appearing only in the intercept b, must not be preliminarily known for Q determinations. The estimates of m derived from this regression is a random quantity dependent on the sampling of the spectra and possess statistical errors (*White, 1992*).

In chapter 4, we attempt to improve the Q estimation by means of a near-surface VSP data, with an accurate determination of the time delay, processing, and finally a robust estimation of Q values for P and S waves in two different sites.

3.2 **Surface waves methods**

The main objective in surface wave testing is to extract information about the **geometrical dispersion** of surface waves from observations of particle motion at two or more receiver locations, associated with the intrinsic energy dissipation caused by material damping.

Attenuation and dispersion analysis of surface waves is generally performed like a standard MASW (Multichannel Analysis of Surface Waves) test, on multichannel measurements acquired using a linear array of receivers and an active source. The procedure requires accurate measurements of the amplitude of the surface wave particle motion because it contains information about attenuation and geometrical spreading. It is essential that the effects of noise are considered and that the amplitude perturbations are minimized. Verticality and physical coupling of each receiver should be checked carefully. Moreover, a previous accurate calibration of the receivers used in the shotgather is needed to guarantee a uniform array response.

The estimation of the intrinsic attenuation component can be used to assess the dissipative properties of the medium, typically assuming a viscoelastic constitutive model.

Such information is usually presented in the form of dispersion curves showing the variation of the attenuation coefficient versus frequency.

The purpose of our dispersion and attenuation analysis is to extract the information about geometric dispersion and spatial attenuation of the particle motion from acquired multichannel surface waves testing (an example is shown in figure **3.5**). To this end, I implemented several analysis techniques in PYTHON to extract experimental dispersion and attenuation curves from recorded seismograms.

This chapter briefly summarizes the methods used to estimate experimental attenuation curves and focuses attention on the method proposed by Kudo and Shima (*1970*) and more recently by Xia et al. (*2002*). This method produces only the fundamental mode attenuation curve.

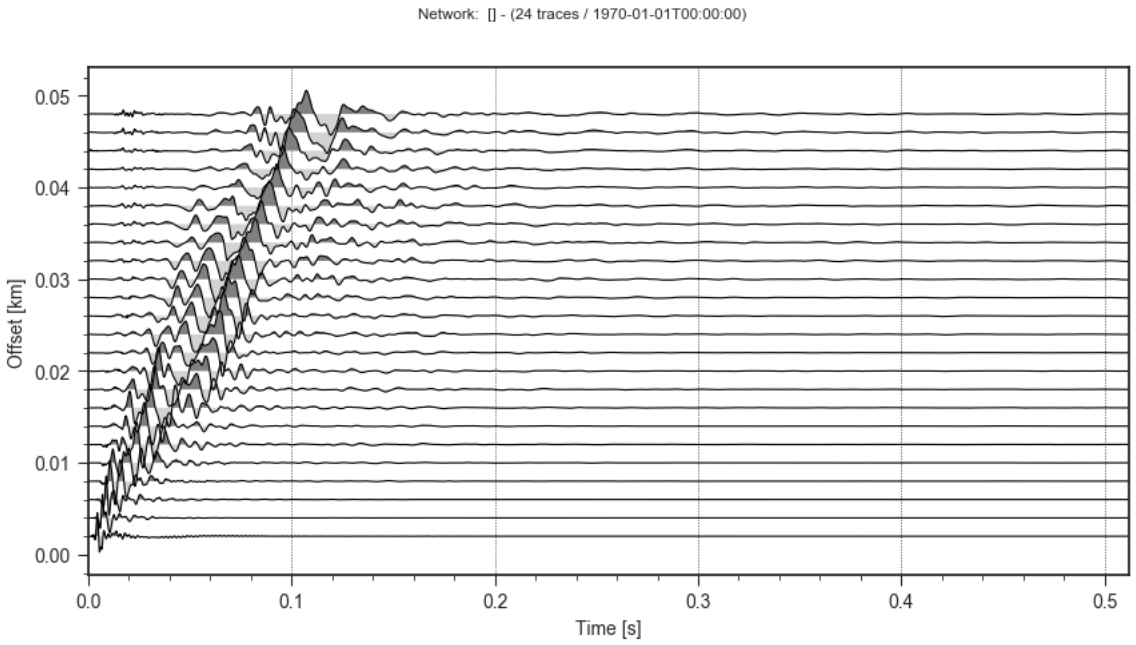

Figure 3.5: 24-channel shot gather obtained in the test site of Velino River in June 2018.

3.2.1 **Experimental dispersion curves**

In addition to the methods to estimate attenuation curves, the methods used to extract experimental phase velocity dispersion curves may be classified according to the procedure adopted (*Foti et al., 2014*):

- Direct assessments of the **propagation parameters,** e.g., wavelength in the steady-state Rayleigh method or phase delay in the two-station spectral analysis of surface waves (SASW);
- **Regression methods**, in which the propagation parameters are obtained by fitting the experimental data with the expected theoretical functions such as: multi-offset phase analysis (MOPA, *Foti and Strobbia, 2006*), spatial autocorrelation (SPAC, *Aki (1957); Chávez-García et al. (2005)*), transfer function;
- **Transform-based methods**, in which the experimental data are transformed from the original space–time domain into a different domain in which the propagation parameters are identified as spectral maxima (e.g., frequency–wavenumber, frequency–slowness, frequency–velocity analysis).

For active MASW experiments I implemented a PYTHON version of the **Phase shift method**, that compute dispersion data using a transformation described in Park et al. (1998).

Other methods utilized to compute dispersion curves are **f-k method**, that compute dispersion data using a standard frequency-wavenumber transformation (i.e., convert the data from space-time to frequency-wavenumber domain using a two-dimensional Fast Fourier Transformation), **fdbf** (Frequency Domain Beamformer), that compute dispersion data using frequency domain beamformer (*Foti et al. 2014*), and **tau-p**, that compute dispersion data using a slant-stack (linear Radon) transform (*McMechan and Yedlin, 1981*).

3.2.2 **Review of methods for estimation of attenuation curves**

In the case of surface waves testing, the Q structure cannot be estimated in a straightforward way, but we need to apply an inversion. This chapter is a quick review of the most utilized methods to estimate experimental attenuation curves (attenuation coefficients) from surface waves data. Kudo and Shima method (*1970*) has been adopted for our purposes, in order to extract experimental attenuation curves. For the experimental dispersion curves, as mentioned before, I implemented Phase shift method. It is proved that phase shift method is able to produce the best results in terms of accuracy and computation efficiency for the unconsolidated sediments considered in our work. Phase shift shows extremely stable results also when a reduced number of traces is considered and other methods fail due to spatial aliasing or severe noise content that prevents from unambiguous interpretation (*Dal Moro, 1999*).
Most of the methods have been optimized for SASW or MASW data testing.

Method	Domain	Reference
Tranfer function technique	ω -x	Lai et al. (2002)
Amplitude regression versus offset	ω -k	Rix et al. (2000)
Half power bandwidth	ω -k	Badsar et al. (2010)
Multichannel multimode complex wavenumber estimation	ω -k	Misbah and Strobbia (2014)
Spatial decay of the Arias intensit	r-x	Badsar et al. (2011)
Circle fit method	ω-k	Ewins (1984)
Spatial decay of surface waves	ω-x	Kudo and Shima (1970), Park et al. (1998)

Table 3-2: Review methods to estimate seismic attenuation through borehole surveys

3.2.3 **Phase shift method**

According to Park et al. (*1998*) work, the phase shift method consists in a wavefield transformation that provides images of phase-velocity dispersion curves directly from the recorded wavefields of a multichannel shot gather. With this method, different modes are separated with higher resolution even if the shot gather consists of a relatively small number of traces collected over a limited offset range. It is a three-step transformation method:

- Fourier transform and amplitude normalization;
- dispersion imaging;
- extracting of dispersion curves.

In the transformation theory we consider an offset-time ($x - t$) domain representation $u(x,t)$ of a shot gather as in figure (**Figure 3.4**), so that the Fourier transformation can be applied to the time axis of $u(x,t)$ to obtain $U(x,\omega)$:

$$U(x,\omega) = \int u(x,t)e^{i\omega t}dt \qquad (3\text{-}12)$$

Where the transformed signal $U(x,\omega)$ can be expressed as the product of two terms:

$$U(x,\omega) = P(x,\omega)A(x,\omega) \qquad (3\text{-}13)$$

$P(x,\omega)$ and $A(x,\omega)$ are the phase and amplitude spectrum of the input signal. In $U(x,\omega)$, each frequency component is completely separated from other frequencies and the arrival time information is preserved in the phase spectrum $P(x,\omega)$. The phase spectrum contains all information about dispersion properties, while the amplitude spectrum contains information about all other properties such as attenuation and spherical divergence (*Park et al. 1998, Park, 2011*).

The Fourier transform of the signal $U(x,\omega)$ can be expressed in terms of amplitude and phase as follows:

$$U(x,\omega) = A(x,\omega)e^{-i\Phi x} \qquad (3\text{-}14)$$

Where $\Phi = \omega/c_\omega$, ω = frequency in Hz, c_ω = phase velocity for circular frequency ω. Therefore, the phase term is determined by the characteristic phase velocity of each frequency component and the offset. Appling the following integral transformation to $U(x,\omega)$ we obtain $V(\omega,\varphi)$:

$$V(\omega,\varphi) = \int e^{-i\varphi x}[U(x,\omega)/|U(x,\omega)|]dx = \int e^{-i(\Phi-\varphi)x}[A(x,\omega)/|A(x,\omega)|]dx \qquad (3\text{-}15)$$

The integral transformation can be thought of as the summing over offset of wavefields for a single frequency, after applying offset-dependent phase shift determined for an assumed phase velocity $c_\omega = \omega/\varphi$, as per eq. (1-3). For a value of φ where a peak in $\omega V(\omega,\varphi)$occours, the phase velocity $c_\omega$can be determined. If higher modes get appreciable amount of energy, there will be more than one peak. $U(x,\omega)$ is normalized with respect to offset, thus compensating for the effects of attenuation and spherical divergence. Therefore, for a given frequency ω, $V(\omega,\varphi)$ will have a maximum if

$$\varphi = \Phi = \omega/c_\omega \qquad (3\text{-}16)$$

Because $A(x,\omega)$ is both real and positive. For a value of $\varphi$where a peak of $V(\omega,\varphi)$ occurs, the phase velocity c_ω can be determined. If higher modes get appreciable amount of energy, there will be more than one peaks.

Dispersion curves result from the transformation of $V(\omega,\varphi)$to obtain $I(\omega,c_\omega)$ through changing the variables such that $c_\omega = \omega/\varphi$. In the $I(\omega,c_\omega)$ wavefields, there will be peaks along the c_ω-axis that satisfy (1-5) for a givenω. The focus along these peaks over different values ofωpermits the images of dispersion curves to be constructed.

So, the steps needed to obtain dispersion curves are summarized in the workflow below:

Fourier Transform and normalization

A **Fast Fourier Transformation (FFT)** is applied to each trace $u(x,t)$ of the shotgather (N-channels) in order to obtain frequency-domain representation $U(x,\omega)$ (equation 1-1);

↓

The amplitude of the Fourier transformed record is **normalized** in both the offset and the frequency dimensions. As the phase spectrum of the signal $P(x,\omega)$ contains all information about its dispersion properties, no significant information is lost.

↓

Iteration and summed amplitude

A **phase velocity range** for testing v_vals is established with a selected range of increments.

↓

For a given testing phase velocity (v_vals) and a given frequency ω, the **amount of phase shifts** required to counterbalance the time delay corresponding to specific offsets is determined.

↓

The phase shifts (determined in step 4 for a given testing phase velocity) are applied to distinct traces of the transformed surface wave record that are there after added to obtain the **slant-stacked (summed) amplitude** corresponding to each set of ω and v_values.

↓

Steps 4 and 5 are repeated for all the different frequency components of the transformed record in a scanning manner, changing v_values by small increments within the previously specified range (step 3).

↓

Dispersion imaging and picking

The **phase velocity spectrum** (dispersion image) is obtained by plotting the summed amplitude in the frequency–phase velocity domain, either in two or three dimensions. The peak values (high-amplitude bands) observed display the dispersion characteristics of the recorded surface waves.

3.2.3.1 Example of phase shift method processing in PYTHON code with real data

The user must previously input a series of parameters like the length of recorded trace to use in calculations (sec), receivers spacing and position, sample rate, number of samples, frequency sampling, a range of frequency and velocity to consider in calculation, etc.

Here an example of data parameters used in this test (where the shot gather is made up of 24 channels and the employed source is a 6.5 kg sledge hammer):

```
1. dt = 3.125e-05                    # sample rate [s]
2. n_channels = 24       # number of receivers used in testing
3. n_samples = 2048         # number of samples per receiver
4. position = range(0,48,2)          # vector of positions for all receivers
5. offset = 4              # offset location
6. timeHistories = TH  # matrix containing time histories for all receivers
7. fnyq = 1.0/(2 * dt)        # Nyquist frequency
8. df = 1.0 / (n_samples *  dt)         # Sampling in frequency domain
9. kres = 2 * np.pi / min(np.diff(position)) # Maximum resolvable wavenumber
```

```
1. f_values = np.linspace(5,200,1000)
2. v_values = np.linspace(10,600,1000)
```

Once we fixed these parameters, we can calculate the Fast Fourier Transform of each trace, (Equation 1 of *Park et al. 1998,* **figure 3.7**) and applying equation 4 of Park et al. (*1998*) on a double loop through frequencies and velocities range in order to obtain dispersion curves in velocity-frequency domain. In **figure 3.7** we can observe the various vibration modes relates with dispersion curves in which the lower curve represents the fundamental mode of propagation.

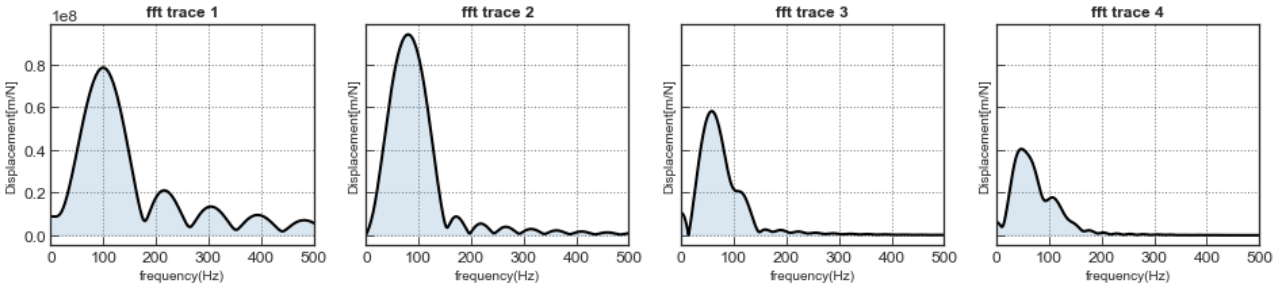

Figure 3.6: Fast fourier transform of 4 traces in the 24-channel record

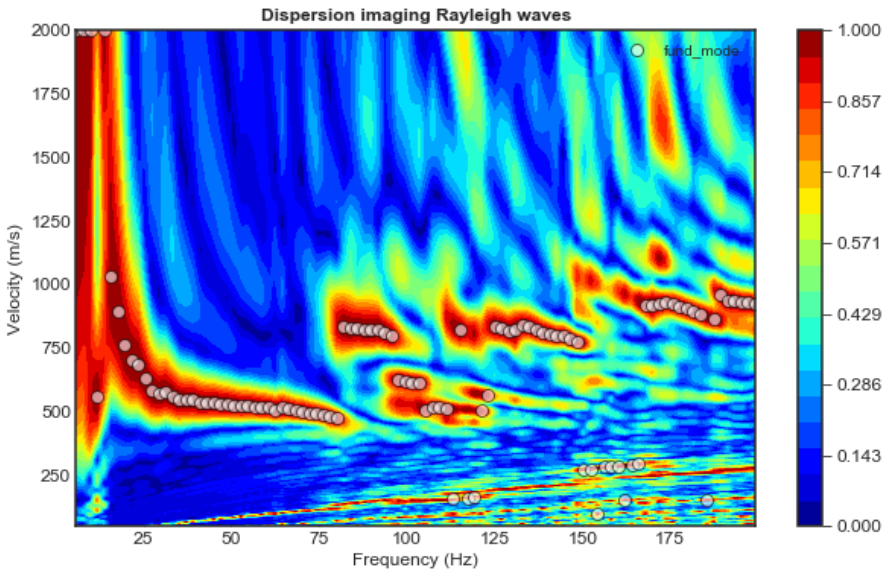

Figure 3.7: Experimental dispersion curves obtained by using phase shift method (2-meters offset).

The methods used to estimate attenuation curves are described below.

3.2.4 **Spatial decay measurement of surface waves**

This method is based ona spectral analysis of the traces described in Kudo and Shima work (1970) and revisited by Xia et al. (2002). The experimental attenuation curves have been calculated through a spectral analysis technique based on MASW testing data.We can express a Rayleigh wave amplitude as:

$$A(x+dx) = A(x)e^{-\alpha dx} \qquad (3\text{-}17)$$

where A is Rayleigh wave amplitude, $\alpha$is a Rayleigh wave attenuation coefficient, and x and dx are the nearest source-geophone offset and a geophone interval, respectively. The attenuation coefficient $\alpha_R(\omega)$ is given as follow:

$$\alpha_R(\omega) = -\frac{\ln\left[\left|\frac{W(x+dx,\omega)}{W(x,\omega)}\right|\sqrt{\frac{x+dx}{x}}\right]}{dx} \qquad (3\text{-}18)$$

where $\alpha_R(\omega)$ is the Rayleigh wave attenuation coefficient as a function of frequency f, $W$is the amplitude of a specific frequency, and the term under square root is a scaling factor in calculating the attenuation coefficient. This method assumes that a single Rayleigh wave mode is dominant, and may lead to incorrect results if multiple modes are presents significantly in the wave field.

3.2.4.1 **Example of Spatial decay of surface waves in PYTHON code with real data**

Considering the same data and parameter settings of **Section 3.2.4.1**, we show an extract of the code that we used to extract attenuation curves from real surface waves

dataset. The code implements equation (1-24) to calculate the value of attenuation coefficients for every frequency in the spectrum and every pair of receivers. Considering a number of receivers N, the attenuation curves that we obtain are N-1. By taking the average of each N-1 attenuation curves we obtain the total attenuation curve as showed in **Figure 3.8**

```
10. gamma_values = pd.DataFrame(np.matrix(np.empty([len(stream)-
    1,len(stream.iloc[0])])))
11. for i in range (0,23):
12.     for n in range (1,24):
13.         gamma_values.iloc[i] = -(np.log(np.abs((stream.iloc[n]/
14.                             stream.iloc[i])*np.sqrt((steps[i]+2)/steps[i]))))/2)
```

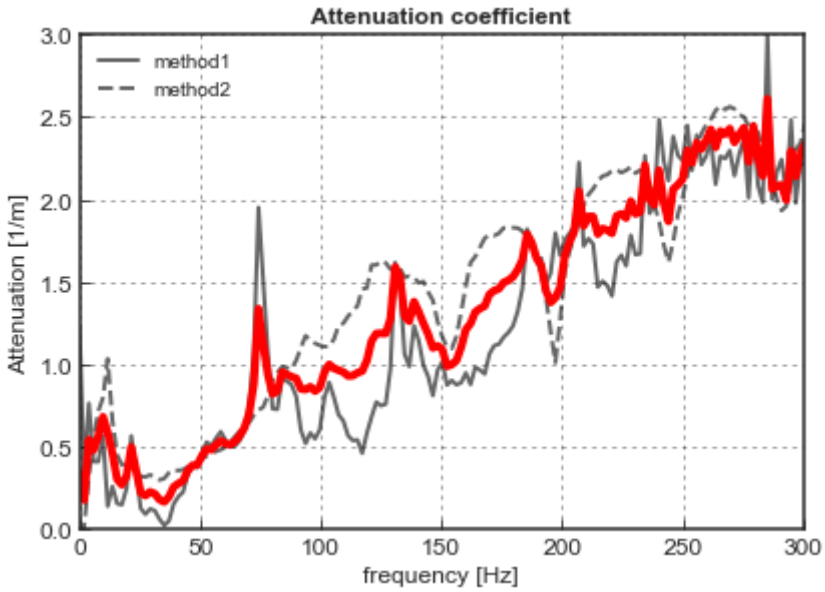

Figure 3.8: Total attenuation curve (in red), the two curves in grey is referred to two different pairs geometry.

3.3 Theoretical dispersion and attenuation curves by Direct Stiffness Matrix method

The solution of the forward problem for 1D layered models can be obtained very efficiently using a variety of algorithms such as **propagator matrix** (*Thomson 1950; Haskell 1953; Gilbert and Backus 1966*) or **stiffness matrix** (*Kausel and Roesset, 1981*) algorithms.
The direct stiffness or impedance matrix method is a tool for the analysis of wave propagation problems in elastic media, namely source problems, normal mode problems, and wave amplification problems. In principle, it is an analytical method in the sense that one obtains mathematical expressions for displacements that are free from approximations or discretization errors. However, the resulting expressions are generally intractable by

purely analytical means and must ultimately be evaluated numerically. The method can be applied to a large class of continua, such as beams and plates, but we restrict our presentation to the following three problems involving isotropic media formulated in Cartesian and cylindrical coordinates.

For the layered model, in our work six parameters are needed to fully characterize each layer: density ρ, thickness h, two elastic constants (e.g., shear modulus G and Poisson's ratio ν) and two damping ratios (i.e. shear-wave and body-wave damping ratio). Often, the elastic parameters are defined in terms of the P-wave and S-wave velocities and of Q_P and Q_S (Quality factor) for each layer. Based on sensitivity analyses (*Nazarian, 1984*), two of these parameters are typically fixed a priori for each layer, that is, the density and Poisson's ratio (or a given ratio between P-wave and S-wave velocities) of each layer.

The method is based on the use of integral transforms, and consists of the following steps (*Kausel and Roesset, 1981; Kausel, 2006*):

- Transform the source(s) (if any), which are modeled as external tractions, from the space–time domain into the frequency–wavenumber domain. This produces a source-vector p, usually in closed form. The loads p are related to the displacements u through the element stiffness matrix K:
- For each frequency and wavenumber, determine the stiffness matrix of halfspace and each layer (element stiffness matrices) and, by appropriate superposition, the stiffness matrix K of the complete layered system. This matrix is block-tridiagonal (i.e., narrowly banded) and symmetric, and in general its elements are complex. Damping is incorporated via complex moduli.
- Solve the system of equations $p = Ku$ by standard methods, and obtain the displacements in the frequency–wavenumber domain.
- Carry out an inverse transform into the spatial–temporal domain, which yields the desired response.

For the computation of halfspace and layer stiffness matrices, we will consider only the contribution of Rayleigh waves in the P-SV case.

3.3.1 **Halfspace stiffness matrix**

The 2x2-halfspace matrix for a lower ($z < 0$) half-space subjected to a P-SV wave's polarization is derived from Table 1 of Kausel and Roësset (*1981*) and expressed as:

$$k_{hlfpsv} = 2kG\left[\frac{1-s^2}{2(1-rs)}\begin{Bmatrix} r & 1 \\ 1 & s \end{Bmatrix} - \begin{Bmatrix} 0 & 1 \\ 1 & 0 \end{Bmatrix}\right] \qquad (3\text{-}19)$$

For an upper half-space (opening upward), simple reverse the sign of off-diagonal terms.

The stiffness matrix for a half-space subjected instead to a SH waves polarization is derived from Table 5 of Kausel and Roësset (*1981*) and expressed as:

$$k_{hlfsh} = ksG \qquad (3\text{-}20)$$

3.3.1.1 **Example of an halfspace matrix computed in PYTHON code**

The example shows the computation of the halfspace matrices for S-PV and SH polarization from a set of reference parameters.

Here we fix model parameters

```
1. vp = 2000  # P-wave velocity (m/s)
2. vs = 500  # S-wave velocity (m/s)
3. ds = 0.05  # S-wave Damping ratio
4. dp = 0.05  # P-wave Damping ratio
5. rho = 1800 # Density (kg/mc)
6. h = float('inf')  # Layer thickness (meters)
7. omega = 100  # Frequency (Hz)
8. k = 0.5  # horizontal wavenumber (rad/m)
9. G = rho*(vs**2)/1e08 # Shear modulus (Mpa)
```

The functions **k_hlfpsv** and **k_hlfsh** return the relative halfspace matrices for both problems, in according to Table1 and Table5 of Kausel and Roësset (*1981*) article. Here we fit our simple matrix with parameters in according with example 4.1 in EDT-manual (*Schevenels M., 2007*):

```
1. k_hlfpsv(vp,vs,omega,k,True)
2. matrix([[ 4.06684092+0.0176422j ,  0.41266369-0.01566676j],
3.         [ 0.41266369-0.01566676j,  3.74613873+0.05003505j]])
```

3.3.2 **Element stiffness matrix**

$$k_{11,j} = \frac{1-s^2}{2D}\begin{Bmatrix} \frac{1}{s}(C^pS^s - psC^sS^p) & -(1-C^pC^s+psS^pS^s) \\ -(1-C^pC^s+psS^pS^s) & \frac{1}{p}(C^sS^p - psC^pS^s) \end{Bmatrix} - \frac{1+s^2}{2}\begin{Bmatrix} 0 & 1 \\ 1 & 0 \end{Bmatrix} \quad (3\text{-}21)$$

$$k_{12,j} = \frac{1-s^2}{2D}\begin{Bmatrix} \frac{1}{s}(psS^p - S^s) & -(C^p - C^s) \\ (C^p - C^s) & \frac{1}{p}(psS^s - S^p) \end{Bmatrix} \quad (3\text{-}22)$$

$$k_{22,j} = same\ as\ k_{11,j}, with\ off - diagonal\ signs\ changed$$

$$k_{21,j} = k_{12,j}^{T}$$

Where $k_{11,j}, k_{12,j}, k_{22,j}$ and $k_{21,j}$ are the 2 x 2 submatrices of the element stiffness matrix for the jth layer.

$$k_{elmpsv,j} = \begin{bmatrix} k_{11,j} & k_{12,j} \\ k_{21,j} & k_{22,j} \end{bmatrix} \qquad j = 1, \dots, n \tag{3-23}$$

For the SH-waves polarization, the element stiffness matrix is assembled and expressed as:

$$k_{elmsh,j} = \frac{ksG}{sinh(ksh)} \begin{bmatrix} cosh(ksh) & -1 \\ -1 & cosh(ksh) \end{bmatrix} \tag{3-24}$$

3.3.3 **Assembly global stiffness matrix**

The global stiffness matrix (or system stiffness matrix) K is assembled from the elements and halfspace stiffness matrices at the common layer interfaces and has a tridiagonal structure, and is symmetric. For each P-SV and SH wave polarization, the global or system stiffness matrix can be computed as:

$$K_{glob} = \begin{bmatrix} k_{11,1} & k_{12,1} & \cdots & & & \\ k_{21,1} & k_{22,1} + k_{11,2} & k_{12,2} & \ddots & & \\ \vdots & k_{21,2} & k_{22,2} + k_{11,3} & \ddots & \ddots & \\ & & \ddots & \ddots & \ddots & \\ & & & \ddots & k_{22,n-1} + k_{11,n} & k_{12,2} \\ & & & \cdots & k_{21,n} & k_{22,n} + k_{hlf} \end{bmatrix} \tag{3-25}$$

3.3.3.1 **Example of a global matrix computed in PYTHON code**

```
1. vp = [360, 1000, 1400, 1400]  # P-wave velocity (m/s)
2. vs = [180, 120, 180, 360]  # S-wave velocity (m/s)
3. ds = 0.03  # S-wave Damping ratio, i.e. Q = 16,67 (adim)
4. dp = 0.03 # P-wave Damping ratio, i.e. Q = 16,67 (adim)
5. rho = 1800 # Density (kg/mc)
6. h = [2, 4, 8, float('inf')]  # Layer thickness (meters)
7. G = (rho*(np.power(vs,2)))/1e08 # Shear modulus (Mpa)
```

The function k**_globpsv_matrix** calculates the global matrix automatically according to the number of layers present above the half-space. In this example I've fixed frequency and wavenumber only at 100 and 0.5, respectively, to extract only one stiffness matrix.

```
8.  k_globpsv_matrix(h,vp,vs,rho,0.5,100,True)
9.
10. matrix([[ 0.42448779+0.00794457j, -0.11908087-0.03139854j,
11.          -0.32789814+0.00767228j,  0.30651216+0.03147965j,
12.           0.00000000+0.j        ,  0.00000000+0.j        ],
13.         [-0.11908087-0.03139854j,  1.57088127+0.12659538j,
14.          -0.30651216-0.03147965j, -1.62469457-0.12657122j,
15.           0.00000000+0.j        ,  0.00000000+0.j        ],
16.         [-0.32789814+0.00767228j, -0.30651216-0.03147965j,
17.           0.83402185+0.02546558j, -0.20777924-0.06584859j,
18.          -0.13348331+0.01669636j,  0.35062644+0.03466819j],
19.         [ 0.30651216+0.03147965j, -1.62469457-0.12657122j,
20.          -0.20777924-0.06584859j,  2.49515051+0.19643279j,
21.          -0.35062644-0.03466819j, -0.98936788-0.06977971j],
22.         [ 0.00000000+0.j        ,  0.00000000+0.j        ,
23.          -0.13348331+0.01669636j, -0.35062644-0.03466819j,
24.           0.63707946+0.15728793j,  0.13175790-0.20077895j],
25.         [ 0.00000000+0.j        ,  0.00000000+0.j        ,
26.           0.35062644+0.03466819j, -0.98936788-0.06977971j,
27.           0.13175790-0.20077895j,  0.80268777+0.28004669j]])
```

3.3.4 **Trascendental eigenvalue problem**

Surface waves dispersion curves in a layered medium can be computed by means of the direct stiffness method or the thin layer method (**Section 3.3.4.2**) by the solution of an eigenvalue problem in terms of the frequency ω and the horizontal wavenumber k_x. This work focuses on the calculation of dispersive waves in a layered halfspace by means of the direct stiffness method. If the direct stiffness method is used, the eigenvalue problem is transcendental, has an infinite number of solutions, and must be solved with search techniques. If the thin layer method is used, a quadratic eigenvalue problem in terms of the horizontal wavenumber k_x is obtained for each frequency ω. This problem can be reformulated as a linear eigenvalue problem, which can be solved using standard techniques.

In the direct stiffness method, the equilibrium of the medium in the frequency-wavenumber domain can be expressed as:

$$p = Ku \qquad (3\text{-}26)$$

Where p is the system external load vector, and u is the system displacement vector, respectively. Considering a horizontally layered halfspace, if the load vector p vanished, in

a system with no external loading or tractions, the dynamic equilibrium equation can be written as:

$$Ku = 0 \qquad (3\text{-}27)$$

In this case, if the global stiffness matrix is singular, non-trivial solutions for the displacement u can be obtained if the determinant of the global stiffness matrix vanish (equal to zero), and the displacements are equal to the in-plane free surface waves or natural modes of vibration in the layered halfspace. Hence, wave numbers that represent the modal solutions at different frequencies are obtained as the solutions of:

$$F_R(k, \omega) = det(K) = 0 \qquad (3\text{-}28)$$

where $F_R(c, k)$ represents the Rayleigh secular equation that can depends on various parameters:

$$F_R(k, \omega, V_S, V_P, Q_S, Q_P, \rho, h) = 0 \qquad (3\text{-}29)$$

where k is the wavenumber, ω is the angular frequency, V_S, V_P are the S and P wave velocities, Q_S, Q_P are the S and P quality factor, respectively,ρ is the mass density, and h is the depth of the layer. Knowing the connections between k, ω, λ and c we can describe the solutions in the desired domain ((k, ω), (k, c),(ω, λ), etc.).

This equation can be expressed considering various layers and points on which calculate the solutions:

$$F_{R,q}\left(k_q, \omega_q, \bar{V}_S, \bar{V}_P, \bar{Q}_S, \bar{Q}_P, \bar{\rho}, \bar{h}\right) = 0 \qquad (3\text{-}30)$$

where $q = 1, \dots, Q$ is the number of points where the theoretical dispersion curve is computed, and the overlined terms is referring to vectors.

Due to the uncoupling of the polarization of waves in plane (PSV) and out-of-plane (SH) problems (that govern Rayleigh and Love waves); the equation 1-34 can be reformulated as:

$$det(K_{PSV}) = 0 \qquad (3\text{-}31)$$
$$det(K_{SH}) = 0$$

The matrices utilized for P-SV problem are described previously. The equations corresponds to an eigenvalue problem in terms of the angular frequency ω and the complex horizontal wavenumber k. The eigenvalue problem includes transcendental functions (i.e. is transcendental problem), infinite numbers of accepted solutions or modes are theoretically possible, and must be solved only numerically, by search algorithms that minimizes the determinant in terms of the complex wavenumber k, as an explicit solution of the problem is not available, except for a simple layered media, constituting by one or two layers.

For each frequency and wavenumber, the phase velocity c of the Rayleigh wave is obtained theoretically as the ratio $\omega/Re(k)$, where (ω, k) is a solution that satisfy equation 1-37 (roots). In **Figure 5.1,** we can observe the trend of global stiffness matrix determinant varying phase velocities at only four different frequencies, in the (c, ω) domain.

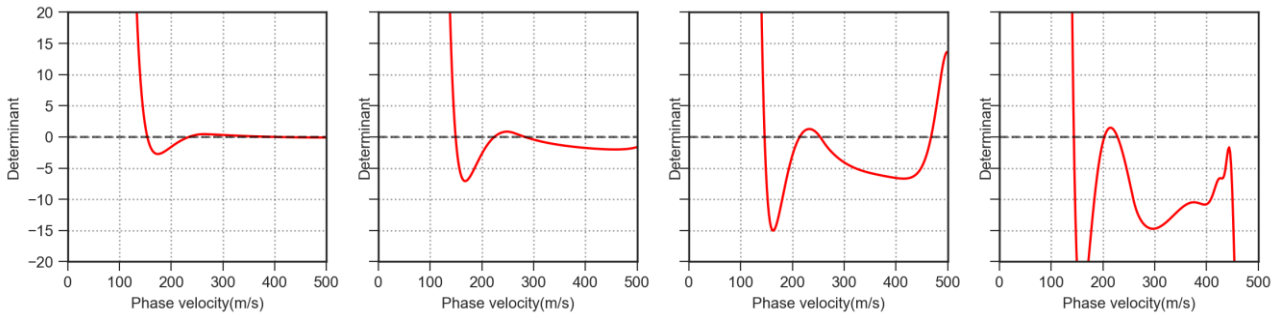

Figure 3.8: trend of determinant varying phase velocity at four different frequencies (39,47,54,62 Hz), the dot line represent zero value of determinant.

The attenuation coefficient $\gamma_R(\omega)$ of the Rayleigh wave is computed as $1/Im(k)$. We can notice in **Figure 3.8** that at a given frequency or wavenumber, multiple solutions may exist corresponding to a multiple modes of Rayleigh waves. For each frequency, the solution with the lowest value of phase velocity is referred to as the fundamental Rayleigh wave mode of vibration, the second value is the first mode, and so on.

3.3.4.1 Example of dispersion curves computed in PYTHON code

Here an example of the code used for the calculation of theoretical dispersion curves, the code was tested on three different soil layer structures, with more complex layering, used previously by Tokimatsu et al. (1992) and Tokimatsu (1997). The curves were computed on 0-30 Hz frequency range using a testing phase velocity increment of 0.5 m/s, that is well enough for this test, although authors recommend small increments (*Olafsdottir, 2018*). In all three cases, the agreement between the fundamental and higher modes was good in the frequency range considered. In the right column has been reported the same operation on f-k domain.

	Shear wave velocity (m/s)			**Compressional wave velocity (m/s)**		
Layer number	Case 1	Case 2	Case 3		Mass density (kg/m³)	Layer thickness (m)
1	80	180	80	360	1800	2.0
2	120	120	180	1000	1800	4.0
3	180	180	120	1000	1800	8.0
4 (halfspace)	360	360	360	1400	1800	infinite

Table 3-3: Test profiles, cases 1, 2, and 3 (Tokimatsu et al. 1992 and Tokimatsu 1997).

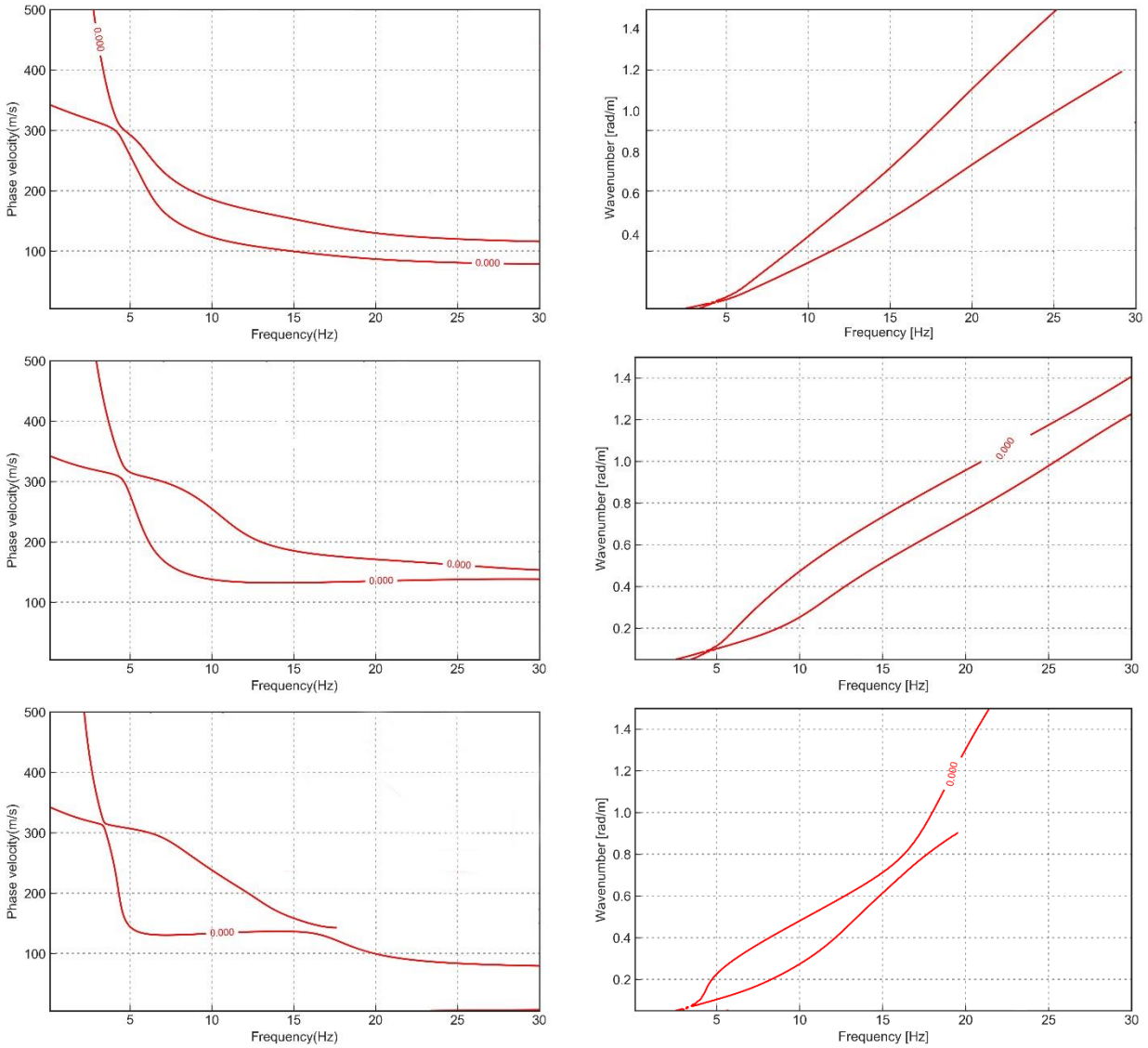

Figure 3.9: Comparison of theoretical fundamental and first higher-modes dispersion curves obtained by python code and presented by Tokimatsu et al. (1992) and Tokimatsu (1997): in the left column a), the multi-mode dispersion curves in frequency and phase velocity domain, in the right column b), the dispersion curves in the frequency and wavenumber domain. For the test only the fundamental and first higher mode were computed.

3.3.4.2 Exploring thin layer method

In this work, I've investigated the potentiality of the *Thin-Layer Method* (TLM) (*Kausel, 1994*), that is proposed as an effective tool for the analysis and simulation of wave motion in layered soils and other laminated media. In essence, the method consists in a partial discretization of the wave equation, namely one in the direction of layering.

The thin layer method is an alternative to the direct stiffness method for wave propagation in layered media. It is based on the use of polynomial shape functions to represent the vertical variation of displacements and tractions. Compared to the direct stiffness method, the thin layer method leads to mathematically more tractable stiffness

matrices involving only polynomial functions instead of transcendental functions. Due to its approximate nature, the thin layer method requires a small thickness of the layer elements compared to the smallest relevant wavelength. Furthermore, the method is only applicable to media with a finite thickness, with either free-free boundary conditions or supported by a rigid stratum (*Rix, 2005*).

While the direct stiffness method allows for the use of layer and halfspace elements, the thin layer method only provides a layer element. Due to the use of linear shape functions for the displacements, the element stiffness matrix Konly involves polynomial functions of the horizontal wavenumber $k_x$andthe circular frequency ω. Waas (1970) suggested treating the layered region as a continuum in the horizontal direction but to discretize in the vertical direction, resulting in the following equation.

In the thin layer method, the element stiffness matrix Kcan bedecomposed as:

$$K = Ak^2 + Bk + G - \omega^2 M = Ak^2 + Bk + C \qquad (3\text{-}32)$$

where the matricesA, B, G and $M$are independent of the wavenumber $k_x$and the frequency ω, but depends solely on the material properties of the layer. Numerical expressions for the matrices A, B, G and M of the layer element can be found in Kausel and Roesset (*1981*), Kausel (*1994*).

This results in a quadratic eigenvalue problem , where k are the wavenumbers for thelayered region. The solution to **Equation 3-32** consists of $4n$ eigenvalues for Love and Rayleigh waves.Each eigenvalue results in two roots: a set of $2n$ values with negative imaginary parts (K) and $2n$ values with positive imaginary parts (k) where it can be shown $k = -k$.

Kausel and Roesset (*1981*) extended the thin layer method to allow elements of finite length, labeled hyper-elements, using the same semi-analytical formulation.

The matrices A, B and C have been calculated using the implemented abc_solve PYTHON function. **Figure 3.10** plot the three matrices in the sparsity pattern of a 2D array for a frequency of 100 Hz. In blue are visualized only the non-zero values of the array.

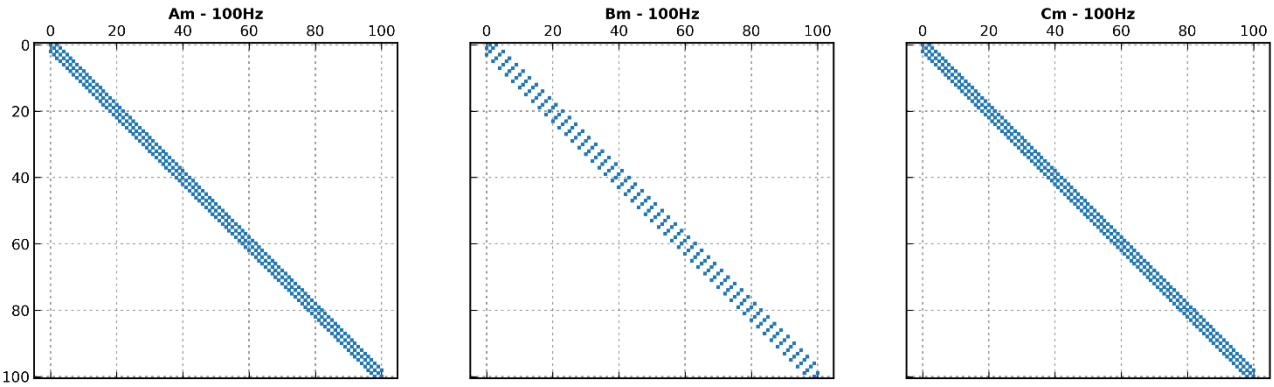

Figure 3.109: examples of sparsity patterns of the matrices Am, Bm and Cm for a 100 Hz frequency

To account for material damping, even in the Thin layer method, the elastic moduli λ, μ should be replaced by their complex counterparts;

$$\lambda = \lambda(1 + 2i\xi sign(\omega)) \qquad (3\text{-}33)$$
$$\mu = \mu(1 + 2i\xi sign(\omega))$$

Where ξ is the damping ratio of the layer.

Overlapping the thin-layer matrices, we obtain the system matrices explained beforeA, B, G, M,which will beblock-tridiagonal matrices. In general, they will be stored by interface, each of which has two degrees of freedom.

The quadratic eigenvalue problem introduced for generalized Rayleigh waves and satisfied the following properties (*Kausel, 1994*):

- If $k;$ is a solution, then so is also $-k;$. These two solutions have **adjoined** eigenvectors whose polarization is apposite (i.e. the signs of the vertical components are reversed). They correspond to waves traveling and/or vanishing in opposite directions. Also, in the undamped case, the eigenvalues and eigenvectors occur in complex conjugate pairs.
- If $k$is **real**, then the eigenvector is also real. $k > 0$ corresponds to waves with positivephase velocity.
- If $k$is **purely imaginary**, the mode does not propagate, but vanishes to the right or left depending on the sign of $k;$
- If $k;$ is **complex**, the eigenvectors are complex, the motions are not in phase, and the wave is evanescent. The Rayleigh mode propagates to either the right or left (i.e. in$\pm x$) depending on the sign of $Re(k);$. Also, it decays (or vanishes) to the right or left depending on the sign of $Im(k);$. Observe that the wave may propagate and decay indifferent directions!

The most robust algorithm has proven to be inverse iteration with shift by Rayleigh quotient. As the wavenumber k entered the equations nonlinearly the Linear Companion Matrix Method was introduced to rearrange the problem into a generalized eigenvalue problem. The corresponding transformation for the **equation 3-33** is to find an equivalent linear $\lambda - matrix, A - \lambda B$. We say that a $2n \times 2n$ linear $\lambda - matrix, A - \lambda B$ is a linearization. Numerical computation of the solution of a quadratic eigenvalue problem can be found in Tisseur (2013). We tested this method reformulation the matrices A, B, C obtaining a linear matrix. Since the problem is not anymore quadratic, can be solve with the standard python functions to solve a generalized eigenvalue problem like scipy.linalg.eig. The problem is the great numerical approximation using python standard function, that will be solved increasing the number of thin layer, but increasing number of layers increases the time computation. More layers mean bigger matrices and more solutions in the eigenvalue problem. In Figure 5.5 are plotted the real and imaginary part of the k −solutions. Here an example of the code used to solve the quadratic problem:

```
28. # solves quadratic eigenvalue problem by reducing
```

```
29. # the problem to a generalized eigenvalue problem A*x = lambdanew*B*x
30. dim = np.shape(K)[0]
31. Arow1 = np.hstack((-C,-K))
32. Arow2 = np.hstack((np.eye(dim),np.zeros((dim,dim))))
33. A = np.vstack((Arow1,Arow2))
34. Brow1 = np.hstack((M,np.zeros((dim,dim))))
35. Brow2 = np.hstack((np.zeros((dim,dim)),np.eye(dim)))
36. B = np.vstack((Brow1,Brow2))
37. eigvals, eigvecs = scipy.linalg.eig(A, B)
38. eigvecsnew = normalizeVecAll(eigvecs[:dim,:],0) # convert gen. eig. solution back to qu
    ad. eig. problem
39. return eigvals, eigvecsnew
```

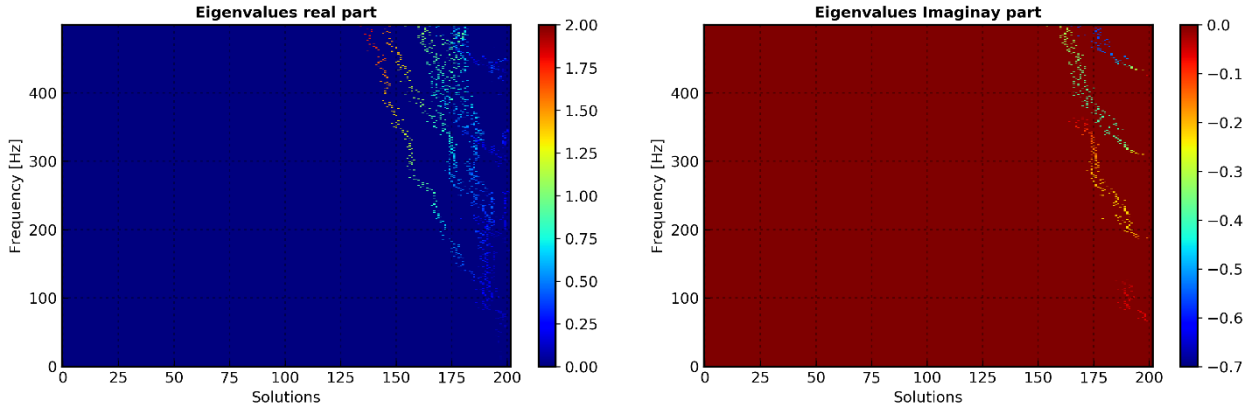

Figure 3.11: Eigenvalues solution from the generalized eigenvalues problem. In a) the real part of the k solutions varying frequency corresponding to dispersion curves; in b) the imaginary part corresponding to attenuation coefficients.

Chapter 4.
In situ measurements of seismic attenuation and surface waves comparison

This chapter describes the equipment and procedures employed for seismic attenuation estimates using seismic downhole surveys and MASW testing. The aim of this study is to provide an optimized processing procedure for obtaining accurate seismic attenuation profiles using near-surface borehole surveys and then optimize a surface waves testing.

The procedures for downhole measurements adopted take inspiration from the processing techniques adopted in VSP for hydrocarbon exploration, which is optimized for near-surface downhole testing.

In addition, a surface waves test has been produced to extract dispersion and attenuation curves from experimental dataset. These curves are then compared with dispersion and attenuation curves predicted by theoretical computation, using velocity and damping parameters coming from DHT surveys to assess the accuracy of surface-wave estimation as far as Q and damping data are concerned.

4.1 Site locations

The data set for determining Q are measured at a test site located in Rieti (RI), Central Italy. From 2nd to 8th August 2017, as part of the investigation and study activities related to the level III Seismic Microzonation (MS) of the Municipality of Rieti (RI), in Campomoro (Borgo S. Antonio), a continuous core drilling was carried out, up to 44 meters, and equipped for the downhole geophysical test. The near-surface VSP is located on the left bank of the Velino River, in the Rieti Valley. The borehole drilling data are reported in tab. 4.1.

Survey		
Geognostic survey	Latitude	42°,402415
	Longitude	12°,866859

	Material	PVC pipe with a 3" diameter and 0.5 cm thickness;
	Cementation	consisting of water, cement and bentonite

Table 4-1: Parameters for field data site location and drilling description

a)

b)

c)

Figure 4.1: Map of borehole site location; a) large scale location; b) location of test site 1, in Rieti (Campomoro); c) location of test site 2, in INGV headquarter

The urban area of Rieti, including the historic center, falls at the south-eastern edge of the "Conca Reatina", an alluvial plan of the Velino River. The city of Rieti is mainly founded on a lithoid travertine plate, partially covered by anthropic deposits, except for the southern part which is based on alluvial sediments. These deposits, which fill an E-W valley with very steep sides, and about 300 meters wide, refer to the Velino River and are very recent, attributable to the Holocene. The second test site, is located to the headquarters of INGV in Rome, at Via di Vigna Murata 605. Almost the entire territory of the Municipio Roma IX is made up of the main ignimbritic units erupted by the Colli Albani volcano (units of Trigoria, Pozzolane Rosse, Pozzolane Nere, formation of Villa Senni), which are interspersed with synthesized lavic expansions.

Fig.4.2 and 4.3 shows the seismic velocity results, coming from downhole test, of the two sites of interest.

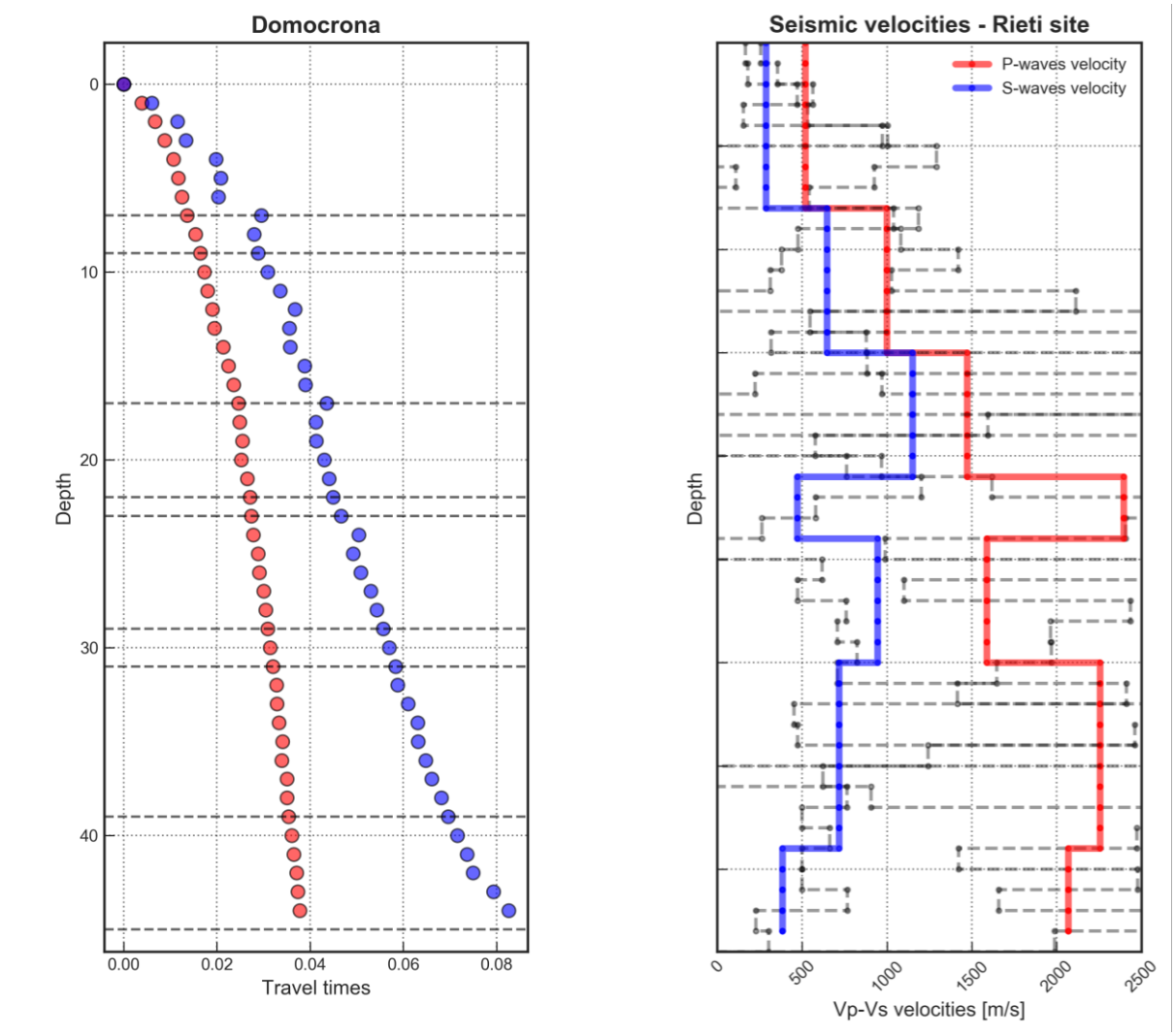

a) b)

Figure 4.2: Test site 1; Path of the seismic rays (Ray-tracing). b) Velocity trend with depth.

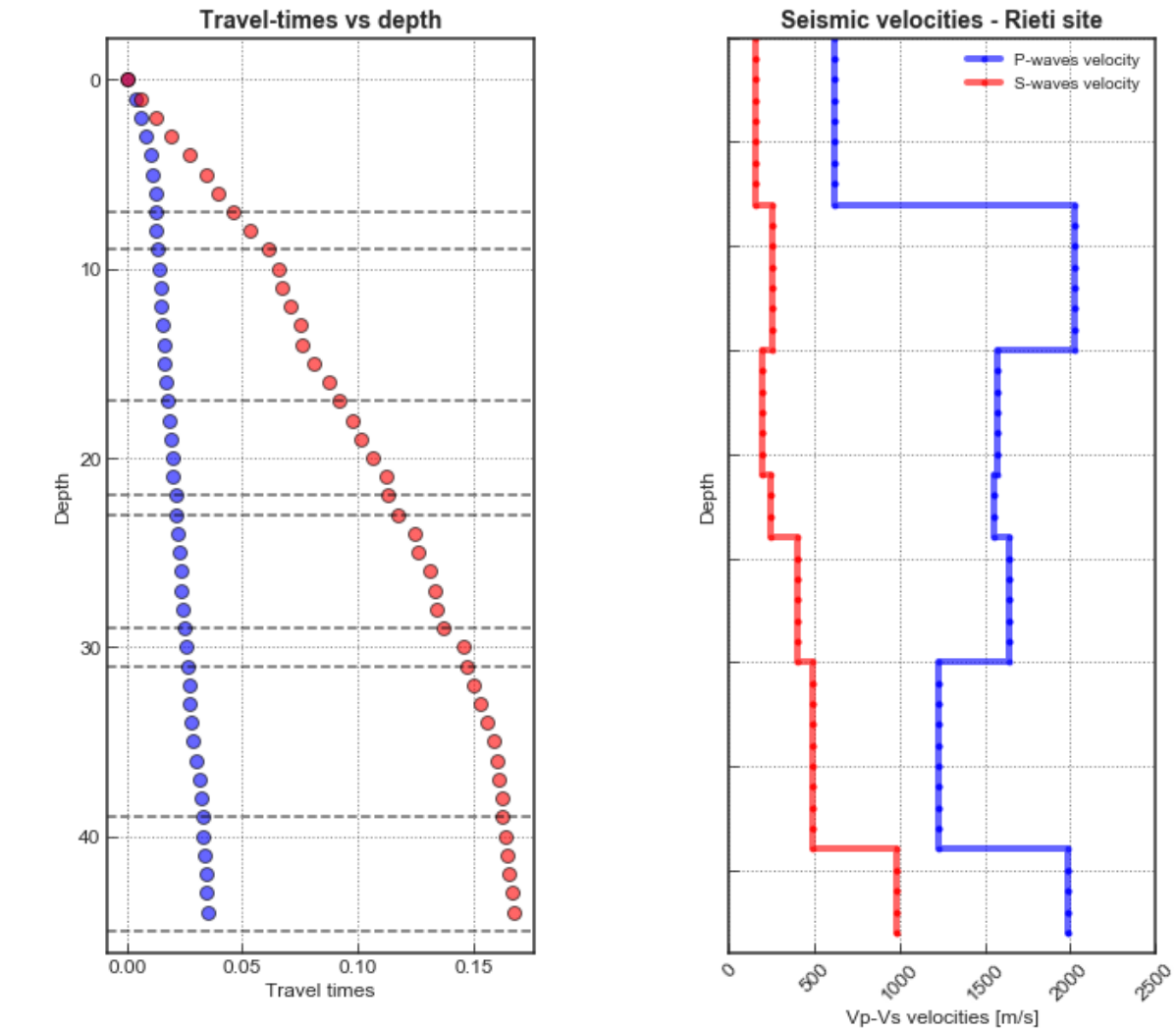

a) b)

Figure 4.3: Test site 2; a) Path of the seismic rays (Ray-tracing). b) Velocity trend with depth.

The velocity trend is consistent with the stratigraphic variations. A good correspondence between lithotypes and velocity variations is observed along the two boreholes. For the Rieti site, the gravels at the base of the survey exhibits S-wave velocity close to 800 m/s, even if the downward continuity of these formations remains to be assessed, given that the borehole description indicates an increase in the silty-sandy matrix in the gravels finds below 45 m of depth.

4.2 Instrumentation and geometry

This section describes the instruments, the acquisition parameters and survey design utilized for seismic borehole attenuation measurements. The two methods utilized are heavily affected by the accuracy of the recorded waveform, especially at the near-surface scale.

4.2.1 **Instruments utilized**

4.2.1.1 **Seismic sources**

Vertically operated shakers or vertical impact sources are typically used for surface and borehole wave testing. Especially downhole recordings, whether from well velocity surveys, vertical seismic profiles or customized experiments, provide the data set most commonly used in measurements of attenuation (*Raikes and White, 1988*).

Weight-drop systems, vertically accelerated masses and even vibroseis are able to generate high S/N ratios, provide control over the frequency content and allow longer wavelengths to be gathered resulting in larger investigation depths. Nevertheless, these sources are expensive and not easily manageable.

The cheapest and most common seismic source that we have used consists of a 6 kg sledge-hammer striking manually on an Aluminum plate coupled to the ground (The weight of the sledgehammer should be at least 5 kg, *Foti, 2018*).

Two seismic sources have been used for P- and S-wave measurements. For P-wave testing, the source consists in an Aluminum plate of 30 cm diameter which is striked through vertically. For the S-eave generation, an Aluminum source built by DICEA's Geophysics Area has been employed. The two different seismic source are showed in **figure 4.4**:

a) **b)**

c) **d)**

Figure 4.4: Pictures of the Test site 1: a) Generation of P waves by vertically vibration shot on metal plate. b) Impact source for SH wave generation. c) and d) positioning of both the sources.

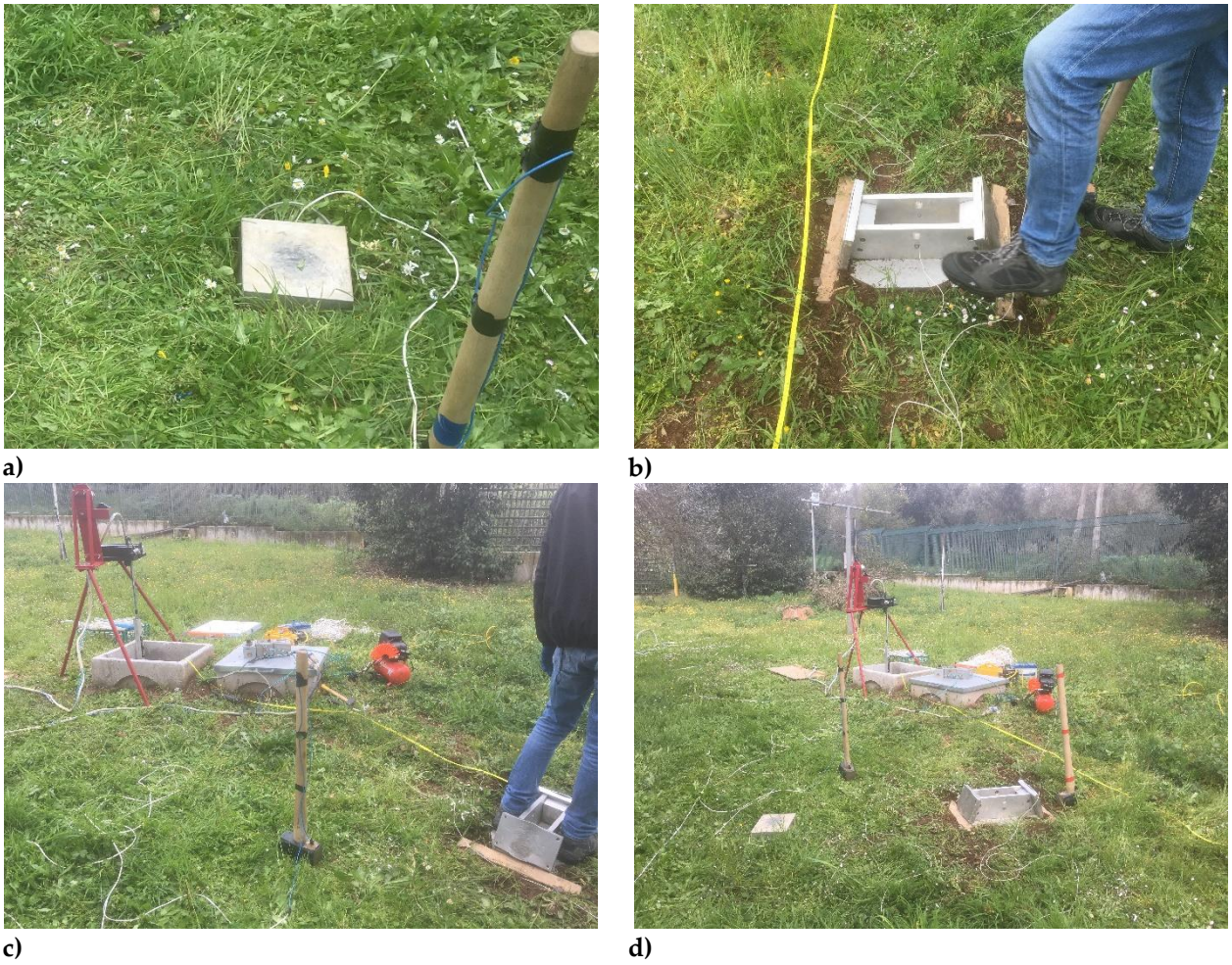

a) **b)**

c) **d)**

Figure 4.5: Pictures of the Test site 2: a) Generation of P waves by vertically vibration shot on metal plate. b) Impact source for SH wave generation. c) and d) positioning of both the sources.

4.2.1.2 **Receivers**

For the attenuation analysis, a geophone downhole string was used in both the test sites to perform a DHT testing. It consists of n°8 three-channel geophones with a 10 Hz natural frequency, spaced 1 meter apart and progressively lowered down 5 meters for each measure, resulting in an overlap of three traces between two subsequent acquisitions (in **figure 4.6b** is showed the insertion of the string in the borehole). For a classic VSP surveys, the depth spacing of the records is generally too large to allow a good resolution for near-surface estimates (50-100 meter depths, 1-2-meter receiver spacing).

The seismic string was provided by the Politecnico di Torino (DIATI) (**Figure 4.6a**). The connection with the PVC pipe is guaranteed by a system of pistons operated manually with a compressor via remote control (**Figure 4.6c and 4.6d**).

The geophone string is suspended on a tripod in order to keep the equipment locked in a vertical position (**Figure 4.8a and 4.8b**)

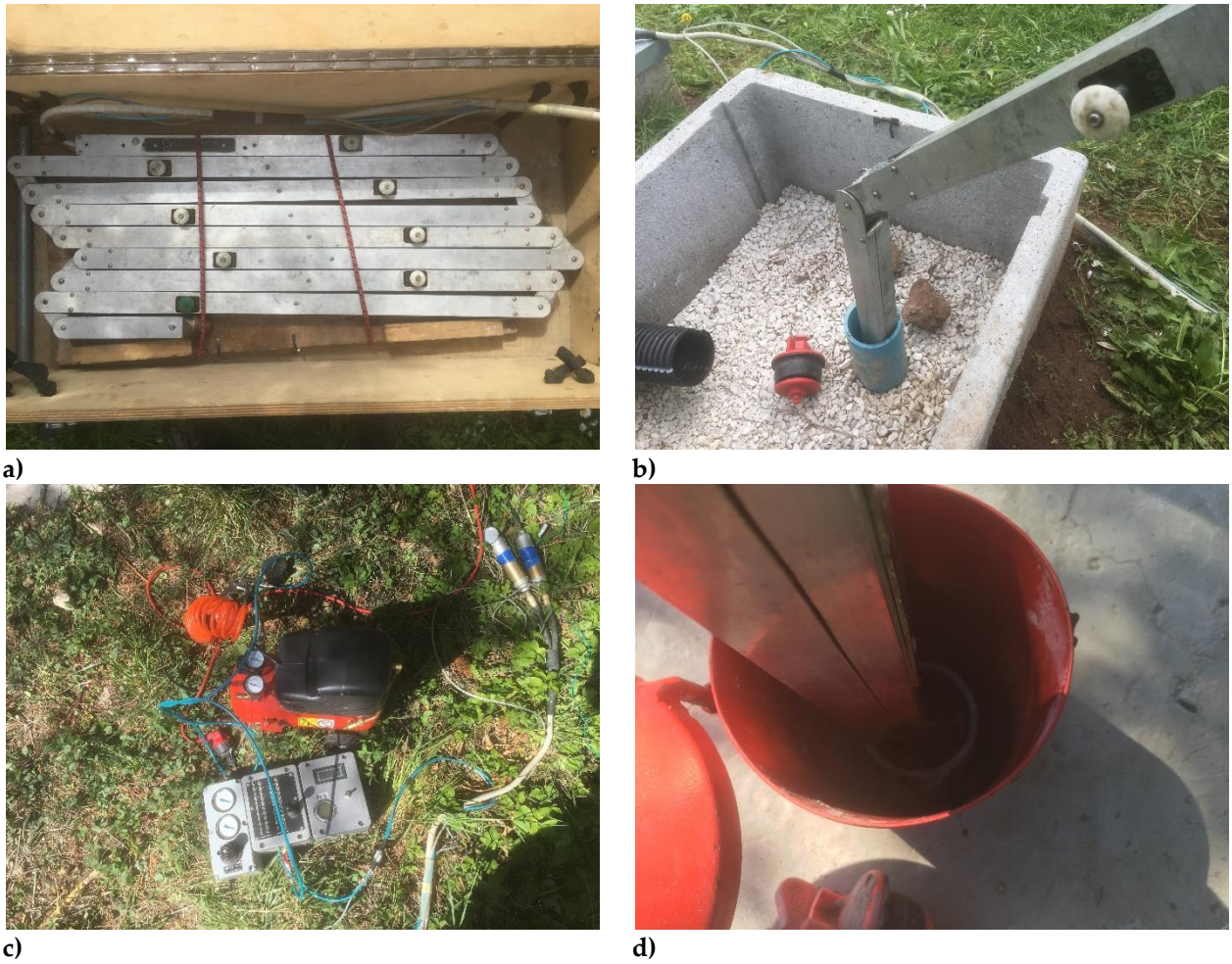

Figure 4.6: a) Generation of P waves by vertically vibration shot on metal plate. b) Impact source for SH wave generation. c) and d) positioning of both the sources.

4.2.1.3 Seismograph

For the acquisition, the digitalization and the recording of the data, we have used the 24-channel digital seismograph ES-3000 Geode © by Geometrics Inc., which allows a 24bit A/D conversion (**Figure 4.7a**). The seismograph interfaces with a laptop on which the data can be checked in real time acquired and at the same time monitor the level of environmental noise. To ensure high accuracy of the instant initial registration, a circuit closing trigger system was used, with mono-polar electric connection to the strike Aluminum plate and to the striking mass.

a) b)

Figure 4.7: a) Geode ES-3000 utilized in this experiment. b) laptop real-time interface

4.2.1.4 Acquisition parameters

Below is a table with the acquisition parameters and receiver geometry used for the investigation:

Parameter	Value
Number of channels	3
Number of receivers	8
Receivers distance	1 m
Sampling rate	32000 Hz
Number of samples	16384
Recording length	312 ms
Sampling interval	0.03125 ms

Table 4-2: Acquisition and design parameters used in the site of Rieti.

4.2.2 Survey layout

Considering the objectives of the borehole seismic test, the correct experimental design and the careful execution of the experiment are of primary importance for obtaining optimal results. Many alternative approaches exist depending on the objective of the investigation and on the field of application. The spatial scale of borehole testing can vary from meters to kilometers, with receivers spacing in the order of tens. Most of the acquisition parameters depend on the target depth and the desired resolution, that in this case can be assumed of the order of magnitude of the receiver spacing (1m).

The term "acquisition geometry" usually indicates the space sampling of the wave field. It is characterized by the geometry of the receiver spread; the number and the position of the receivers define the total size of the array and the receiver spacing (*Strobbia, 2014*).

a) b)

Figure 4.8: In situ views of the experiment located in Rieti

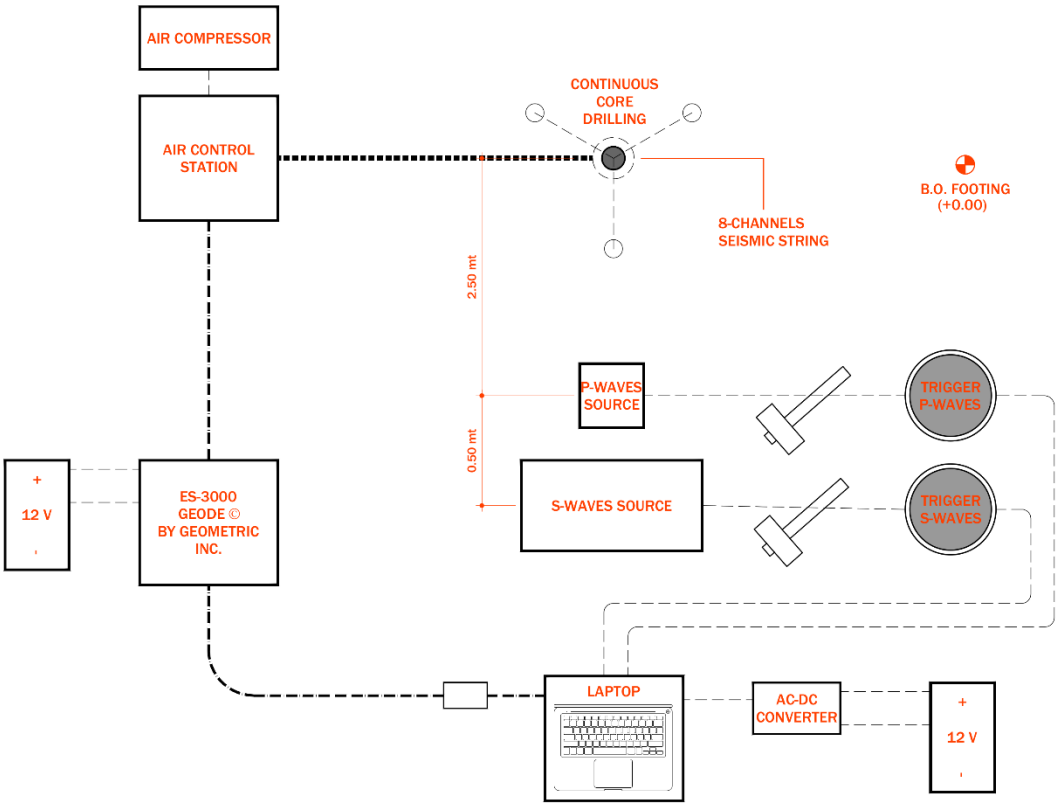

Figure 4.9: Survey layout of the DHT testing

4.2.3 **Select of pairs**

According to Li et al. *(2016)*, the testing geometry should satisfy four conditions to obtain reliable near-surface Q estimates:

- the direct waves used for the absorption estimation should avoid noise and interference effects;

- the source signature should be invariant, or else its effect should be removed in the Q estimation;
- the receiver coupling response should be invariant, or else its effect should be removed in the Q estimation; and
- project costs should be minimized, which is typically neglected in academic research but is an essential consideration in real seismic surveys and in professional practice.

In a classical downhole (DHT) survey, the various tracks are acquired by lowering the geophone, or alternatively a geophonic string, at n-depth within the probing hole. These n-traces can be combined into n-1 non-redundant pairs, according to various configurations. One of the main problems for this type of investigation, when operating in medium-small depth, is the different energization given by the operator at each shot, that affects the waveforms and the frequency content of the generated signal (point 2). Operating with a string consisting of 8 geophones in series, assures that the estimates will always be relative to the same shot, avoiding problems related to the different source signature.

Changes in the source signature can give rise to apparent changes in frequency content with depth, thus causing errors in Qestimates.

4.3 **Data processing**

The goal of processing seismic DHT data at any scale is to increase the S/N ratio. In our case the coherent signal is due to downgoing wave field and the primary objective is to isolate only this wave field.

There are several factors which can affect the determination of Q (*Teng, 1968; Janssen, 1985*):

- Noise deforming the shape of the wavelet and its spectrum;
- multiple reflections simulating non-existent layers and hiding-or interfering with-existent reflections;
- layers which are thin, compared to the dominant seismic wavelength, causing interferences of reflections;
- micro-seismic instrumental or man-made noises;
- poor separation of signals from neighboring events;
- lack of knowledge of the crustal structure at the recording site;
- under-damped recording instrument.

A total of 44 records of P and SH waves were used in this analysis.

Figure 4.10 shows an example of the raw data sets obtained, so-called shot gathers. The different kinds of waves that clearly can be seen are the direct and/or refracted wave, the airwave, tube waves, and several reflections. For the reflection seismic method, the downgoing reflections are the only data we want, the others are "noise". This noise generated by the seismic source itself is coherent noise, in contrast to random noise. To

convert the data recorded in the field to the final seismic section, preferably a depth section, processing is necessary.

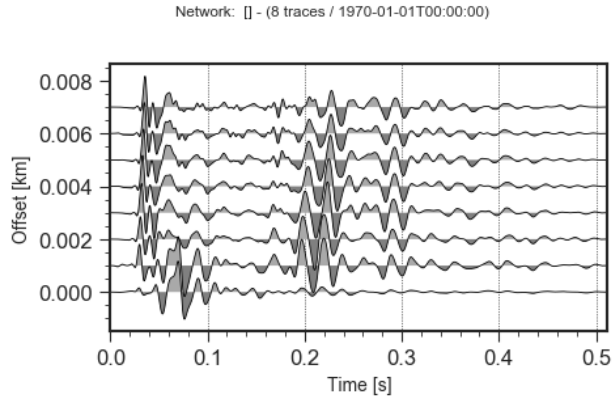

a)

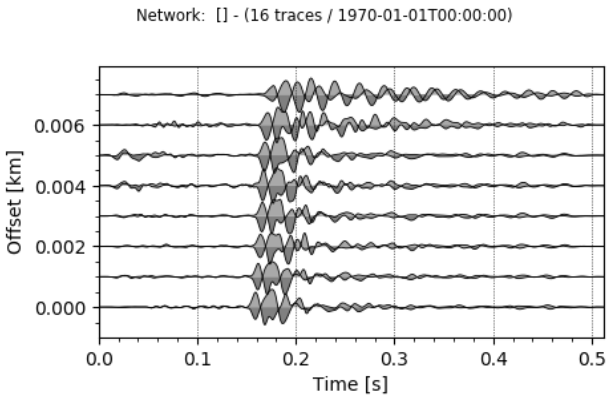

b)

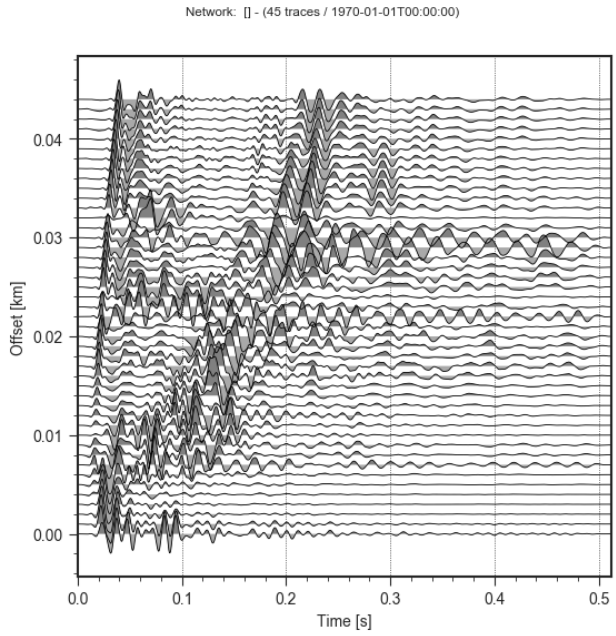

c)

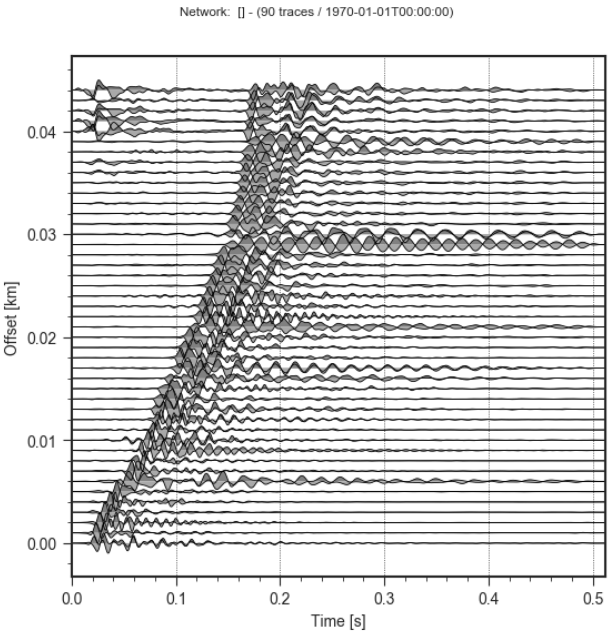

d)

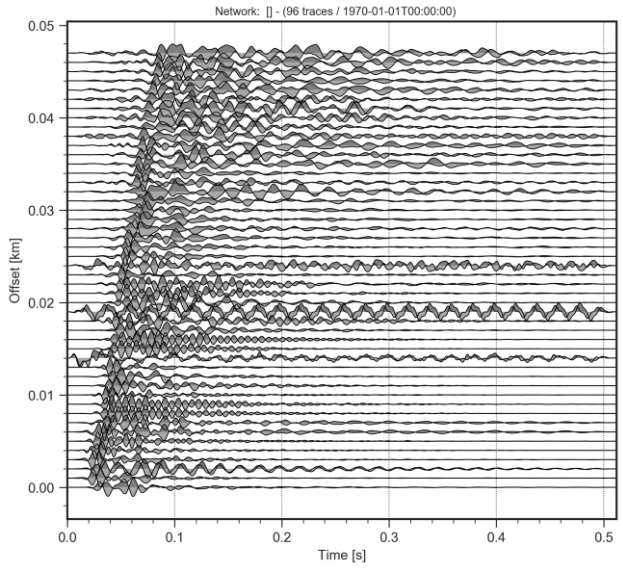

e)

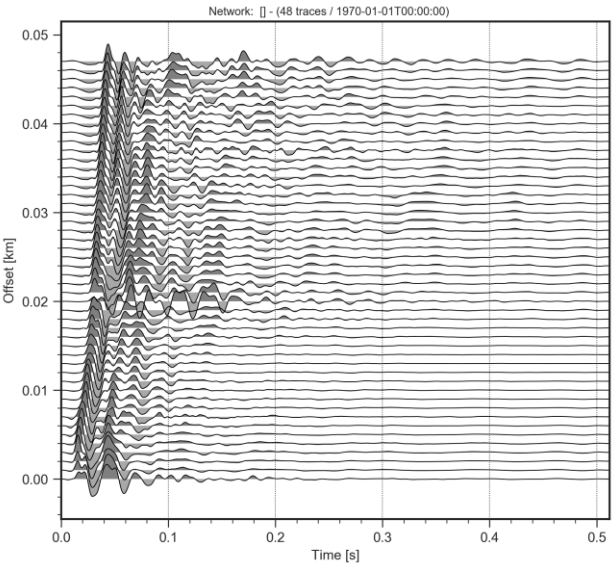

f)

Figure 4.10: a) and b) example of single shot gathers for P and SH waves. c) and d) full seismic gathers for P and SH waves of Test site 1; e) and f) full seismic gathers for P and SH waves of Test site 2.

Increasing S/N ratio can be obtained directly in situ applying some obvious precautions like a good earth-receiver and earth-source coupling. As pre-processing, I have selected 5 principal steps that are listed below:

- polynomial regression;
- first break picking and travel times;
- trace muting;
- frequency analysis (frequency content);
- trace windowing.

4.3.1 **Choice of traces and vertical stacking**

The particular survey geometry that has been chosen resulting in an overlap of three traces between two subsequent acquisitions. Trace selection depends on the direct observation of the seismic signal. Traces affected by disturbance of bad coupling problems have been replaced by a visual inspection, considering the overlap traces too (**figure 4.11).**

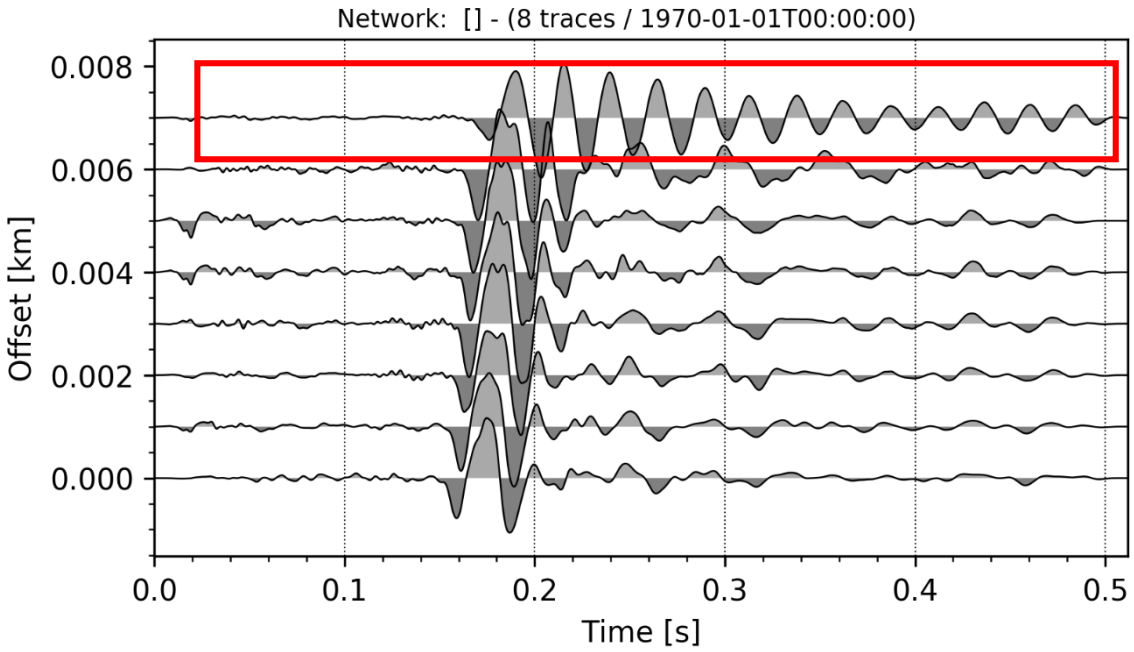

Figure 4.11: Visual inspection of a single seismic gather (SH 8-channel)

A stacked section is instead a processed seismic record that contains traces that have been added together from different records to reduce noise and improve overall data quality. The number of traces that have been added together during stacking is called the fold. For each measurement station the number of repeated energizations (stacking) and

the number of recordings was chosen in the rate of 8 stack. Some measurements needed a real-time vertical stacking depending on the noise.

4.3.2 **First break picking and travel times**

Near the first arrival, seismic traces are not stationary, so the frequency content of an early window is sensitive to its position. For spectral ratios to measure the earth filtering, care should be taken to window the same phases on all traces. In the absence of significant dispersion, this can be done by adjusting the cutting window position so that the first arrival peaks at 5-ms before to the beginning of the window on every trace of the segment. This is an important detail in the preparation for absorption estimation. Inconsistent windowing causes erratic behavior of the spectral ratios (*Mateeva, 2015*).

The time delay τ between the receivers in a given pair ($\tau = (t - t_0)$in equation (**3-5**)) can be measured from the first arrival peaks with a precision of the order of the sampling interval. The arrival of the signal is identified on the basis of the following observations:

- For the SH waves, presence of specular pulses in the horizontal components of the recordings made with energizations of opposite directions;
- frequency variation of the wave train.

The picking of SH wave arrivals is done manually by comparing, for each station depth, the two opposite polarizations of shear wave SH (made in situ by relative rotation of the seismic source of 180 °). In the following figure (**4.12**) we can observe the comparison of the two opposite polarizations (SH1 and SH2) for first break picking.

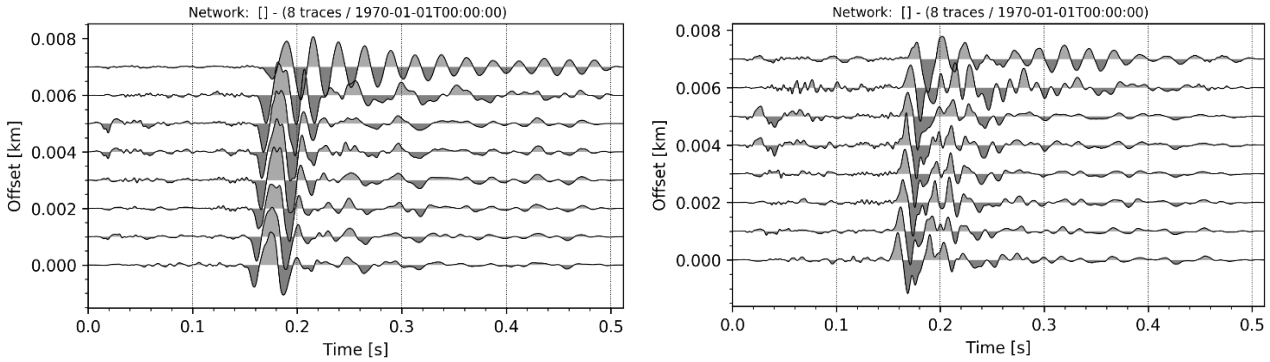

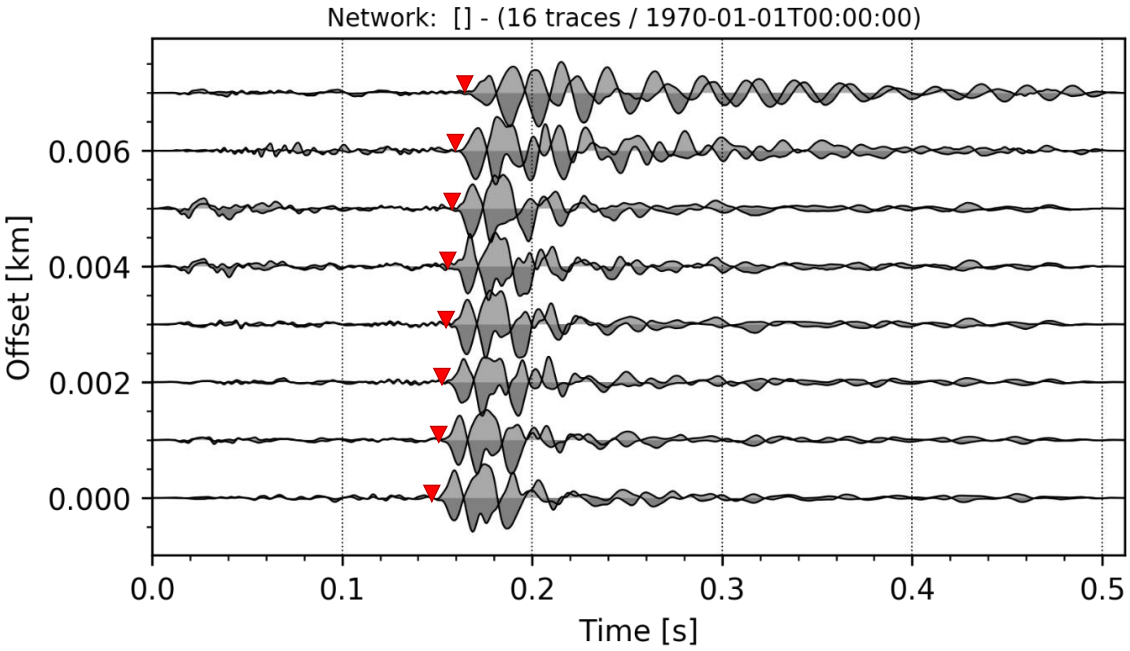

Figure 4.5: Example of comparing SH waves polarization, by means of the specular pulses we can find the first break (red markers).

4.3.3 **Frequency content**

The frequency content analysis of the signals in the frequency domain can help in identifying the usable frequency band and it is useful in two step of our processing: a) selection of frequency range of the coherent signal (body waves) b) identification of the frequency band of the logarithmic ratio on absorption estimates.

A particular procedure to assess the energy content consists in applying low pass filters with decreasing frequency thresholds to evaluate the lower frequency bound of usable data and high pass filters with increasing frequency thresholds to evaluate the frequency upper bound (*Foti, 2018*). This procedure has been applied on seismic traces in both of the experiments and sites (VSP and MASW). It provides indications on the usable frequency content and allows to design a correct band-pass filter to apply on each seismic signal of the database, in order to focus the dominant seismic signal, filtering out the noise and other interference.

In general, frequency filtering is a technique to enhance the resolution in frequency domain by suppressing the noise, mostly associated with higher frequencies.

Four variants of filtering are commonly applied:

- Low-cut (only high frequencies are allowed to pass);
- high-cut (only low frequencies are allowed to pass);
- band-cut (a band of frequencies is restricted from passing);
- band-pass (only a specific frequency band is allowed to pass).

In the following figure we can see an example of the processing of seismic gather applying low pass and high pass filters to check the correct frequency content.

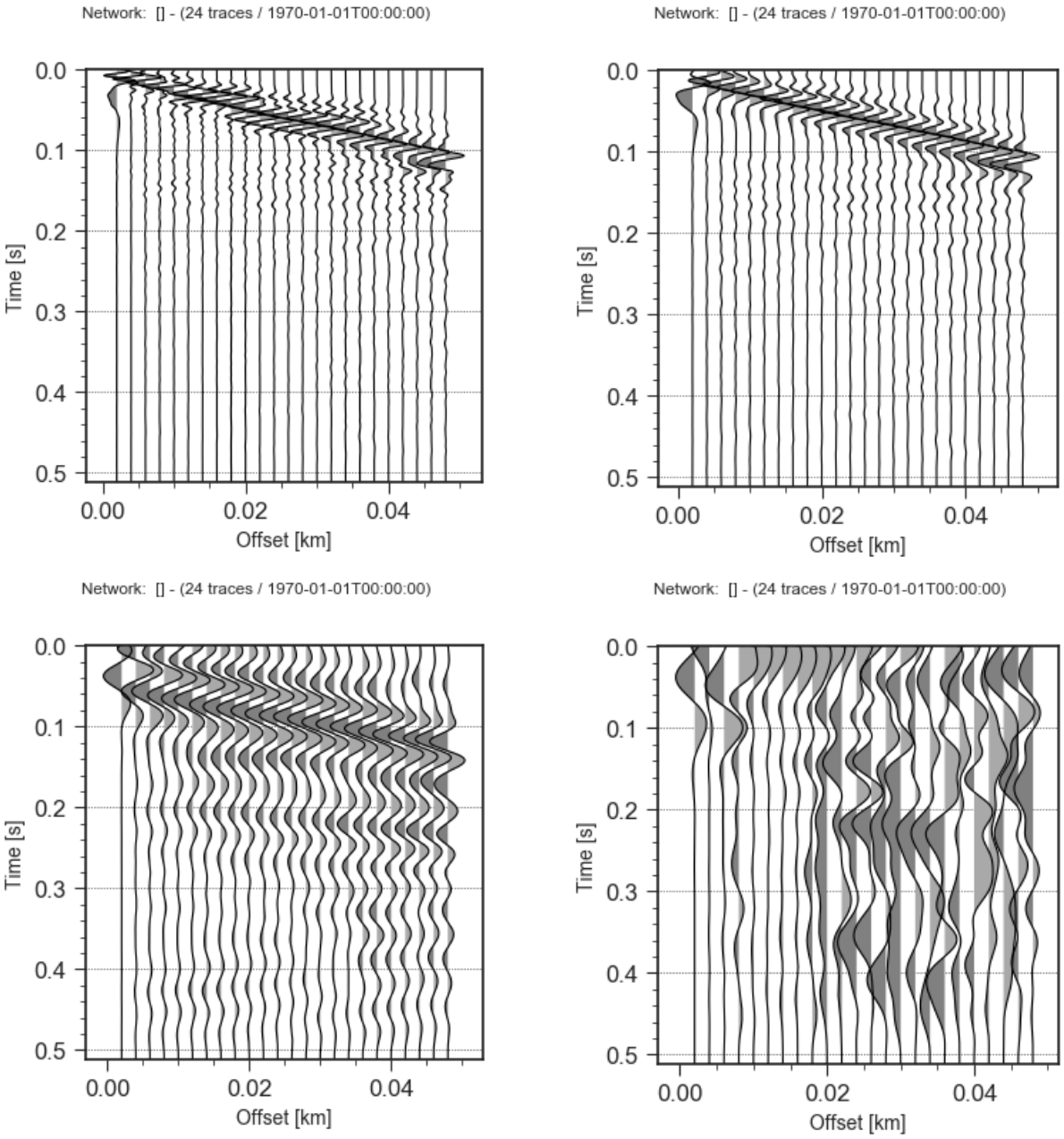

Figure 4.6: Example of check of the low frequency content (data from Rieti site, MASW surveys). a) Raw data, b) data with low pass filter 60 Hz (OK), c) data with low pass filter 20 Hz (partial OK), d) data with low pass filter 10 Hz (the signal in not dominant anymore and the wavefield is dominated by noise).

On the VSP datasets, applying the same methodology, has then been applied a 10-150 Hz butterworth band-pass filter to remove incoherent noise (electric noise, other wave types, etc.)

In order to get reasonable attenuation estimates, it is extremely important to identify the frequency content or band over which the signal to noise ratio is sufficiently high.

Once the signal is processed, in the SR method, the identification of the correct frequency band to apply the linear regression is even crucial, while in the RT method a filter can be applied only for a clear identification of the first cycle of the seismic signal, since we

cut the remaining part. In this work, the frequency band selected for SR processing is where the signal to noise ratio is quite high (see on figure 2.2), and where the amplitude spectrum shows the maximum values on the abscissae, considering the remaining part only due to noise. The spectral ratio shows reliable attenuation values in the frequency band where the spectrum is more energetic. Another instrument that can help to find a correct frequency band is the Spectrogram of each trace of the seismic stream (**Figure 4.14**).

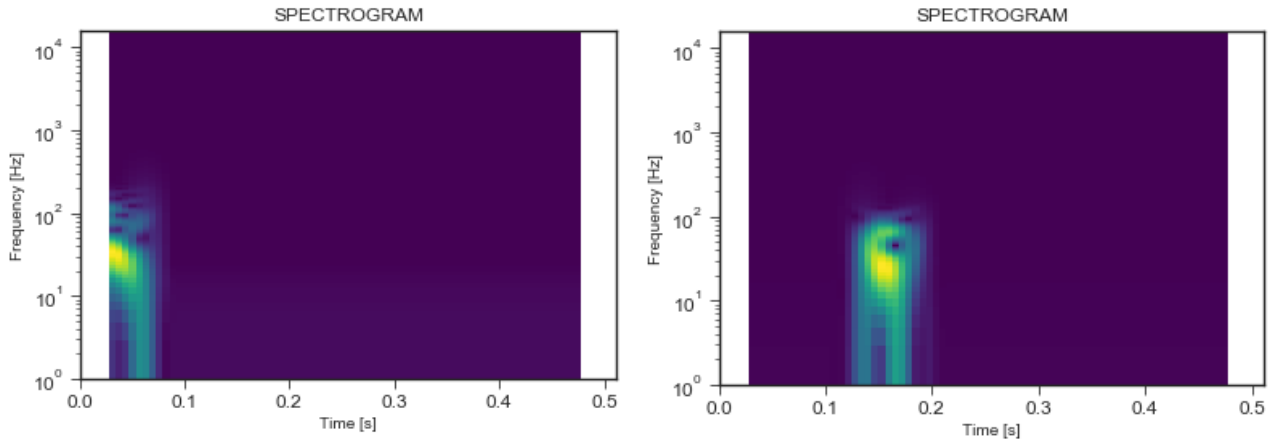

Figure 4.7: Example of Spectrogram (P and S waves) in the choice of frequency band.

To avoid the instrumental response (geophones), it was decided to make a further cut of the lower frequency band (0-15 Hz), that can interfere with the survey frequencies. As can be seen in the figure (**Figure 4.15**) the spectrum shows the peak of energy most focused in the 15-60 Hz frequency band, decreasing rapidly for higher frequencies, but keeping the amplitude at low frequencies almost unchanged increasing in depth.

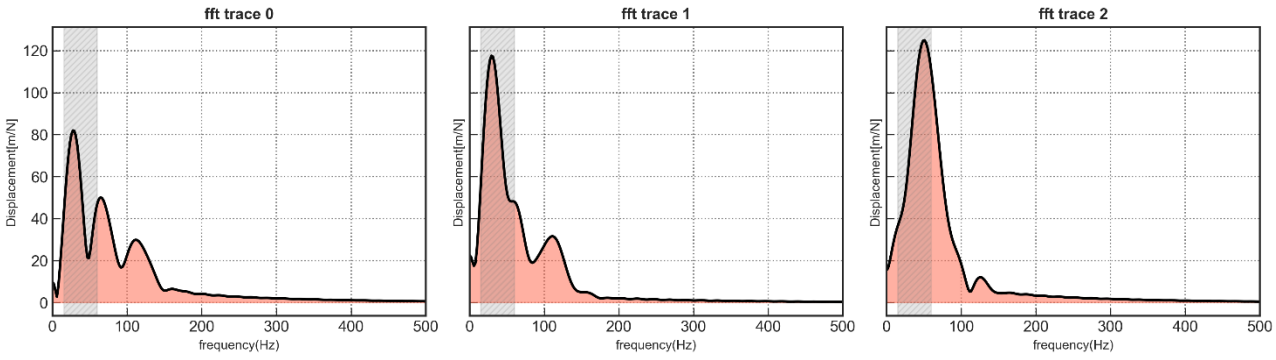

Figure 4.8: Example of the choice of frequency band by means of FFT spectrum analysis (S-waves, Rieti site).

Since scattering from thin layers will be explicitly taken into account in the absorption estimates, it does not represent "noise" (when not taken into account, this source-generated "noise" is a dominant cause of bias and uncertainty). The noise in our data is the ambient background that can be seen on the VSP traces before the first arrivals.

As is seen from figure **4.14** and **4.15**, only frequencies between 15 and 60 Hz can be used for absorption estimation; the rest of the spectrum is dominated by noise. On most traces the signal-to-noise ratio in the usable frequency band is about 15-50 Hz.

In the following table, there are all the frequency bands choices for the experiment.

Test Site	Wave type	Bandpass filter (Hz)	Chosen Frequency band (Hz)
Rieti	P	10-150	**15-50**
	SH	10-150	**15-60**

Table 4-3: Frequency bands used for the absorption estimates.

4.3.4 **Muting**

Muting is aimed at optimal removal of wave intrusions and other low amplitude noises present in the raw wave field. It is performed by selecting two limiting scanning seismic velocities on the wave field, meant for top-muting and bottom-muting, based on which the events above and below the corresponding limits will be removed. The purpose in this case to eliminate the noises preceding the first arrivals, and after two or three cycle of vibration.

Muting in this domain is not typically thought of as filtering, but the same care must be taken in identifying noise and signal, determining the best muting to apply to enhance the S/N ratio, and selecting the mute taper to avoid introducing unwanted artifacts.

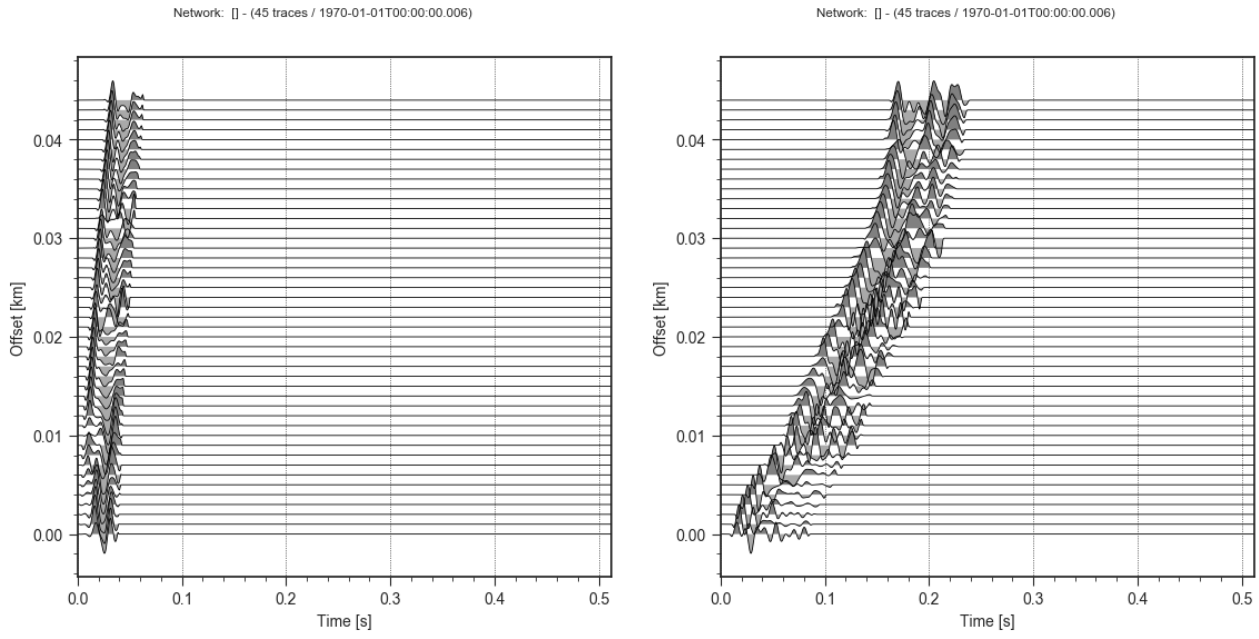

a)

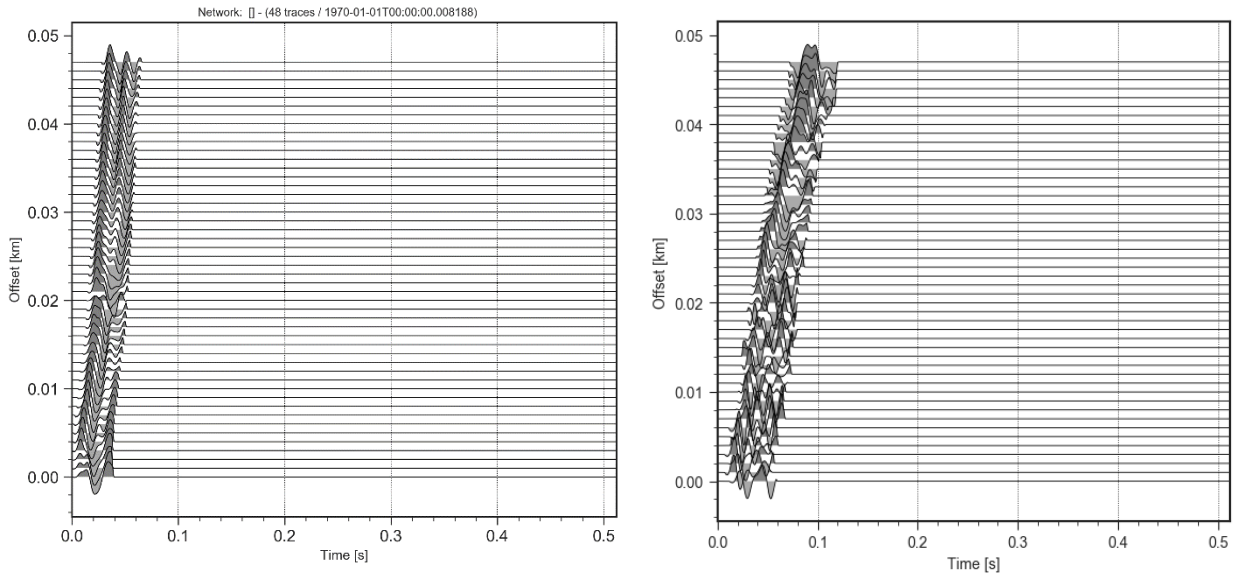

b)

Figure 4.9: Example of muting applied to the seismic dataset. a) test site 1; b) test site 2.

The main components of spatially limited coherent noise that affects the wavefield in near-surface VSP data are generally multiple refraction, ground roll, air-wave, air-coupled waves, tube waves and other early-arriving noise.

Filtering in the $x - t$ domain, or muting, is a straightforward way to separate (remove) noise from signal. Muting of refracted and direct-wave energy is typical of both exploration-scale and near-surface data and is necessary on most data sets to ensure the noise does not appear coherent on VSP stacked sections and result in geologic misinterpretation.

Although care must be taken to identify refractions and reflections correctly, the muting process itself is straight forward.

With smaller receiver spacing and target depths, like in our case, the airwave phase and other incoherent waves usually arrives to contaminate the signal, for larger spacing instead arrives too late.

A method of noise attenuation for near-surface surveys data mentioned in the literature is to mute everything arriving later than the airwave when no signal is identified in that region.

Muting helps to suppress the wavefield characteristics recorded beyond specific seismic velocities. Introduction of excessive muting may result in significant loss in the wavefield characteristics, and hence, muting operation should be controlled so that an optimum energy content of the signal is maintained while removing the adulterating noises.

Muting is carried out by eliminating the wave signatures which are not in phase. The muting operation is carried out along the slope of the identified prominent phases of the wavefield.

These observations suggest that muting alone cannot lead to the generation of a reliable absorption estimates. Hence, muting on the filtered wavefields is recommended.

In this work we have applied a muting before and after a 50 ms cutting window functions for SH waves and 20 ms window functions for P waves (**Figure 4.12**).

4.3.5 **Windowing**

We can minimize the effects of performing an FFT over a non-integer number of cycles by using a technique called windowing. Windowing reduces the amplitude of the discontinuities at the boundaries of each finite sequence acquired by the digitizer and consists of multiplying the time record by a finite-length window with an amplitude that varies smoothly and gradually toward zero at the edges. This technique is also referred to as applying a window and it is useful to improve the frequency spectrum of the FFT.

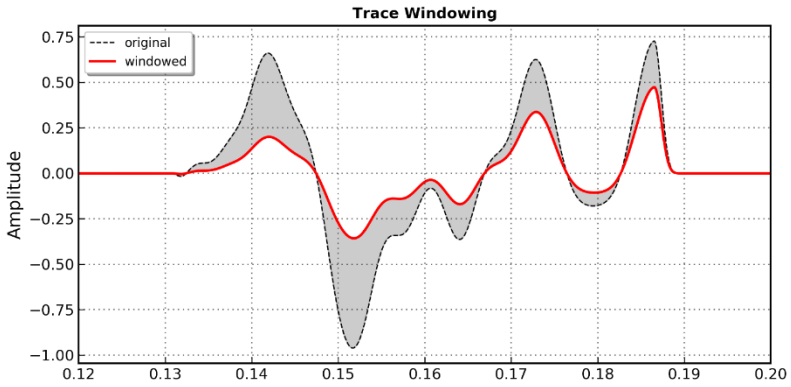

Figure 4.10: Example of trace windowing with a Blackman-tapered time window function.

4.4 Data results

4.4.1 **Spectral ratio results**

In this section, the SR method is applied using seismic near-surface VSP data, explained in detail in the previous section, with details on processing and acquisition parameters.

The results of the processing were the extraction of the downgoing wavefield cleaned by other wave components and noise. The results of wave separation and processing using an improvement wave-by-wave separation approach is showed in **Figure 4.13**. The extracted downgoing wavefield was used for interval Q estimation.

4.4.1.1 **High level Fast Fourier Transform**

A high level FFT sub-routine is applied to the time signals, and these signals are displayed and stored domain amplitude using PYTHON code. The FFT algorithm converts the time domain signals to frequency domain and computes the discrete Fourier transform of the amplitudes of the time domain signals by taking 16384 points.

The natural logarithms of the spectral ratios between the reference signal and the arrivals recorded at subsequent geophones were then computed and plotted as a function of frequency to derive the slope of the logarithm spectral ratio, alpha, which, according to Equation (2-1), is a function of Q and the travel time between the two arrivals. We can see on **figure 4.17** the reduction in the spectral amplitude due to the attenuation of the signal

increasing along the depth of the investigation. This corresponds to a peak displacement towards lower frequencies, which is also clear in the temporal domain, with high-frequency components, which are predominant in the first layers, that are gradually disappearing as the depth of investigation increases. This dependence on the frequency and widening of the wave front are the basis of the choice on the application of the RT method, less affected by frequency issues.

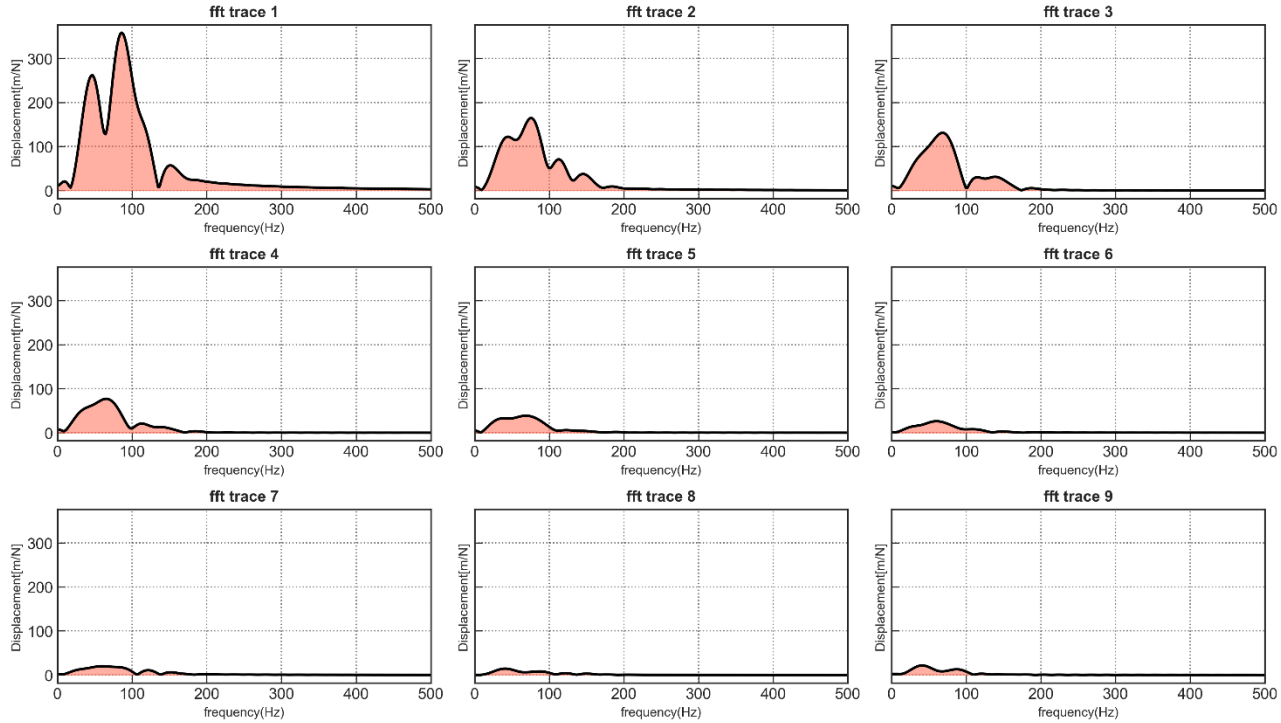

Figure 4.11: Amplitude spectra of the downgoing wavefield, we can notice the descrising in amplitude, increasing depth of investigation.

We see that the most of energy spectrum is within 10-100 Hz, with the center frequency at 50-60 Hz. To select the frequency content for Q estimation, we consider a logarithm of the amplitude spectrum ratio for different frequency band for P and SH waves (**Table 4.3**).

4.4.1.2 Logarithmic ratio and apparent attenuation

The reduced spectral ratio $\ln[A(\omega)/A(\omega)]$, were calculated in according with equation **3-8**. **Figure 4.19** shows the logarithm of amplitude spectral ratio for the bandwidth 0-150 Hz for 9 intervals (43 total intervals). The so called reduced spectral ratio shows a very good linear trend between 15 and 50 Hz for SH waves, especially for deeper ratios. P waves shows a linear trend between 25 and 55 Hz. We can see that within the frequency band 15-50, these curves can be approximated with the linear function.

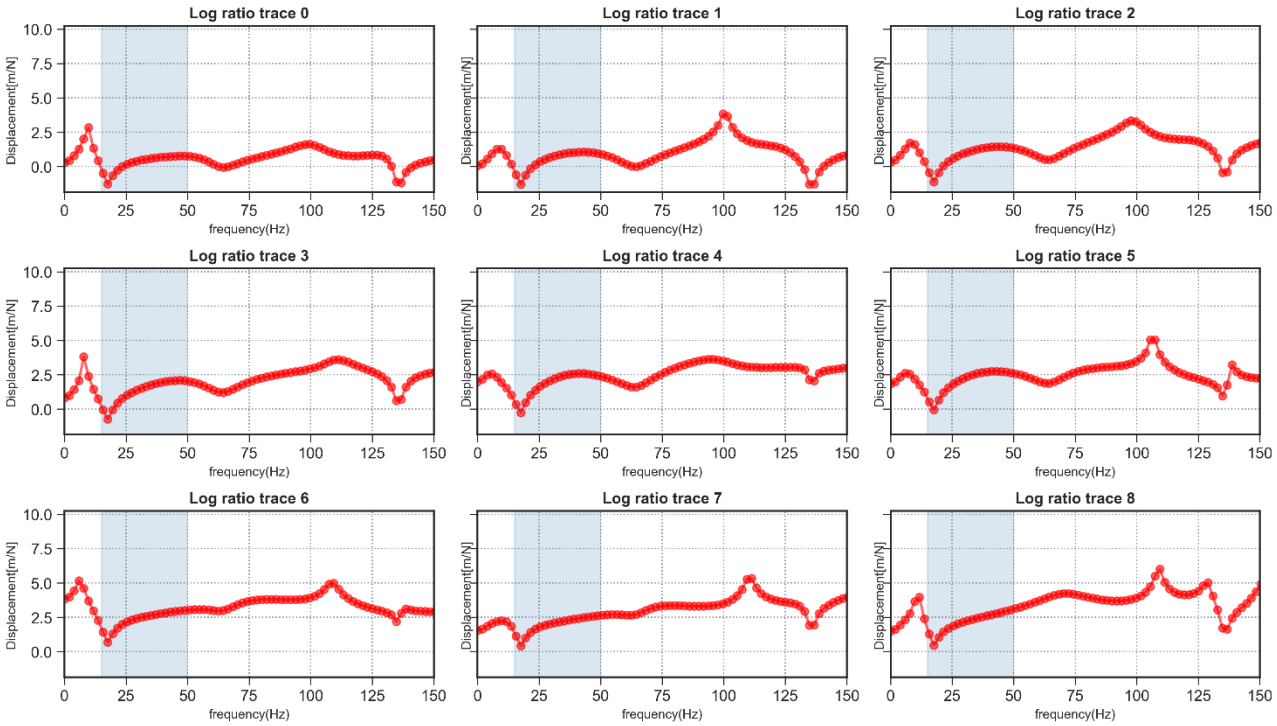

Figure 4.12: Spectral ratio between various recording pairs.

Once we have fixed the frequency band to perform the linear regression, we can now calculate the apparent attenuation $\gamma(\omega)$ (**equation 3.5 – section 3.1.3.1**), for each receiver pairs, that is related to the slopes values obtained. Some typical reduced spectral ratios values are presented in **Figure 4.19**, that also shown the least-squares fitted straight lines (in the blue-span).

4.4.1.3 Estimation of Q factor

As we expected, when plotting the differential attenuation values vs depth, we see an increasing with the distance from the source. Some deviating values, can be due mainly to scattering phenomena or a defective receiver coupling with the borehole. We can notice a net increase of apparent attenuation between 5-10 meter depths, especially for SH waves.

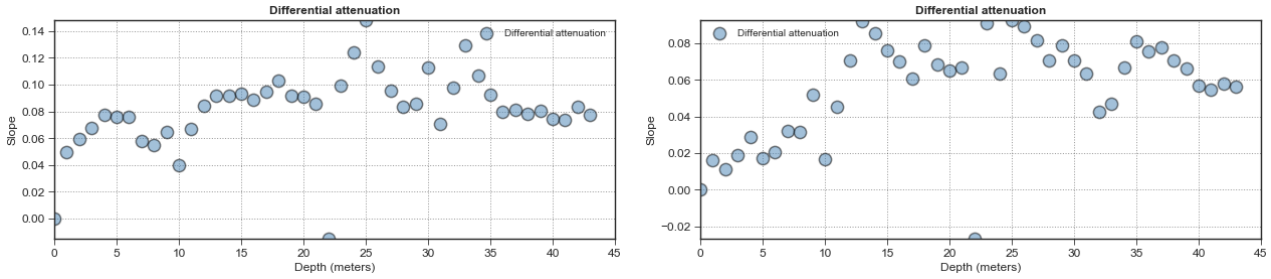

Figure 4.20: Differential attenuation versus Depth of investigation for the Test site 1, calculated for P and SH wavefields

Some out of range values of apparent attenuation, as we mentioned before, due to a bad coupling between receivers, and strong disturbances, are connected with a poor quality

of the selected traces. Being strongly influenced by local interference, these values of m (slope) are simply reject or mediated from the absorption estimation. We think that these negative values are strongly related even to the scattering phenomena.

Such values are readily observable even if the spectral ratio slope is fit over a larger frequency band (*Mateeva, 2015*).

For the two datasets the slope values are divided by a minimum of 0.032 up to a maximum equal to 0.143 recorded in the last meters for P-waves, and a range of 0.004 up to 0.098 for SH waves measurements.

In according with **equation 3-11**, once we have calculated reduced spectral ratio and apparent attenuation, we can now obtain intrinsic interval quality factor Q_P and Q_S estimates from the different receiver pairs and different depths. The Q values as obtained using spectral ratio method are showed in **Figure 4.21** and tabulated in **Table 4.4**.

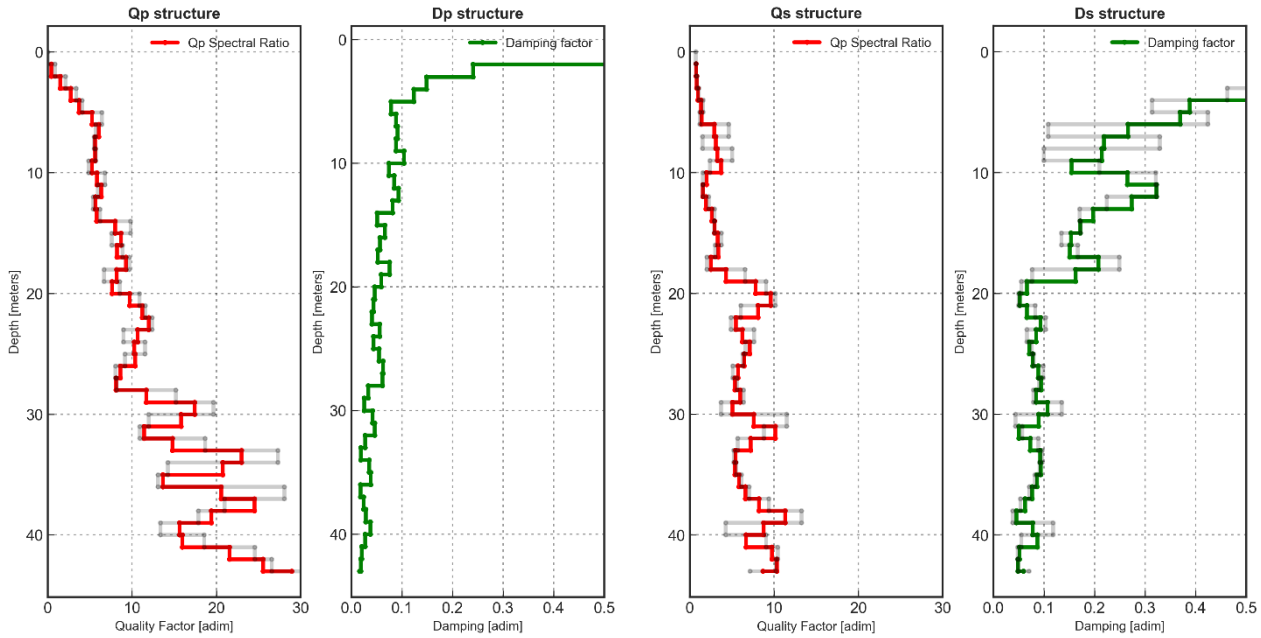

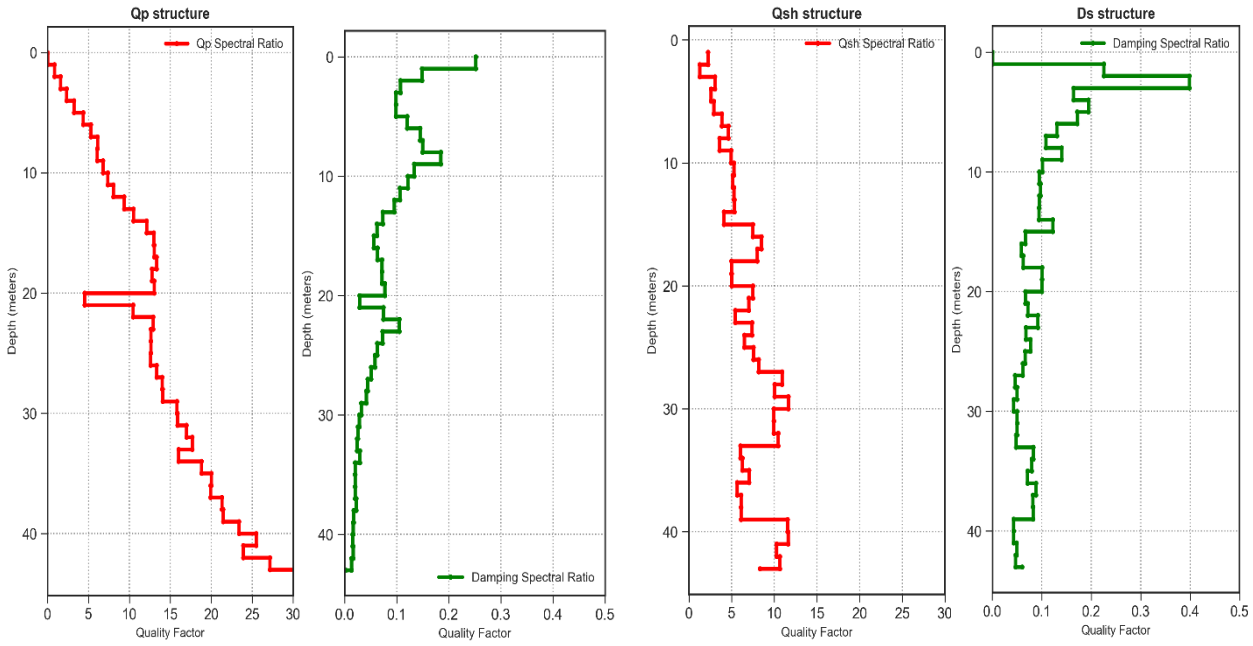

Figure 4.13: Test site 1; a) Interval Q estimation and Damping factor versus depth for P waves. b) Interval Q estimation and Damping factor versus depth for SH waves; Test site 2; c) Interval Q estimation and Damping factor versus depth for P waves. d) Interval Q estimation and Damping factor versus depth for SH waves

A good correlation with layers is noticed, with changes in absorption values, especially for greater depths of investigation, with some peaks in the passages between layers.

The profiles show a very low Q values for P and S waves. We find that S waves attenuate more strongly than P waves ($Q_S/Q_P \cong 0.5 - 0.6$).

According to theoretical considerations (*Lay and Wallace 1995*), Q_S/Q_P for the world should be 9/4 or 2.25. However, worldwide reported values deviate significantly from this theoretical value (*Yoshimoto et al., 1993*).

Hough and Anderson (*1988*) opined that $Q_S/Q_P \geq 1$ for most types of scattering, whereas Padhy (*2009*) states that high value of this parameter is expected when scattering from shallow heterogeneities in the crust is involved. The value of Q_S/Q_P is around 4/9 for a medium where attenuation is completely due to intrinsic attenuation and no scattering attenuation takes place (*Lay and Wallace, 1995*).

The higher the value of Q_S/Q_P, especially for the Rieti test site, the higher is the scattering, hence the more the heterogeneity. In the INGV test site the value is lower due to the greater stratigraphic homogeneity.

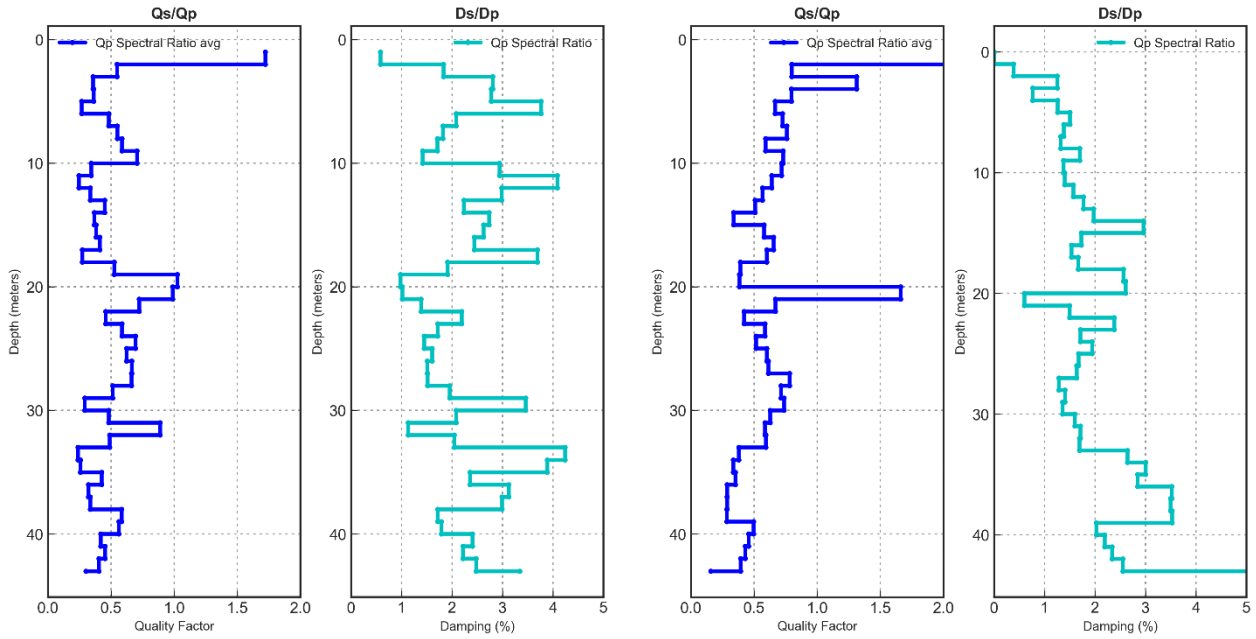

Figure 4.14: Qp/Qs and Ds/Dp ratios for the 2 test sites

4.4.2 **Rise-time results**

The second method used in this study is the rise-time method, described in detail in **section 3.1.2.1.**

The main purpose of this method is to extract good quality seismic data related to the first cycle of vibration in the time domain. The same pre-processing procedure used in SR method has been adopted for RT absorption estimation. The pulse-broadening method is advantageous because very short length of seismogram is required. So we have directly isolated each trace with a short 20-ms time windows with Blackmann-Harris window function.

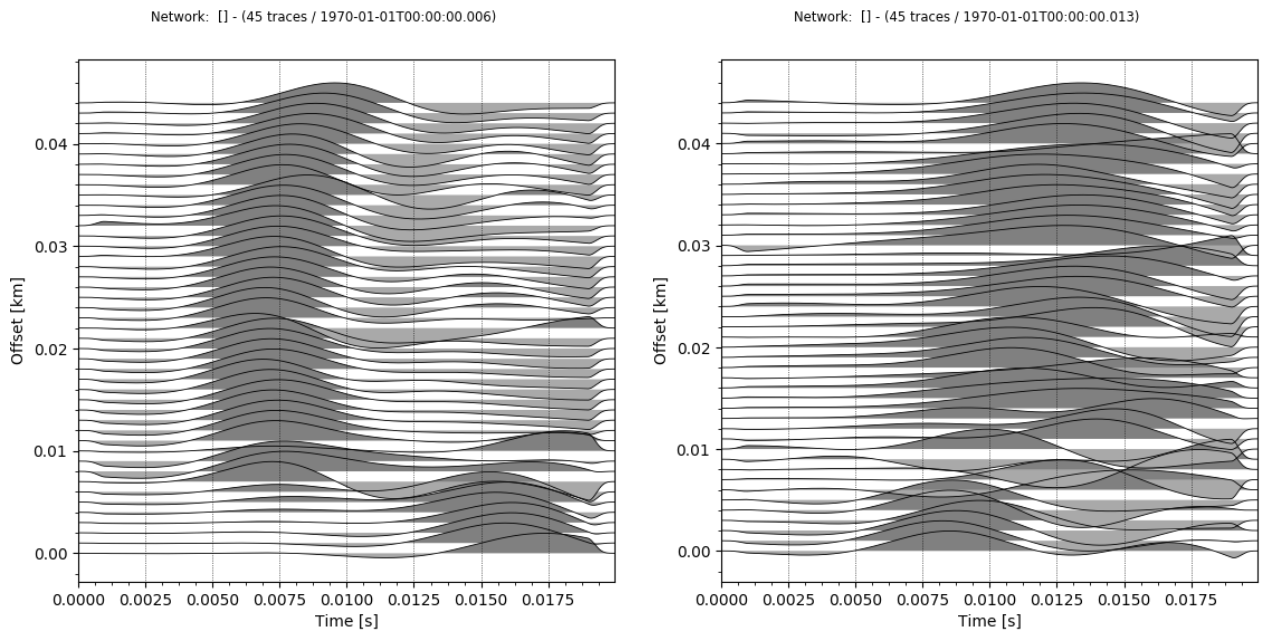

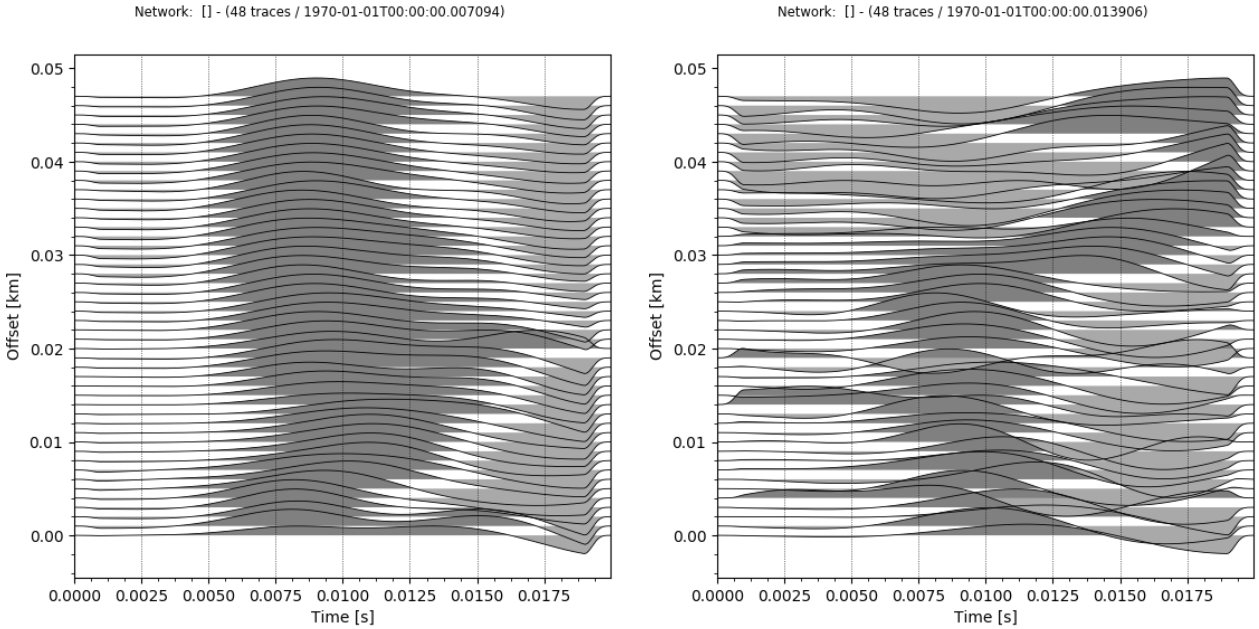

Figure 4.15: 20 ms - isolated traces for rise-time estimation for the 2 test sites.

The data in **Figure 4.23** shows the 44 processed traces for P and SH waves. This method requests a good quality seismic data in order to avoid incorrect estimates of the rise-time, due to double peak, low S/N ratio, etc.

It s been implemented an algorithm in PYTHON to process this data and extract the rise-time values for each depth of investigation.

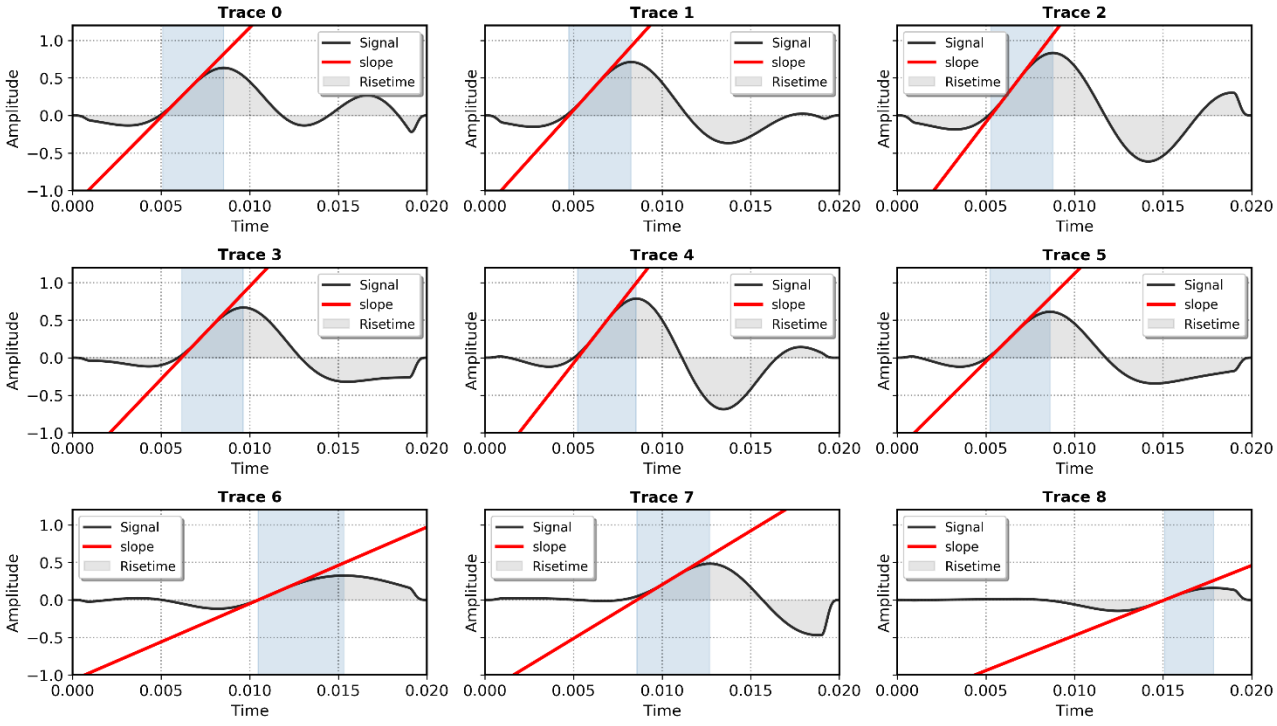

Figure 4.16: Example of rise-time estimates. In red the maximum slope of the first quarter-cycle of the seismic signal.

In **Figure 4.24** we can observe the calculated rise-time for a set of 9 seismic traces. The rise-time show an increasing in depth of investigation, due to widening of the first cycle of the signals. Incorrect values have been directly rejected from the processing.

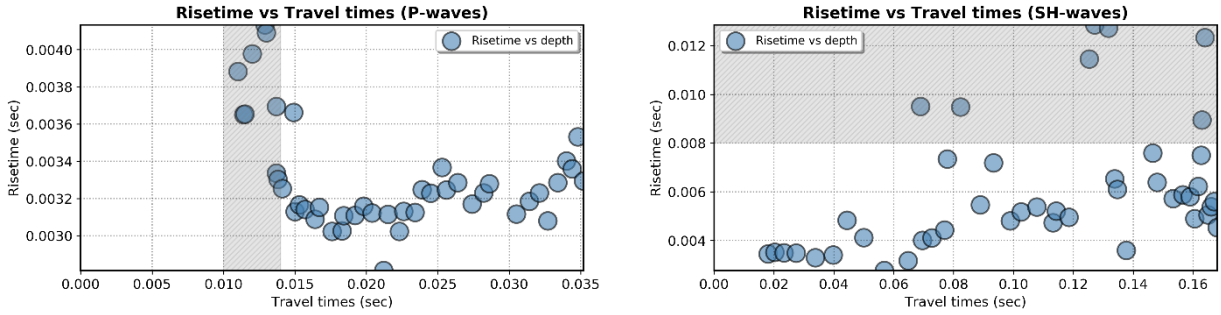

Figure 4.17: Experimental rise-time as function of travel times.

Figure 4.25 shows the experimental rise-times for P and SH waves plotted as a function of travel times that have been estimated in the first break picking in **Section 4.3.2.** and presents the comparison of the profiles obtained with the spectral ratio method one. Since our data come as velocity seismograms (we used 10 Hz velocity-geophones), we adopt $C = 0.485 \approx 0.5$ based on theoretical results (*Kjartansson,1979*).

By operating a linear regression over an a priori layer division we can estimates intervals Q in according with **Equation 3-2** in **Section 3.1.2.1.**

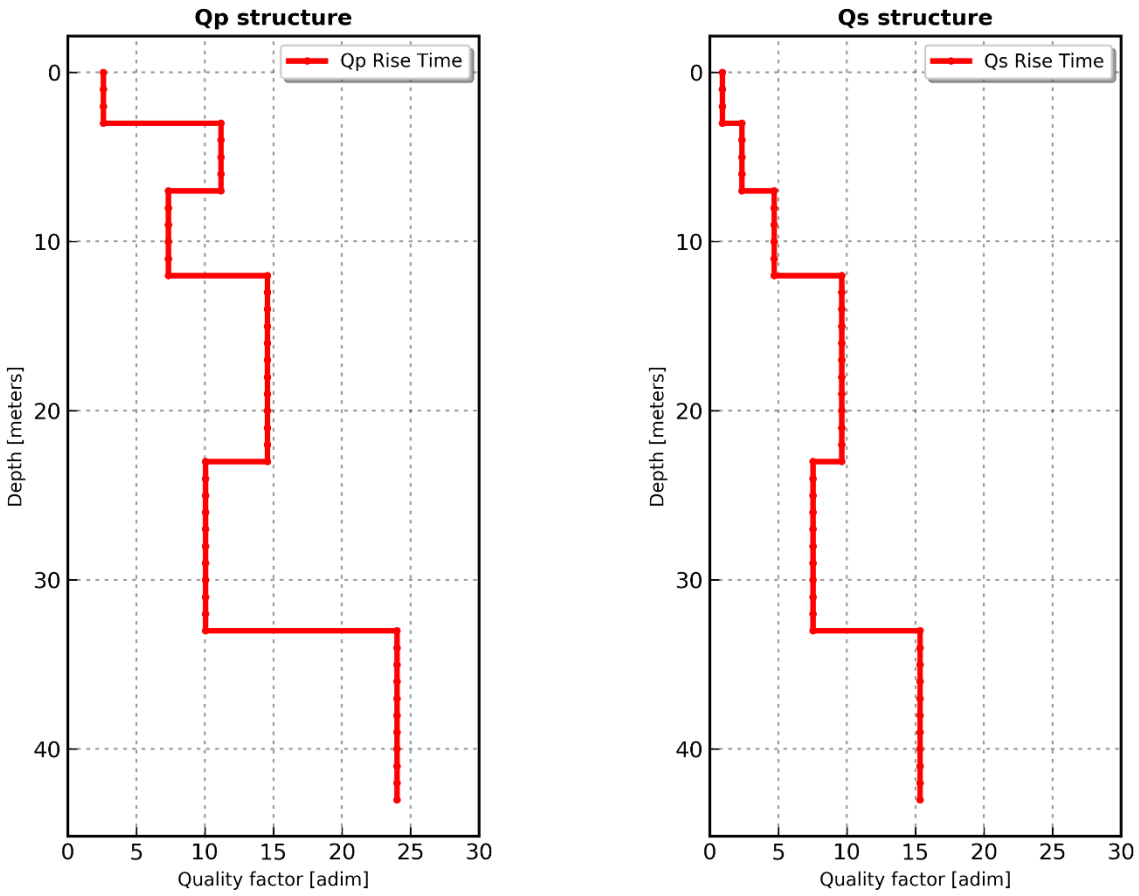

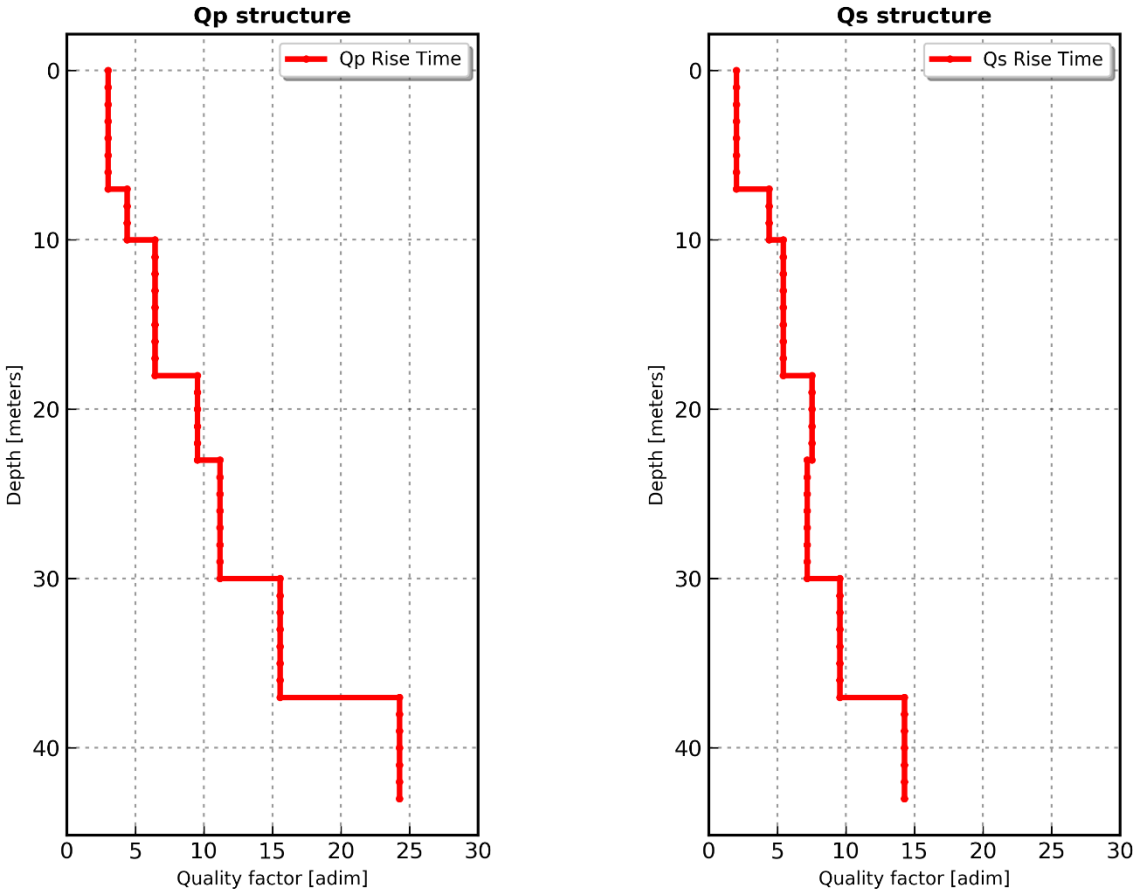
Qp structure
Qp Rise Time
Depth [meters]
Quality factor [adim]
Qs structure
Qs Rise Time
Depth [meters]
Quality factor [adim]

a)

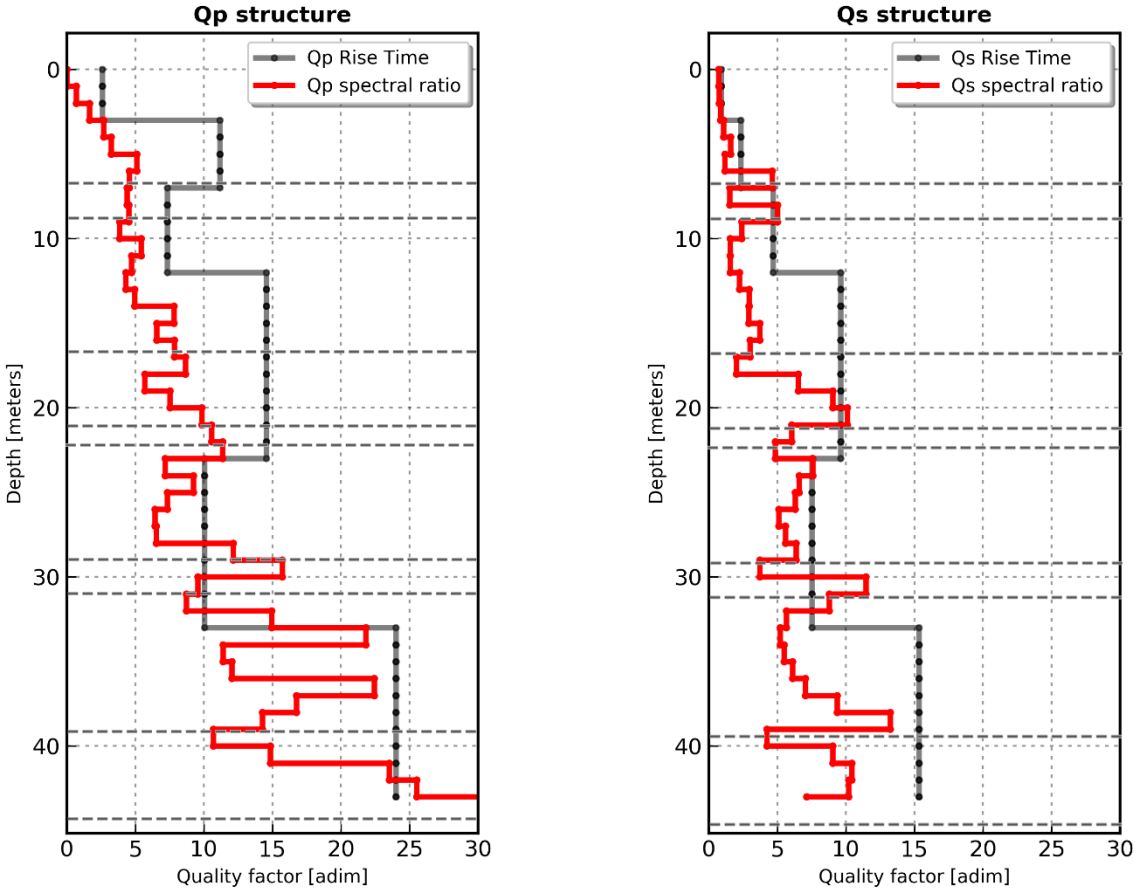
Qp structure
Qp Rise Time
Qp spectral ratio
Depth [meters]
Quality factor [adim]
Qs structure
Qs Rise Time
Qs spectral ratio
Depth [meters]
Quality factor [adim]

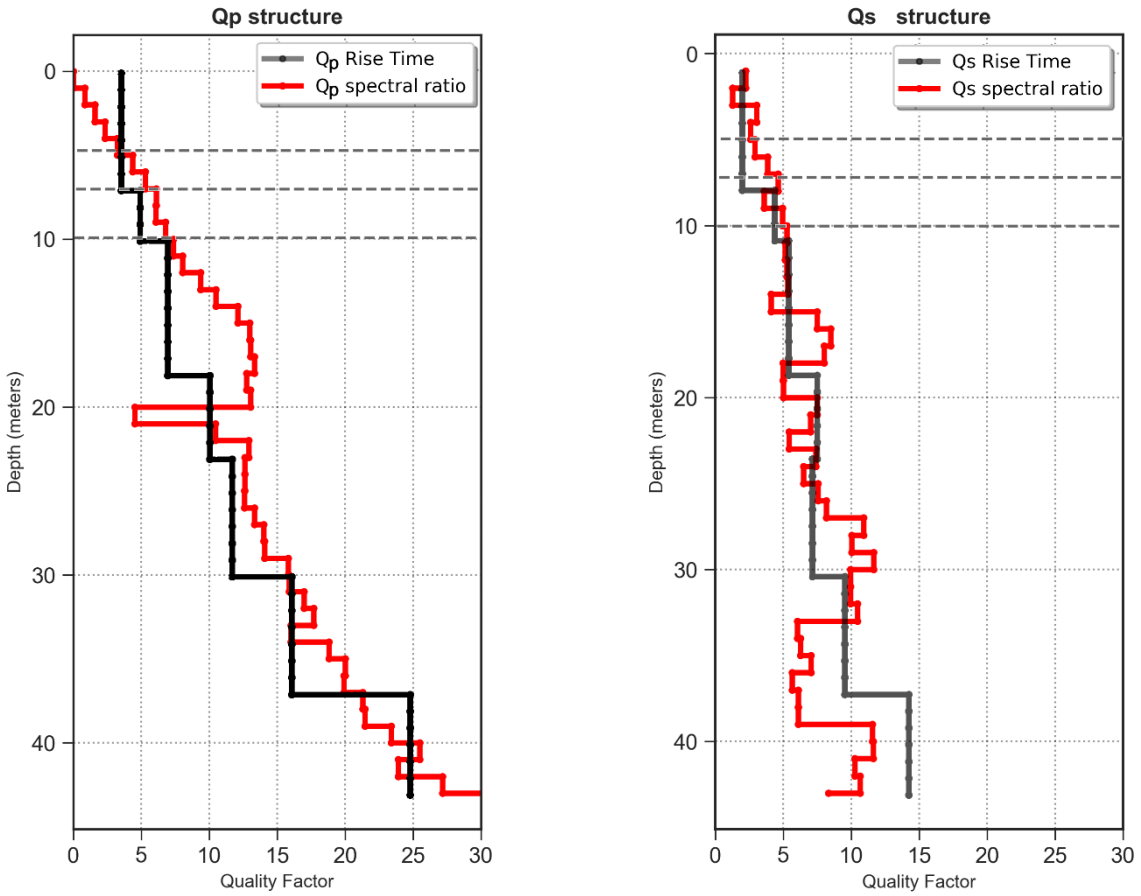

b)

Figure 4.18: Interval Q_P and Q_S for Rieti site using rise-time method and comparison between the two methods used. a) Test site 1; b) Test site 2. The dashed lines indicates the layer boundaries.

The interval Q values obtained, comparing the values derived from the SR method, show an excellent correspondence and a minimum error. Values of Q_P from SR method are included from 0.3 to 32.6, and Q_S from 1.2 to 13.2, not considering negative and out of range values. In general, the calculated values with the rise-time method are higher, considering mean values, as we have observed in a precedent study for Q_P (*Cercato, Desideri, 2018*). Some authors attribute this discrepancy to mode conversions, scattering around the borehole (*Morozov, 2008*), and signal dispersion with depth.

For obvious technical issues, the values obtained with the rise-time method can only be relative to the specific depth, as it is not possible to obtain step interval values.

4.5 Experimental dispersion curves

In this section, we apply the techniques reviewed in this paper for the determination of dispersion curves, applied on experimental dataset obtained in the same site of DHT survey (**Section 4.1**).

4.5.1 **Instrumentation and survey layout**

The investigation depth depends on the maximum measured wavelength and the resolution decreases with depth. In particular, resolution at shallow depth depends on the high frequency content (small wavelengths) of the recorded data.

In this active surface wave test was adopted using a receiver array and an active source. The scheme used involves in a linear array of 24 vertical geophones 2-meters spaced with in-line sources, for a final array length of 48 meters. The spatial sampling frequency affects the maximum wavenumber, which corresponds to the minimum wavelength. The source offset is the distance between the source and the closest receiver. In this test we have adopted a scheme called **common receiver gather**. A single array is deployed and left in place while the shot position (source offset) is moved along a line at evenly spaced locations. Six source offset are used in this test (**Figure 4.27**).

The wave field was generated by a 6 kg sledge-hammer striking manually on an Aluminum plate (30 cm diameter) fixed on the ground; a set of 24 vertical geophones with a natural frequency of 4.5 Hz and the same seismograph described in **Section 4.2.1.3**.

Figure 4.27: Views of the surface waves testing site and instrumentation. Both vertical and horizontal geophone can be observed in figure, but only vertical geophones dataset has been used

The acquisition parameters and survey design are described in table below:

Parameter	Value
Number of channels	1-vertical
Number of receivers	24
Receivers distance	2 mt
Sampling rate	8000 Hz
Number of samples	16384
Recording length	512 ms
Sampling interval	0.03125 ms

Table 4-4: Parameters acquisition and design parameters used in the site of Rieti.

4.5.2 **Data processing**

6 single shot gathers have been acquired separately to allow for statistical assessment of signal-to-noise ratio or for uncertainty evaluation. The raw-stacked shotgathers are plotted in **Figure 4.28**.

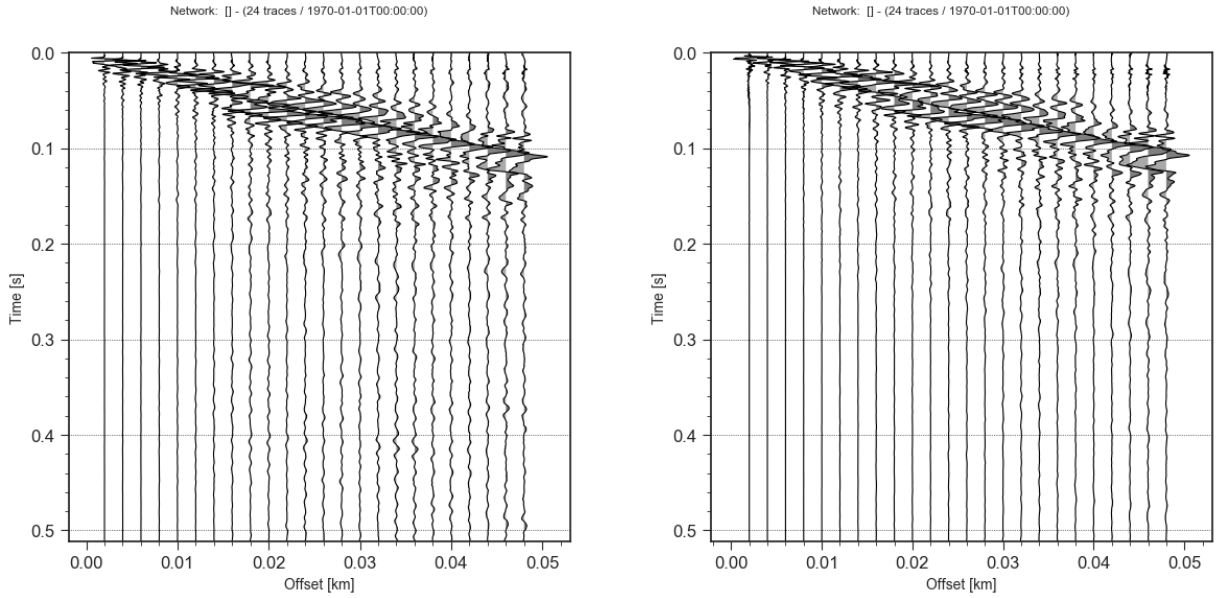

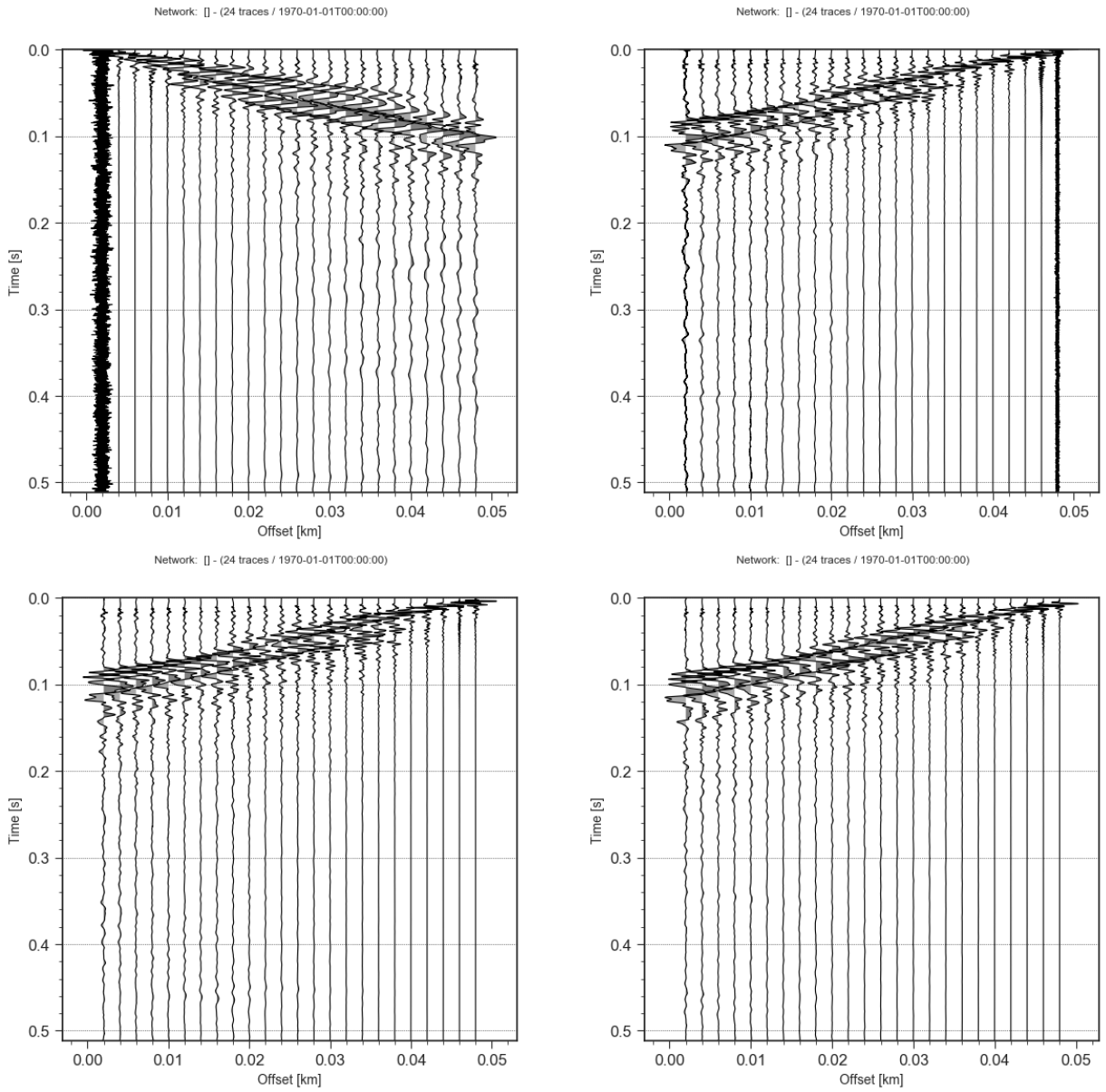

Figure 4.28: Reference dataset: stacked multichannel seismograms (shot gathers) displayed as wiggle traces.

As for the borehole surveys, even for surface waves testing the aim of the processing procedure is to increase the S/N ratio and extract the coherent signal from the wave field. The procedure used in this work for the processing consists in three principal steps, that have been implemented in a PYTHON code:

- **Filtering**: a 10-120 Hz butterworth band-pass frequency filter has been applied to the seismic dataset in order to remove high frequency and very low frequency noise. The lower and upper frequency bounds have been evaluated by the same procedure explained in **Section 4.3.4**;
- **Muting:** as explained in **Section 4.3.3** a muting procedure has been applied in order to remove body wave intrusions and other low amplitude noises present in the raw wavefield. It is performed by selecting two limiting scanning phase-velocities on the wave field, meant for top-muting and bottom-muting, based

on which the events above and below the corresponding limits will be removed; the limits adopted corresponds to 90 and 170 m/s phase velocities;

- **Windowing:** A Blackmann-Harris window function has been applied on each muted trace.

In the figure below are represented the 6 records, corresponding to 6 different source offsets, positioned symmetrically with respect to the center of the line, after processing procedures.

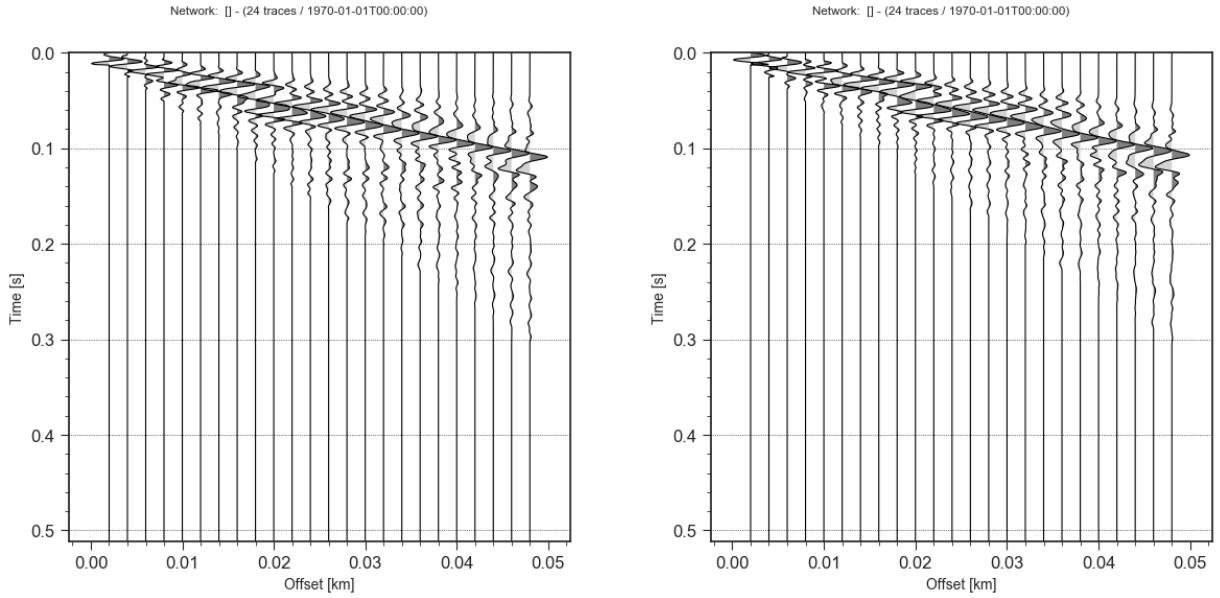

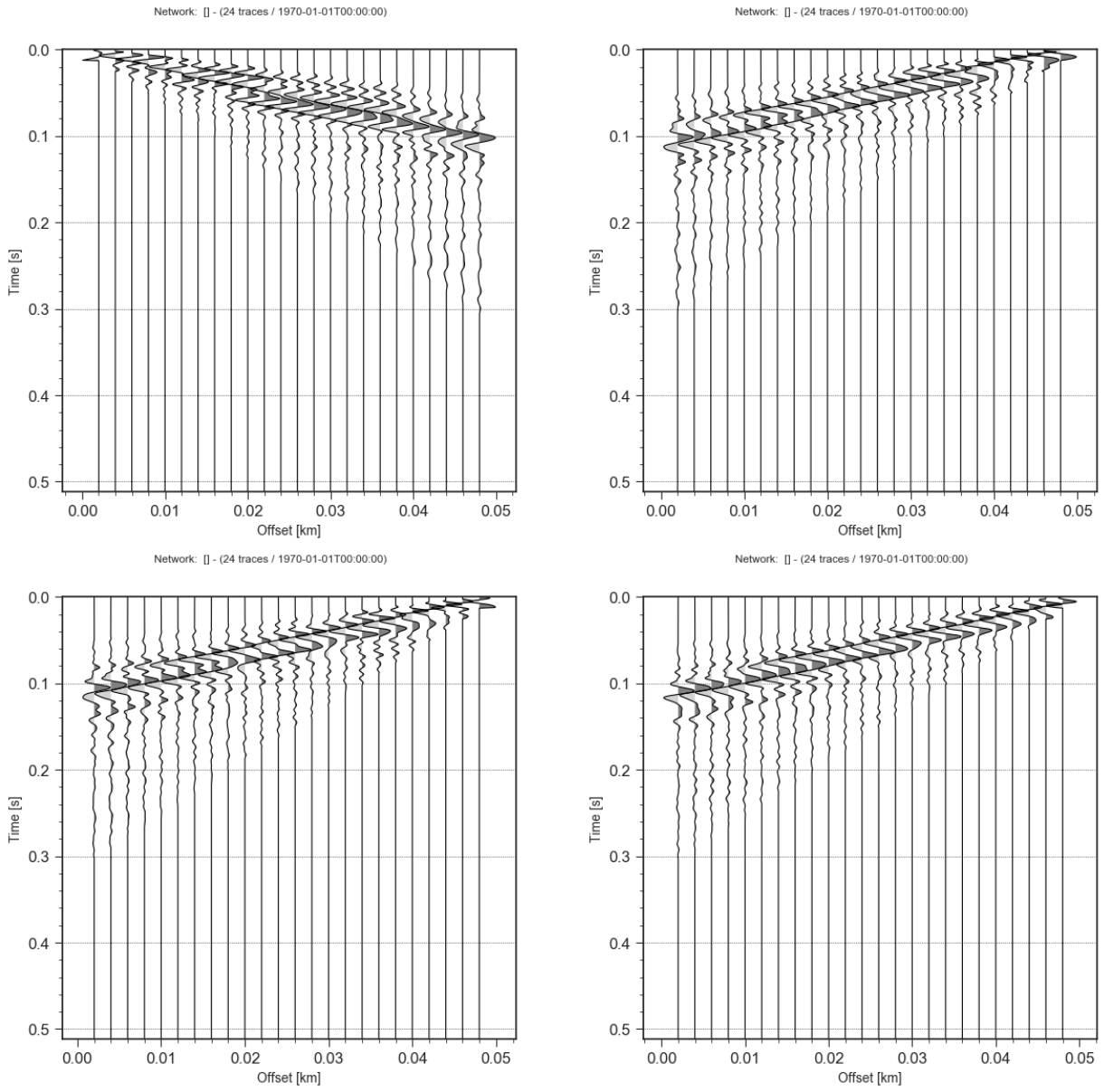

Figure 4.29: Processed datasets: stacked and processed multichannel seismograms (shot gathers) displayed as wiggle traces.

4.5.3 **Extract dispersion and attenuation curves**

We have now adopted **Phase shift method** (see **Section 3.2.3**) in order to extract fundamental mode dispersion curves from the full wavefield on a shot gather, using a simple three-step transformation method.

The first step is to apply the Fast Fourier transform to extract the normalized amplitudes of the transformed signals in according with equation 4-12 and removing frequencies above/below specified max/min frequency.

In **Figure 4.30,** we can observe the normalized spectrum of traces 5,6,7,8 that have been transformed.

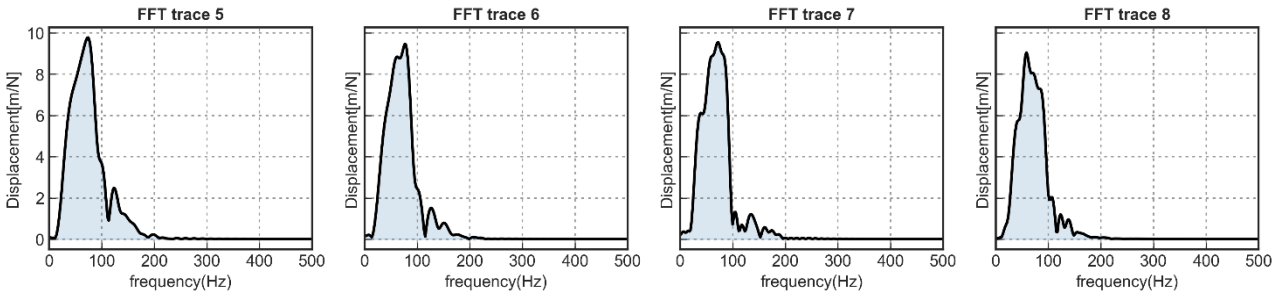

Figure 4.30: Normalized spectrum of trace 5,6,7,8.

We can now start the transformation looping through frequencies and trial velocities in according with equation 4 in Park et al. (*1998*).

Dispersion imaging is now obtained by plotting the summed amplitude in the frequency–phase velocity domain in two dimensions. This is possible by looping The dispersion analysis of the recorded data has carried out specifying a testing Rayleigh wave velocity range of 50-2000 m/s and a frequency range of 5-200 Hz. The peak values (high-amplitude bands) observed display the dispersion characteristics of the recorded surface waves, in which we can identify and pick the fundamental mode dispersion curve by using a specific function based on the spectral maxima observed at each frequencies. Fundamental mode dispersion curves have been extracted from a selected range of frequency (15-80 Hz), because very high frequency has affected by higher modes (**Figure 4.31**). In this range of frequency can be observed a very clear dispersion curve for each source offset used for the test.

4.5.3.1 Example of the Phase shift method in PYTHON code

Here an extract of the PYTHON code used for the test, in this case we have reported the 6-dispersion imaging and extracted dispersion curves coming from the 6-source offsets in the frequency range mentioned before (**Figure 4.31**).

```
40. for c in range(len(freq)):
41.         # Loop through trial velocities at each frequency
42.         for r in range(np.shape(v_vals)[0]):
43.             V[r,c] = np.abs(np.sum(U[c,:]/np.abs(U[c,:])*np.exp(1j*2*np.pi*freq[c]*(spacing/v
    _vals[r]))))
44.
45.         # Identify index associated with peak power at current frequency
46.         max_id = np.nanargmax(V[:,c])
47.         pnorm[:,c] = V[:,c] / V[max_id,c]
48.         v_peak[c] = v_vals[max_id]
```

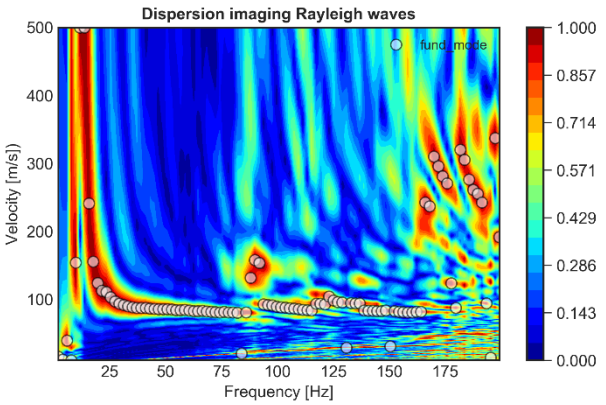
Dispersion imaging Rayleigh waves
fund_mode
Velocity [m/s]
Frequency [Hz]
1.000
0.857
0.714
0.571
0.429
0.286
0.143
0.000

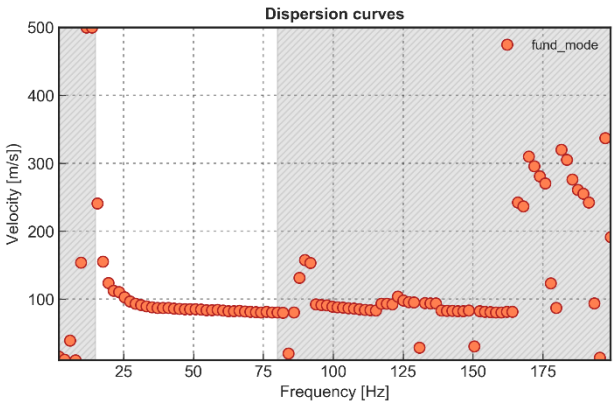
Dispersion curves
fund_mode
Velocity [m/s]
Frequency [Hz]

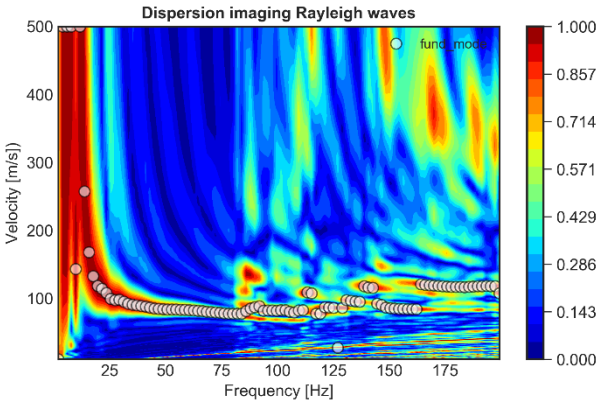
Dispersion imaging Rayleigh waves
fund_mode
Velocity [m/s]
Frequency [Hz]
1.000
0.857
0.714
0.571
0.429
0.286
0.143
0.000

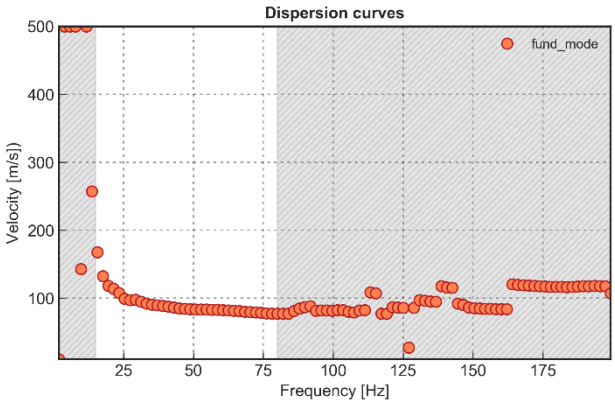
Dispersion curves
fund_mode
Velocity [m/s]
Frequency [Hz]

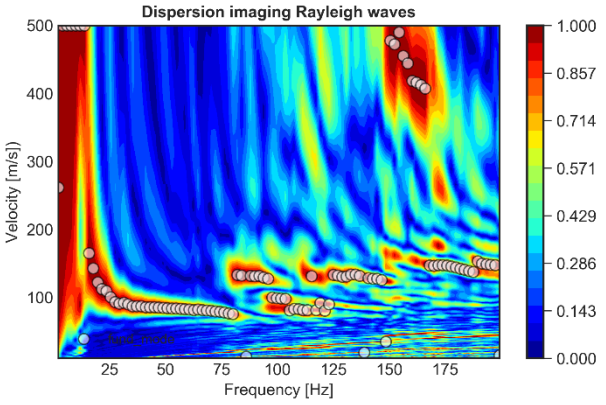
Dispersion imaging Rayleigh waves
Velocity [m/s]
Frequency [Hz]
1.000
0.857
0.714
0.571
0.429
0.286
0.143
0.000

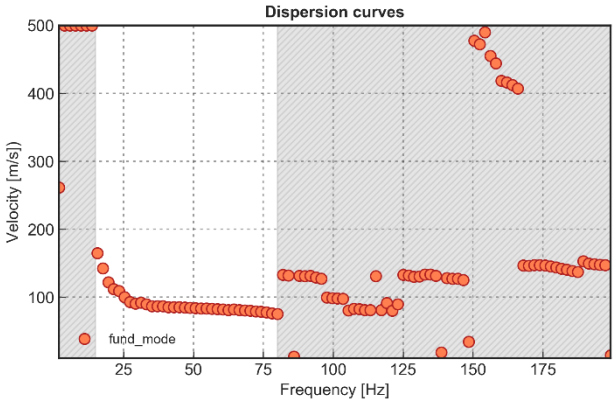
Dispersion curves
fund_mode
Velocity [m/s]
Frequency [Hz]

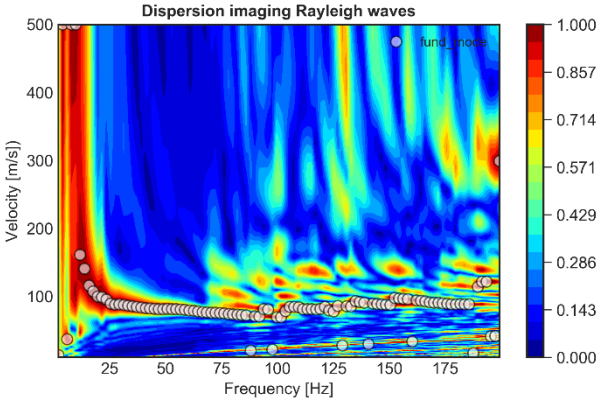
Dispersion imaging Rayleigh waves
fund_mode
Velocity [m/s]
Frequency [Hz]
1.000
0.857
0.714
0.571
0.429
0.286
0.143
0.000

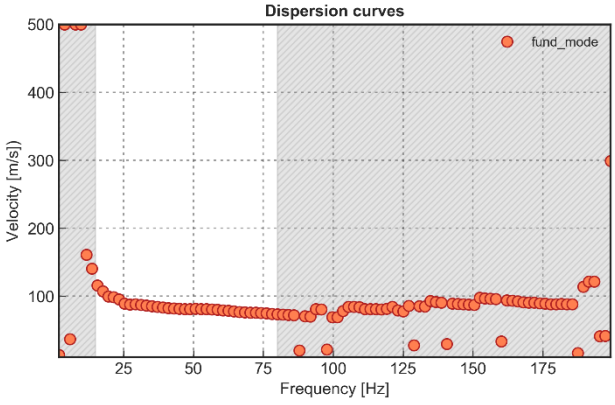
Dispersion curves
fund_mode
Velocity [m/s]
Frequency [Hz]

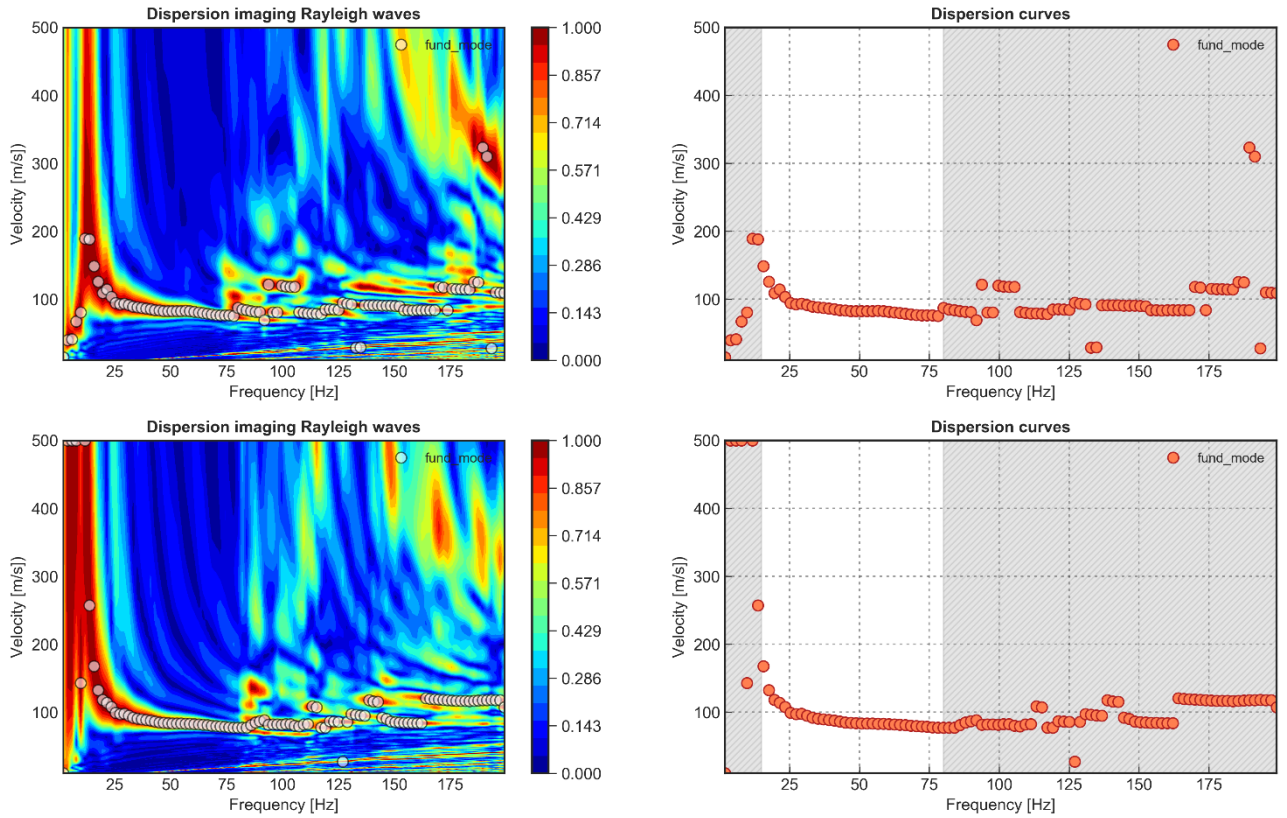

Figure 4.31: a) dispersion imaging of the 6 source offset dataset. b) extracted fundamental dispersion curve excluding out of frequency range values (grey-span).

A very useful plotting is the logarithmic plot dispersion imaging that can focus the visualization on the frequency of interest **(Figure 4.32**) and has been utilized to checking the lower bound limit in the frequency range, taken at 15 Hz. In this log-plot is well visible the role of the space sampling due to receivers used in the test.

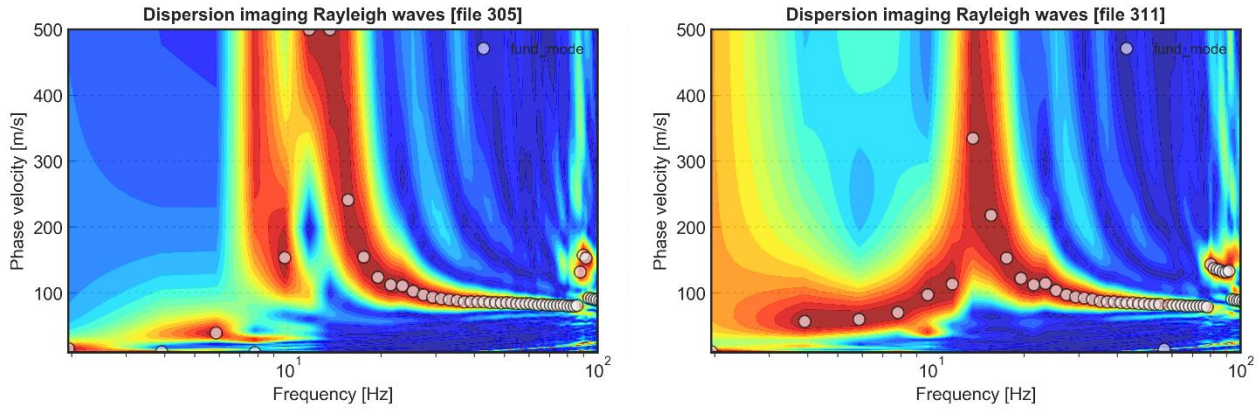

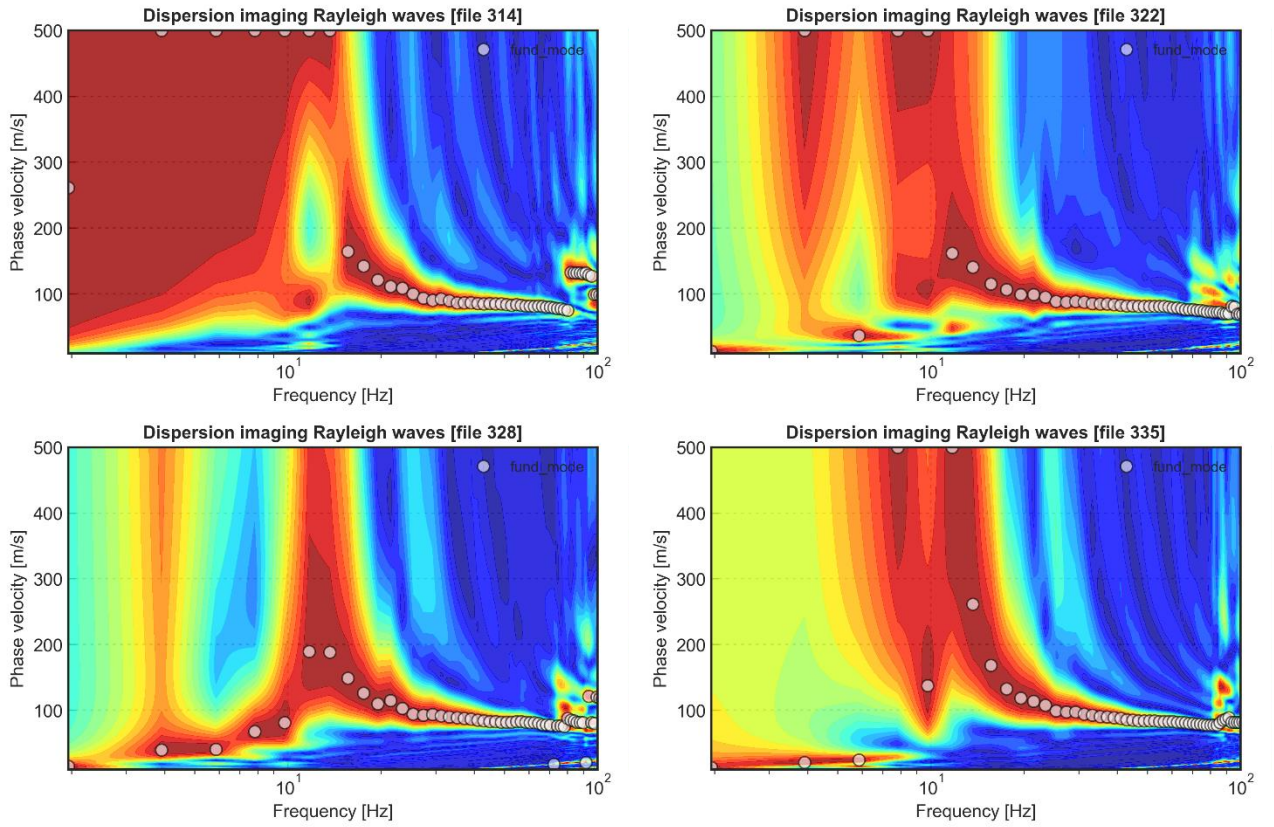

Figure 4.32: dispersion imaging in a logarithmic frequency scale.

The last step is to calculate the mean value coming from the different 6-source offsets fundamental dispersion curves as we can observe in **Figure 4.32**. For a practical question, it has been taken only the fundamental mode dispersion curve, rejecting higher modes for further applications. Taking a frequency range of 15-80 Hz, the fundamental mode is not affected by superposition with higher modes and this is easily extracted from the dispersion images. The curves show a good correlation in the 15-80 Hz band with a standard error 0.5-0.7, except for the lowest frequencies, where the error comes greater, as well-showed in **Figure 4.32** and **4.33b.**

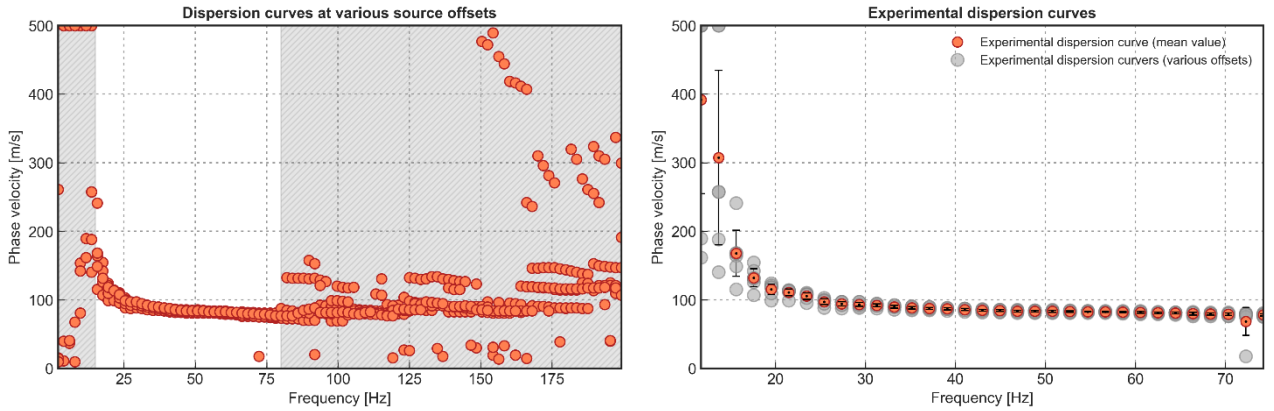

Figure 4.33: a) 6 source offset dispersion curves. b) dispersion curves mean value (in orange).

The experimental dispersion curve gives us a further information to optimize the model for theoretical consideration. As mentioned before, the investigation depth and maximum resolution at shallow depth depends on the maximum and minimum measured wavelength, corresponding to minimum and maximum frequency content of the considered dispersion curve, respectively.

By applying the well-known relation of the wavelength $\lambda = c/f$ we can calculate the minimum and maximum investigation depth, that in this case corresponding in a 3-24 meters depth range, considering a $\lambda/2$ maximum investigation depth.

4.6 Experimental attenuation curves

In this section, we apply the spectral analysis of the traces described in **Section 3.2.4** to obtain the fundamental mode attenuation curves. The dataset utilized and the processing applied on the raw dataset is the same explained previously.

4.6.1 Spectral analysis of surface waves

The code implements the Kudo and Shima (1970) method as explained in **Section 3.2.4**. This process involves in three simple steps. The first step is to evaluate the normalized spectrum $W(x, \omega)$ at a specific frequency of each traces. Fourier amplitudes of seismic signals obtained at various depths were corrected by means of the geometrical factor. With a loop for every frequency between 15 and 80 Hz it has been calculated the normalized logarithmic ratio of each receiver pairs. So as to obtain a set of 23 attenuation curves for each shot-gather ($n - 1$ pairs with $n = number\ of\ receivers$). This process is repeated for each source-offset, in order to calculate the six fundamental mode attenuation curves of Rayleigh waves.

The relation between the mean value of attenuation coefficients and frequency at various source offset are plotted in **Figure 4.34.**

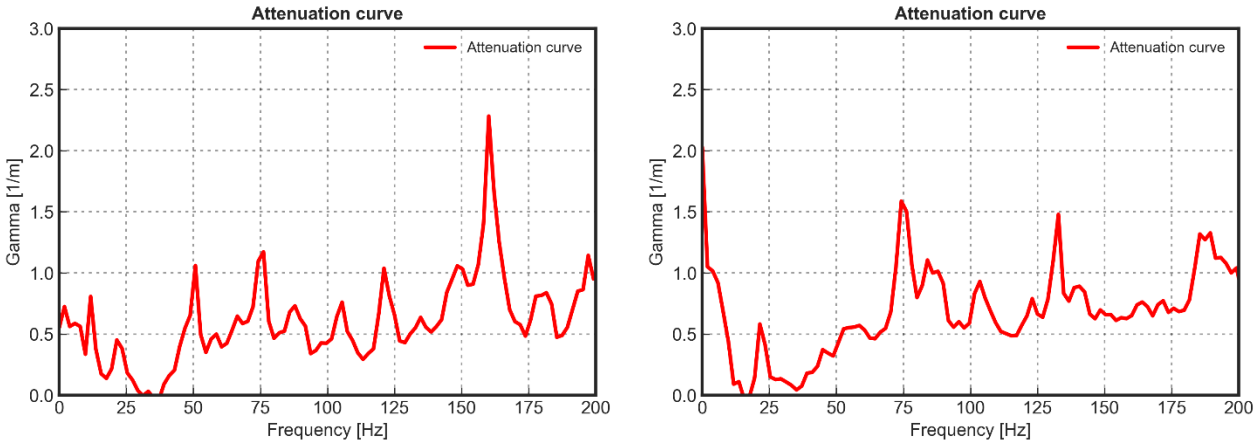

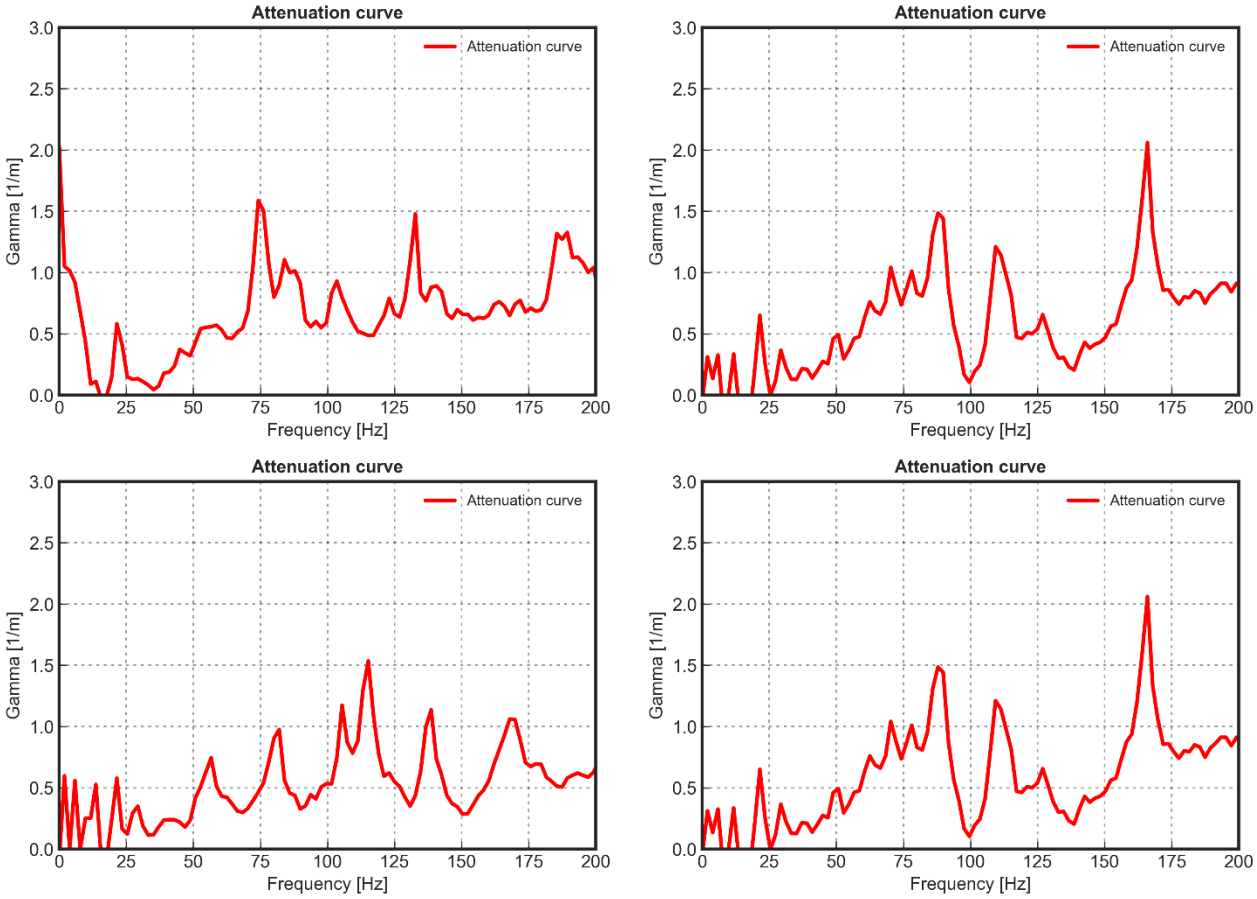

Figure 4.34: The attenuation curves of each shot gathers.

As for the experimental dispersion curves the mean value of this six curves are obtained and plotted in **Figure 4.35**. We can observe the resultant attenuation curve that exhibits a growing trend increasing frequency in a range of $\gamma(\omega)$ included from 0.01 to 0.9 for higher frequencies. The frequency range choosen for this test is the same described in **Section 4.5.2** for dispersion curves purpose.

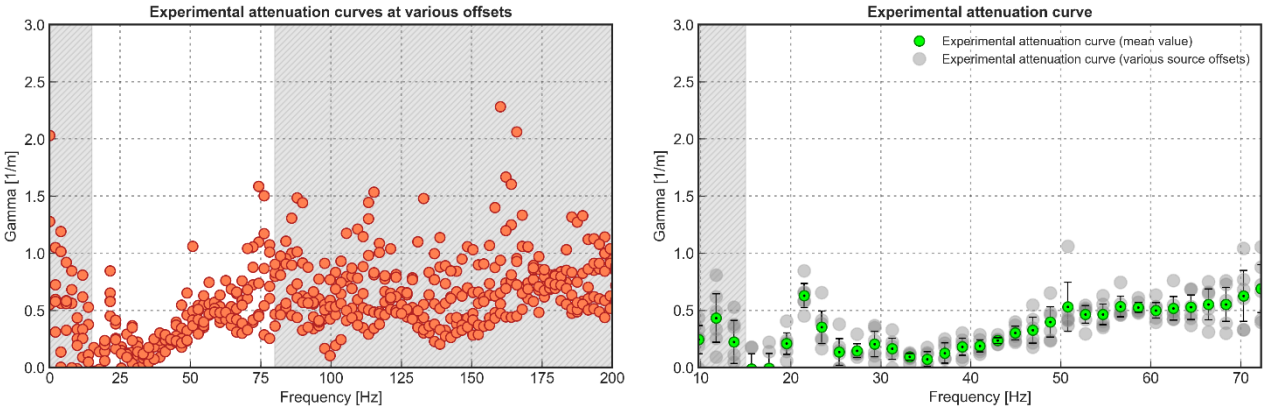

Figure 4.35: a) Total attenuation curves from various source offsets; b) mean value attenuation curve (in green) in the 15-80 frequency range

4.7 Comparison of theoretical and experimental dispersion and attenuation curves

This final section presents the comparison of numerically predicted (theoretical) and experimentally measured dispersion and attenuation curves for soils with damping. A test site is analyzed by means direct stiffness matrix modelling approach including an accurate damping profile. Experimental dispersion and attenuation curves for are retrieved by application of the methods, explained in **Sections 4.6** and **4.6**, to the measured dataset.

An eigenvalue problem in frequency and propagation constant is obtained, the solution of which yields dispersion and attenuation curves. These dispersion curves give information about the wave propagation in the considered model structure. In the classic approach, damping is discarded and free wave propagation is considered. In order to more accurately account for the damping effects and better predict the performance of soils, in this work it has included damping in the modelling technique. Numerical (theoretical or predicted) and experimental dispersion and attenuation curves are compared using the fundamental mode of propagation for the test site of Rieti showed **Figure 4.36**.

Both theoretical dispersion and attenuation curves are optimized with a model obtained from parameters coming from borehole seismic surveys (**Section 4.4**). The improvement in the direct stiffness method includes a detailed attenuation profile in the numerical computation, that enter in the model by introduces complex seismic velocity in the equations. The comparison it has made using only the fundamental mode of Rayleigh waves.

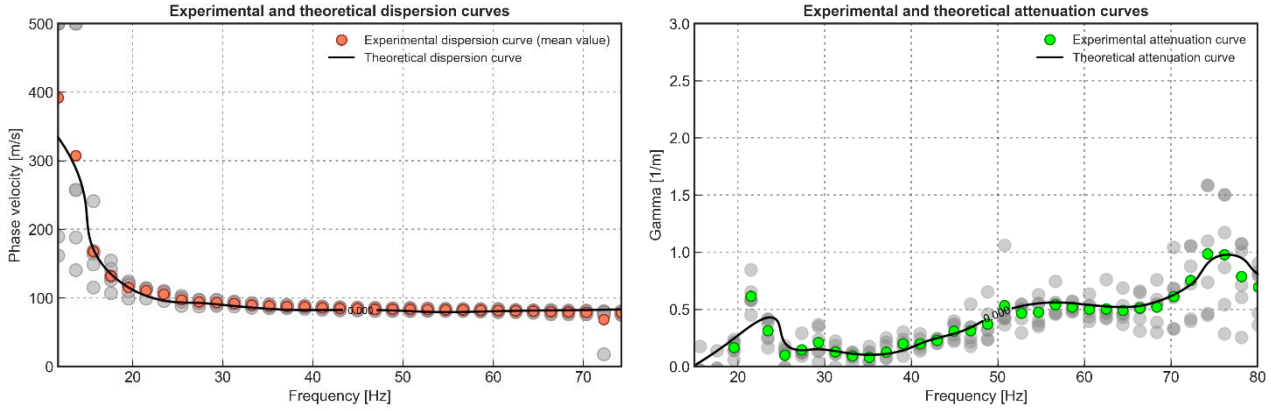

Figure 4.36: a) comparison between experimental and theoretical fundamental mode dispersion curve. b) comparison between experimental and theoretical fundamental mode attenuation curve.

The comparison is provided taking only the fundamental mode of both dispersion and attenuation curves in a frequency range of 15-80 Hz. In this work we decided to cut high frequencies because for large frequency values the numerical errors were too large and the mode superposition was too strong. A good agreement is found between the shapes of the dispersion and attenuation curves. In the low frequency region (15-20 Hz) and high frequency (70-80 Hz) for attenuation curves some more discrepancies are noticed, which can

be explained by the boundary conditions and numerical problems. With increasing frequency, together with the presence of damping, these boundary conditions and numerical problems become higher.

The numerically predicted and experimentally measured dispersion and attenuation curves are in good agreement for the fundamental mode of propagation. The insertion of an accurate Q_P and Q_S profiles (i.e. damping profiles) can describe in this case the more complex dissipative behavior of the medium.

We suggest that the contribution of Rayleigh wave attenuation coefficients from Q_P and Q_S cannot be ignored since the Q_S/Q_P ratio reaches is about 0.6 (**Section 4.4**), which is not uncommon in the near-surface settings.

Both in professional practice and in scientific research the damping factor is approximated to arbitrary values, or simply ignored. The purpose of this study is to demonstrate that an accurate damping profile coming from borehole studies can be an improvement to obtain reliable curves used in an inversion geophysical process.

Chapter 5.
Conclusions

5.1 **Conclusions**

Borehole seismic surveys have been adopted to estimate the soil quality factors described in this thesis. The in situ experiment have provided reliable measurements for both Q_P and Q_S by using a three-channel string of 8-receivers. Two different methodologies are developed for the determination of the quality factor (i.e. material damping ratio), the methods used in this are the spectral ratio and rise-time method. Rise-time method have never been used for near-surface attenuation measurements (<100m). These two methods are applied to the downhole-VSP test in the site of Rieti. Both of the results are compared and explained in **Chapter 4**.

It is demonstrated in this thesis that the existing methods to determine the quality factor can provide reliable attenuation estimates even in near-surface scale, adopting the processing procedure on the seismic dataset. The profiles how a very low Q values included in the range 2-10 for Q_S and 5-25 for Q_P, and the relative damping profiles. We find that S waves attenuate more strongly than P waves ($Q_S/Q_P \cong 0.6$).

Moreover, a surface wave test has been produced in order to explore the experimental attenuation and dispersion curves with the theoretical ones, calculated adopting an accurate model with parameters coming from downhole-VSP surveys. Forward model has been implemented using the direct stiffness matrix method described in Kausel (*1981*). Finally, an investigation on the thin layer method has been produced (*Kausel, 1994*), with an eye to possible further developments.

Providing reliable measurements of seismic attenuation in near-surface scale can be affected by many errors and incorrect estimates. The spectral ratio method is more sensitive to the quality of the spectral resolution, and even on the choice of the frequency band used for the process. Rise-time can provide good absorption results only in presence of good quality seismic signals. Only an accurate processing procedure on the quality of the seismic data can be the solution of this problem. The procedure adopted for the in-situ experiment and processing are explained in detail in **Chapter 4**. A faster and standardized procedure can be the key for a practical use of this parameter, very underestimate in the past.

Both the proposed techniques applied on the downhole-VSP method produced reliable results, a further approach of this technique is to investigate the results using a vibrating source (vibroseis) in order to check the attenuation changes with frequency.

In this study, it has been taken only the fundamental mode of Rayleigh waves. Many improvements will be possible in first case the computation of higher modes, that is a problem for the attenuation curves since the curves will overlap one another.

Last, but not least, providing attenuation measurements from borehole surveys, can be considered as a key element and a fundamental parameter in the understanding, in a sensitive territory like the Italian one, of the real mechanism of the superficial terrains subject of a seismic event.

Bibliography

Abercrombie, Rachel E. "Near-surface attenuation and site effects from comparison of surface and deep borehole recordings." *Bulletin of the Seismological Society of America* 87.3 (1997): 731-744.

Abercrombie, Rachel E. "A summary of attenuation measurements from borehole recordings of earthquakes: the 10 Hz transition problem." *Q of the Earth: Global, Regional, and Laboratory Studies*. Birkhäuser, Basel, 1998. 475-487.

Abercrombie, Rachel E. "Crustal attenuation and site effects at Parkfield, California." *Journal of Geophysical Research: Solid Earth* 105.B3 (2000): 6277-6286.

Angel, Y. C., and Jan Drewes Achenbach. "Reflection and transmission of obliquely incident Rayleigh waves by a surface-breaking crack." *The Journal of the Acoustical Society of America* 75.2 (1984): 313-319.

Aki, Keiiti, and Bernard Chouet. "Origin of coda waves: source, attenuation, and scattering effects." *Journal of geophysical research* 80.23 (1975): 3322-3342.

Aki, Keiiti. "Space and time spectra of stationary stochastic waves, with special reference to microtremors." *Bull. Earthq. Res. Inst.* 35 (1957): 415-456.

Badri, Mohammed, and Harold M. Mooney. "Q measurements from compressional seismic waves in unconsolidated sediments." *Geophysics* 52.6 (1987): 772-784.

Balch, Alfred H., et al. "The use of vertical seismic profiles in seismic investigations of the earth." *Geophysics* 47.6 (1982): 906-918.

Barton, Nick. (2007). *Rock Quality, Seismic Velocity, Attenuation and Anisotropy*.

Bath, M. "Spectral analysis in geophysics: Elsevier Sci." *Pubi. Co., Amsterdam* (1974).

Biot, Maurice A. "Theory of propagation of elastic waves in a fluid-saturated porous solid. II. Higher frequency range." *The Journal of the acoustical Society of america* 28.2 (1956): 179-191.

Biot, Maurice A. "Theory of propagation of elastic waves in a fluid-saturated porous solid. I. Lower frequency range." *The Journal of the acoustical Society of america* 28.2 (1956): 179-191.

Blair, Dane P. "A direct comparison between vibrational resonance and pulse transmission data for assessment of seismic attenuation in rock." *Geophysics* 55.1 (1990): 51-60.

Blair, D. P., and A. T. Spathis. "Attenuation of explosion-generated pulse in rock masses." *Journal of Geophysical Research: Solid Earth* 87.B5 (1982): 3885-3892.

Bracewell, Ronald Newbold, and Ronald N. Bracewell. *The Fourier transform and its applications*. Vol. 31999. New York: McGraw-Hill, 1986.

Carcione, Jose M., Dan Kosloff, and Ronnie Kosloff. "Viscoacoustic wave propagation simulation in the earth." *Geophysics* 53.6 (1988): 769-777.

Changjun Zhang and Tadeusz J. Ulrych, (2002), "Estimation of quality factors from CMP records," *Geophysics* 67: 1542-1547.

Chávez-García, Francisco J., and Francisco Luzón. "On the correlation of seismic microtremors." *Journal of Geophysical Research: Solid Earth* 110.B11 (2005).

Cheng, Peng, and Gary F. Margrave. "Estimation of Q: a comparison of different computational methods." *CSPG/CSEG/CWLS GeoConvention* 12 (2013): 2-5.

Dal Moro, G., and Maria Zadro. "Remarkable tilt–strain anomalies preceding two seismic events in Friuli (NE Italy): their interpretation as precursors." *Earth and planetary science letters* 170.1-2 (1999): 119-129.

Der, Zoltan A., and Alison C. Lees. "Methodologies for estimating t*(f) from short-period body waves and regional variations of t*(f) in the United States." *Geophysical Journal International* 82.1 (1985): 125-140.

Desideri, Francesco Saverio, and Cercato Michele. "estimation of near-surface seismic attenuation through vsp surveying." *37° convegno nazionale GNGTS*, (2018)

Engelhard, L. "Determination of seismic-wave attenuation by complex trace analysis." *Geophysical Journal International* 125.2 (1996): 608-622.

Ewing, W. Maurice, et al. "Elastic waves in layered media." *Physics Today* 10 (1957): 27.

Foti, Sebastiano, et al. *Surface wave methods for near-surface site characterization*. CRC press, 2014.

Foti, Sebastiano, et al. "Guidelines for the good practice of surface wave analysis: A product of the InterPACIFIC project." *Bulletin of Earthquake Engineering* 16.6 (2018): 2367-2420.

Gilbert, Freeman, and George E. Backus. "Propagator matrices in elastic wave and vibration problems." *Geophysics* 31.2 (1966): 326-332.

Gladwin, Michael T., and F. D. Stacey. "Anelastic degradation of acoustic pulses in rock." *Physics of the Earth and Planetary Interiors* 8.4 (1974): 332-336.

Hammarling, Sven, Christopher J. Munro, and Francoise Tisseur. "An algorithm for the complete solution of quadratic eigenvalue problems." *ACM Transactions on Mathematical Software (TOMS)* 39.3 (2013): 18.

Haskell, Norman A. "The dispersion of surface waves on multilayered media." *Bulletin of the seismological Society of America* 43.1 (1953): 17-34.

Hatherly, P. J. "Attenuation measurements on shallow seismic refraction data." *Geophysics* 51.2 (1986): 250-254.

Hough, S. E., et al. "Attenuation near Anza, California." *Bulletin of the Seismological Society of America* 78.2 (1988): 672-691.

Jannsen, D., J. Voss, and F. Theilen. "Comparison of methods to determine Q in shallow sediments from vertical reflection seismograms." *Geophysical Prospecting* 33.4 (1985): 479-497.

Johnston, David Hervey, M. N. Toksöz, and A. Timur. "Attenuation of seismic waves in dry and saturated rocks: II. Mechanisms." *Geophysics* 44.4 (1979): 691-711.

Johnston, David H., M. Nafi Toksoz, and Franklyn K. Levin, eds. *Seismic wave attenuation*. Society of Exploration Geophysicists, 1981.

Jongmans, D. "In-situ attenuation measurements in soils." *Engineering Geology* 29.2 (1990): 99-118.

Kausel, Eduardo, and José Manuel Roësset. "Stiffness matrices for layered soils." *Bulletin of the seismological Society of America* 71.6 (1981): 1743-1761.

Kausel, Eduardo. "Thin-layer method: Formulation in the time domain." *International journal for numerical methods in engineering* 37.6 (1994): 927-941.

Kausel, Eduardo. *Fundamental solutions in elastodynamics: a compendium*. Cambridge University Press, 2006.

Kjartansson, Einar. "Constant Q-wave propagation and attenuation." *Journal of Geophysical Research: Solid Earth* 84.B9 (1979): 4737-4748.

Klimentos, Theodoros. "Attenuation of P-and S-waves as a method of distinguishing gas and condensate from oil and water." *Geophysics* 60.2 (1995): 447-458.

Knopoff, L. "Q," Reviews of Geophysics, Vol. 2, No. 4, 1964, pp. 625-660. doi:10.1029/RG002i004p00625

Kramer, Steven L. Geotechnical Earthquake Engineering. Upper Saddle River, N.J: Prentice Hall, 1996. Print.

Kudo, Kazuyoshi, and Etsuzo Shima. "Attenuation of shear waves in soil." *Bull. Earthq. Res. Inst* 48 (1970): 145-158.

Kurtuluş, Cengiz, and Fadime Sertçelik. "Attenuation measurements on shallow seismic refraction data in the Kocaeli region, Turkey." *Journal of Geophysics and Engineering* 7.3 (2010): 257-266.

Lai, Carlo G., et al. "Simultaneous measurement and inversion of surface wave dispersion and attenuation curves." *Soil Dynamics and Earthquake Engineering* 22.9-12 (2002): 923-930.

Lay, Thorne, and Terry C. Wallace. *Modern global seismology*. Vol. 58. Elsevier, 1995.

Lerche, I., and William Menke. "An inversion method for separating apparent and intrinsic attenuation in layered media." *Geophysical Journal International* 87.2 (1986): 333-347.

Li, Huijian, et al. "A method for low-frequency noise suppression based on mathematical morphology in microseismic monitoring." *Geophysics* 81.3 (2016): V159-V167.

Mateeva, Albena. "Quantifying the uncertainties in absorption estimates from VSP spectral ratios." *Center for Wave Phenomena—Report* 457 (2003): 1-14.

Mavko, Gerald, and Amos Nur. "Melt squirt in the asthenosphere." *Journal of Geophysical Research* 80.11 (1975): 1444-1448.

Mavko, Gerald, Einar Kjartansson, and Kenneth Winkler. "Seismic wave attenuation in rocks." *Reviews of Geophysics* 17.6 (1979): 1155-1164.

McMechan, George A., and Mathew J. Yedlin. "Analysis of dispersive waves by wave field transformation." *Geophysics* 46.6 (1981): 869-874.

Misbah, Amr S., and Claudio L. Strobbia. "Joint estimation of modal attenuation and velocity from multichannel surface wave data." *Geophysics* 79.3 (2014): EN25-EN38.

Morozov, Igor B. "Geometrical attenuation, frequency dependence of Q, and the absorption band problem." *Geophysical Journal International* 175.1 (2008): 239-252.

Morozov, Igor B. "Mechanisms of geometrical seismic attenuation." *Annals of Geophysics* 54.3 (2011).

Morozov, Igor, and Amin Baharvand Ahmadi. "Taxonomy of Q." *Geophysics* 80.1 (2014): T41-T49.

Nazarian, S. "In situ shear wave velocities from spectral analysis of surface wave." *Proceedings of 8th Conference on Earthquake Engineering, San Francisco, 1984*. 1984.

O'Connel, R.J. & Budiansky, B. 1977. Viscoelastic properties of fluid-saturated cracked solids. *Journal of Geophysical Research*, 82: 5719–5736.

Olafsdottir, Elin Asta, Sigurdur Erlingsson, and Bjarni Bessason. "Tool for analysis of multichannel analysis of surface waves (MASW) field data and evaluation of shear wave velocity profiles of soils." *Canadian Geotechnical Journal* 55.2 (2017): 217-233.

Park, Choon Byong, Richard D. Miller, and Jianghai Xia. "Imaging dispersion curves of surface waves on multi-channel record." *SEG Technical Program Expanded Abstracts 1998*. Society of Exploration Geophysicists, 1998. 1377-1380.

Park, Choon B. "Imaging dispersion of MASW data—Full vs. selective offset scheme." *Journal of Environmental & Engineering Geophysics* 16.1 (2011): 13-23.

Paul, A., et al. "Amplitudes of regional seismic phases in relation to crustal structure of the Sierra Nevada, California." *Journal of Geophysical Research: Solid Earth* 101.B11 (1996): 25243-25254.

Quan, Youli, and Jerry M. Harris. "Seismic attenuation tomography using the frequency shift method." *Geophysics* 62.3 (1997): 895-905.

Rai, S. S., Amit Padhi, and P. Rajgopala Sarma. "High crustal seismic attenuation in Ladakh–Karakoram." *Bulletin of the Seismological Society of America* 99.1 (2009): 407-415.

Raikes, S. A., and R. E. White. "Measurements of earth attenuation from downhole and surface seismic recordings." *Geophysical Prospecting* 32.5 (1984): 892-919.

Richards, Paul G., and Keiiti Aki. Quantitative seismology: theory and methods. Freeman, 1980.

Sarma, L. P., and N. Ravikumar. "Q-factor by spectral ratio technique for strata evaluations." *Engineering geology* 57.1-2 (2000): 123-132.

Schevenels, M., and G. Degrande. "ElastoDynamics Toolbox (EDT) for Matlab, Version 2.0." *User's manual BWM-2007-07, Department of Civil Engineering, KU Leuven* (2007).

Spencer Jr, James W. "Stress relaxations at low frequencies in fluid-saturated rocks: Attenuation and modulus dispersion." *Journal of Geophysical Research: Solid Earth* 86.B3 (1981): 1803-1812.

Stacey, F. D., et al. "Anelastic damping of acoustic and seismic pulses." *Geophysical surveys* 2.2 (1975): 133-151.

Strobbia, Claudio, and Sebastiano Foti. "Multi-offset phase analysis of surface wave data (MOPA)." *Journal of Applied Geophysics* 59.4 (2006): 300-313.

Teng, Ta-Liang. "Attenuation of body waves and the Q structure of the mantle." *Journal of Geophysical Research* 73.6 (1968): 2195-2208.

Thomson, William T. "Transmission of elastic waves through a stratified solid medium." *Journal of applied Physics* 21.2 (1950): 89-93.

Tokimatsu, Kohji. "Geotechnical site characterization using surface waves." *Earthquake geotechnical engineering* (1997).

Tokimatsu, Kohji, Shuji Tamura, and Hisaya Kojima. "Effects of multiple modes on Rayleigh wave dispersion characteristics." *Journal of geotechnical engineering* 118.10 (1992): 1529-1543.

Toksöz, M. N., David H. Johnston, and Aytekin Timur. "Attenuation of seismic waves in dry and saturated rocks: I. Laboratory measurements." *Geophysics* 44.4 (1979): 681-690.

Tonn, Rainer. "The determination of the seismic quality factor Q from VSP data: A comparison of different computational methods." *Geophysical Prospecting* 39.1 (1991): 1-27.

Tschoegl, N. W. "The Phenomenological Theory of Linear Viscoelastic Behaviour An Introduction Springer-Verlag." *Berlin, Beidelberg, Germany* (1989).

Udias, Agustin, and Elisa Buforn. Principles of seismology. *Cambridge University Press*, 2017.

I. A. Viktorov. Rayleigh and Lamb waves. *Plenum Press*, New York, 1967.

Virieux, Jean, and Stéphane Operto. "An overview of full-waveform inversion in exploration geophysics." *Geophysics* 74.6 (2009): WCC1-WCC26.

Walsh, J. B. "Seismic wave attenuation in rock due to friction." *Journal of Geophysical Research* 71.10 (1966): 2591-2599.

Wang, Yanghua. "Inverse Q-filter for seismic resolution enhancement." *Geophysics* 71.3 (2006): V51-V60.

White, R. E. "The accuracy of estimating Q from seismic data." *Geophysics* 57.11 (1992): 1508-1511.

Wu, Huatao, and Jonathan M. Lees. "Attenuation structure of Coso geothermal area, California, from wave pulse widths." *Bulletin of the Seismological Society of America* 86.5 (1996): 1574-1590.

Xia, Jianghai, et al. "Determining Q of near-surface materials from Rayleigh waves." *Journal of applied geophysics* 51.2-4 (2002): 121-129.

Yoshimoto, Kazuo, Haruo Sato, and Masakazu Ohtake. "Frequency-dependent attenuation of P and S waves in the Kanto area, Japan, based on the coda-normalization method." *Geophysical Journal International* 114.1 (1993): 165-174.

Zucca, J. J., L. J. Hutchings, and P. W. Kasameyer. "Seismic velocity and attenuation structure of the Geysers geothermal field, California." *Geothermics* 23.2 (1994): 111-126.

Acknowledgements

Desidero ringraziare anzitutto il Prof. Michele Cercato per la bellissima esperienza formativa e di crescita professionale, ed anche per l'aiuto che sempre ha saputo darmi in questi tre anni di dottorato.

Ringrazio anche tutti i colleghi dell'area di geofisica, in particolare Giorgio e Francesco, presenti anche nelle numerose campagne effettuate insieme.

Ringrazio tutti i professionisti, professori e ricercatori che hanno collaborato anche indirettamente per la realizzazione di questo progetto.

Ringrazio i miei colleghi, Camilla, Marco, i due Andrea, Sara e Vincenzo che hanno condiviso con me questa esperienza.

Ringrazio tutta la mia famiglia, mia madre, mio padre, mia sorella, le mie zie, e i miei nipoti, sempre presenti nei miei traguardi, e soprattutto i miei nonni, Bruno e Franca. Un pensiero ai miei due zii, Angelo e Franco, che da poco ci hanno lasciato ma che avrei voluto ringraziare lo stesso.

Ringrazio i miei amici di sempre, e ancora una volta, Andrea, praticamente un fratello.

Ringrazio infine la mia ragazza, Clorinda, che sempre più sta diventando un punto di riferimento, che mi ha spronato e incoraggiato nei momenti più difficili di questo percorso.